Technische Universität München

Fakultät für Physik

Lehrstuhl für Topologie Korrelierter Systeme

Transverse Susceptibility of Complex Magnetic Textures

Dipl.-Phys. Univ. Felix Simon Alexander Rucker

Abstract

In this thesis, experimental studies of complex magnetic textures by means of transverse susceptibility measurements are presented. In the Ising-ferromagnet $LiHoF_4$, a distinct dependence of the nature of the quantum phase transition on geometric misalignment of the sample with respect to the magnetic field direction is reported. Additionally, signatures of field-induced domain-wall tunnelling as well as a strong hyperfine coupling are observed. In the helimagnet MnSi, the interplay of conduction electrons with the skyrmion lattice, a topologically non-trivial form of magnetic order, is studied. As the main result, it is found that the critical current density, above which skyrmion motion is induced, may be reduced by over one order of magnitude with a small oscillating magnetic field.

In dieser Arbeit werden fundamentale Eigenschaften komplexer magnetischer Texturen in zwei Modellsystemen mittels transversaler Suszeptibilitätsmessungen untersucht. In dem Ising Ferromagneten $LiHoF_4$ wird die Abhängigkeit des Quantenphasenübergangs von einer geometrischen Fehlausrichtung der Probe im Bezug auf das magnetische Feld untersucht. Zusätzlich können Signaturen von Tunneleffekten der Domänenwände sowie einer Hyperfeinkopplung beobachtet werden. In dem Helimagneten MnSi wird das Zusammenspiel von Leitungselektronen mit einer komplexen Form magnetischer Ordnung, dem Skyrmionengitter, untersucht. Als Hauptergebnis wird berichtet, dass die kritische Stromdichte, bei der das Skyrmionengitter zu driften beginnt, durch das Anlegen eines oszillierenden magnetischen Feldes um mehr als eine Größenordnung reduziert werden kann.

Contents

Contents

Stabilisation and Dynamics of Complex Magnetic Order

While the interest in quantum matter was mainly restricted to basic research over the past century, modern material science and the fast development of experimental techniques have stimulated the search for possible applications of quantum states. New phenomena such as unconventional superconductivity [1, 2], topological insulators [3, 4], or complex forms of magnetic order [5–7] have been intensively studied over the past decades and promise a variety of exciting applications. In the search for such novel states of matter, the vicinity of continuous phase transitions, where strong fluctuations prevail, has proven to be a suitable starting point [8]. Such transitions can be driven either by a change of temperature, also referred to as classical phase transitions, or by non-thermal control parameters such as pressure, chemical composition or external fields. In the second case, so-called quantum phase transitions (QPTs) may even occur at absolute zero temperature, where no thermal excitations are possible and quantum effects may govern the macroscopic behaviour of the system. Over the past decades, the precise description of such transitions as well as the quantum critical region (QC) associated with them has been established as a key challenge in modern condensed matter physics.

A generic theoretical description of QPTs and the corresponding quantum critical regime is extremely demanding, however, some examples of experimentally accessible QPTs are known, which can be captured by current theoretical models. One of the simplest examples is the transition from a ferromagnetic into a paramagnetic state in the dipolar-coupled Ising ferromagnet $LiHoF_4$ as a function of applied magnetic field, aligned perpendicular to the Ising axis [9, 10]. Such systems provide an ideal probe to confirm the basic theoretical framework, laying the foundation for a successful understanding of more complex systems and more exotic behaviour [8]. These well-understood examples, however, are scare while systems driven towards quantum criticality typically exhibit more complex behaviour, exceeding the current theoretical descriptions.

An intensively investigated example of such complex behaviour is the cubic helimagnet MnSi, where the magnetic transition temperature can be suppressed by the application of hydrostatic pressure. The vanishing of static magnetic order is accompanied by a breakdown of the conven-

tional theory of electrons in metals, the Fermi liquid theory [11, 12]. Recently, the topologically non-trivial nature of the resulting non-Fermi liquid regime was linked to a phase pocket at ambient pressure that hosts a trigonal lattice of spin whirls, the so-called skyrmion lattice [7, 13]. One of the most intriguing consequences of the non-trivial topology in both regimes concerns their interplay with conduction electrons [14]. Most notably, in the skyrmion lattice an extremely efficient gyromagnetic coupling in combination with weak collective pinning leads to a drift of the magnetic texture above ultra-low current densities [15, 16]. Such spin-transfer torque effects have been investigated in ferromagnetic materials for several decades, paving the way for new concepts of magnetic storage devices [17, 18]. Large critical current densities in ferromagnets, however, complicate research on nanoscale samples. In turn, the investigation of the underlying mechanisms of the ultra-low critical current densities, as observed in the skyrmion lattice in MnSi, may contribute to a successful realisation of such devices [19–22].

The focus of this work is twofold. In the first part, a set of fundamental questions concerning the nature of the field-tuned QPT in the model magnet $LiHoF_4$ are addressed using transverse susceptibility measurements. In the second part, the same technique is used to investigate spin-transfer torque effects in the skyrmion lattice in MnSi, focussing in particular on the influence of an applied oscillating magnetic field on the critical current density.

Outline of this thesis

The first chapter starts with a presentation of the cryogenic environment and the experimental methods. In particular, magnetic AC susceptibility measurements are introduced and three types of bespoke low-temperature susceptometers, which have been developed as part of this thesis, are described. Finally, important instrument specifications are summarised and recent developments of the measurement automation software are discussed.

The second chapter presents the investigation of the field-tuned QPT in $LiHoF_4$. The chapter starts with an introduction to theoretical aspects and experimental realisations of QPTs. Then, the state of research on the low temperature properties of $LiHoF_4$ is summarised. After a short remark on specific experimental characteristics, the experimental results are discussed in two parts. First, measurements reproducing the so-far established picture of $LiHoF_4$ are presented and possible influences of a geometric misalignment between sample and magnetic field are discussed. Second, a detailed analysis of the ferromagnetic ground state is performed, revealing a set of yet unreported properties, such as signatures of field-induce domain-wall tunnelling or a strong hyperfine-coupling. The chapter is concluded by a summary of our results.

In the third chapter, generic properties of the skyrmion lattice in MnSi are investigated. First, the current state of research on MnSi is summarised introducing important aspects of the phase

diagram of cubic helimagnets in general as well as the topological properties of this compound. In particular, details of the skyrmion lattice and its interaction with strong DC currents are discussed. After accounting for specific experimental uncertainties, the experimental results are presented in four steps. First, measurements of the transverse susceptibility as a function of temperature and magnetic field across the entire magnetic phase diagram are discussed. Second, the influence of a variation of excitation frequency and excitation amplitude of the susceptibility measurement on the magnetic phases of MnSi is investigated. Third, it is shown that the movement of the skyrmion lattice and the associated critical current threshold may be captured using transverse susceptibility measurements. Finally, an alternating magnetic field is used to reduce the critical current in the skyrmion lattice by more than one order of magnitude. All measurement results are summarised the end of this chapter.

AC Susceptometry at Millikelvin Temperatures

In this chapter, important aspects of the experimental environment as well as technical developments in the context of this work are summarised. The chapter starts with a definition of the magnetic susceptibility, followed by a presentation of three bespoke susceptometers, which have been developed and calibrated as part of this thesis. General aspects of the measurement technique and the experimental environment are presented briefly before recent developments of the measurement automation software are discussed. A more detailed introduction to measurement-specific aspects of the experimental environment will be given in the corresponding sections 2.2 and 3.2.

1.1. The Magnetic Susceptibility

Over the past century, a variety of complex forms of magnetism have been discovered, exceeding the simple picture of a ferromagnet. Such structures range from simple antiferromagnets to highly complex magnetic structures such as the skyrmion lattice. One simple way to discriminate between such different types of magnetism is the investigation of the magnetisation M, which is defined as the magnetic moment per unit cell [23, 24]. Considering only macroscopic samples, the magnetisation is represented by a smooth vector field $\boldsymbol{M}$ over the whole sample, which can vary as a function of external control parameters such as a magnetic field $\boldsymbol{H}$ or the temperature T. Small discontinuities arising at the edges of the sample, so called demagnetisation effects, shall be neglected in the following considerations and are briefly discussed in sections 2.3.5 and 3.3.2. One important aspect of magnetic materials, however, which may not be captured using magnetisation measurements is the response of the magnetisation to a small magnetic field disturbance $\boldsymbol{H} + \partial \boldsymbol{H}_{\mathrm{AC}}(\omega)$. This response is, in the most general case, given

by a tensor and is called the magnetic susceptibility, χ_{ij}. In detail, this quantity describes the change of the magnetisation component M_i in response to a small magnetic field disturbance $\partial H_{\mathrm{AC},j}(\omega)$ along a certain spacial direction j.

$$\chi_{ij}(\boldsymbol{H}, T, \omega) = \frac{\partial M_i(\boldsymbol{H}, T)}{\partial H_{\mathrm{AC},j}(\omega)}, \qquad i, j \in \{x, y, z\} \tag{1.1}$$

Here, T is the sample temperature, $\boldsymbol{H}$ a static magnetic field and ω the frequency. The indices i and j denote the three spacial directions x, y and z. Note that this definition of the susceptibility does not consider any momentum transfer between the magnetic structure and the probing magnetic field, i.e. $\boldsymbol{q} = 0$. Complementary methods, such as certain neutron scattering techniques, may access a similar property, the dynamical susceptibility $\chi(\boldsymbol{q}, \omega)$, which can be evaluated as a function of non-zero momentum transfer ($\boldsymbol{q} \neq 0$). The following considerations are restricted to susceptibility measurements at $\boldsymbol{q} = 0$.

1.1.1. Definitions

The term magnetic susceptibility χ is commonly used, however confusingly often in different contexts or in a very simplified form. In the following, we introduce the magnetic susceptibility as used throughout this thesis. To simplify the considerations, we will restrict the susceptibility tensor χ_{ij} to diagonal elements only, assuming $i = j$. Note that off-diagonal elements of the susceptibility tensor might be quantities of interest, however, we expect most samples to show the largest response along the excitation axis and therefore keep this restriction. In general, we can discriminate between two generic cases. First, the AC susceptibility χ, in which an oscillating field $H_{\mathrm{AC}}(\omega)$ is used to probe the response of the magnetisation in addition to an applied static field H, stabilizing the magnetic order. Second, letting ω approach zero, the static case, χ^{stat}, in which a small change of the static field H is used to cause a change of the magnetisation in the sample.

$$\chi_{ij}(H, T, \omega) \xrightarrow{i,j=x} \chi(H, T, \omega) \xrightarrow{\omega \to 0} \chi^{\mathrm{stat}}(H, T) \tag{1.2}$$

In many materials, the static susceptibility may be approximated by the ratio of the magnetisation to the static field H [23]:

$$\chi^{\mathrm{stat}}(H, T) = \frac{\partial M(H, T)}{\partial H} \approx \frac{M(H, T)}{H} \tag{1.3}$$

Even though both χ and χ^{stat} may yield similar results in simple magnetic materials, providing first insight into the basic magnetic properties, the quantities mismatch if the magnetic state of the sample is more complex. Especially in regimes, in which slow dynamical processes play an important role, such as phase transitions or dominant tiny energy scales, the AC susceptibility χ is a more powerful tool to study the magnetic behaviour.

In general, the static magnetic field $\boldsymbol{H}$ and the oscillating excitation field $\boldsymbol{H}_{\mathrm{AC}}$ are vector quantities which may independently point along arbitrary spacial directions. Without loss of generality, we define the static field to point along a specific direction k, representing most of the experimental configurations.

$$\boldsymbol{H} = |\boldsymbol{H}| \cdot \hat{e}_k = H_k \qquad k \in \{x, y, z\} \tag{1.4}$$

Here, $\hat{e}_k$ represents the unit vector along the direction k. Keeping the restriction $i = j$, we can define two special geometric cases of the dynamic susceptibility. First the **longitudinal susceptibility**,

$$\chi_\parallel = \chi_{ijk}(H_k, T, \omega) = \frac{\partial M_i(H_k, T)}{\partial H_{\mathrm{AC},j}(\omega)} \qquad i, j, k \in \{x, y, z\} \text{ and } i = j \parallel k, \tag{1.5}$$

in which the static field H_k points parallel to the oscillating excitation field $H_{\mathrm{AC},j}$, and second the **transverse susceptibility**,

$$\chi_\perp = \chi_{ijk}(H_k, T, \omega) = \frac{\partial M_i(H_k, T)}{\partial H_{\mathrm{AC},j}(\omega)} \qquad i, j, k \in \{x, y, z\} \text{ and } i = j \perp k, \tag{1.6}$$

in which the static field H_k is aligned perpendicular to the oscillating excitation field $H_{\mathrm{AC},j}$. Both quantities, as defined in equations (1.5) and (1.6) will be investigated throughout this study.

1.1.2. Measurement Technique

The mutual inductance method represents one of the most common ways to record the susceptibility as defined in equations 1.5 and 1.6 [25]. In this method, a pair of balanced pick-up coils is used to detect the change of the magnetisation in a sample in response to an oscillating magnetic field $H_{\mathrm{AC}} = H_0 \cos(\omega t)$ which is generated by a primary excitation coil. According to Faraday's law of induction, the voltage, induced in an empty pick-up coil is given as

$$U_{\mathrm{ind}}^{\mathrm{vac}}(t) = -N_s \frac{\mathrm{d}\Phi}{\mathrm{d}t} = -\frac{\mathrm{d}}{\mathrm{d}t} N_s \int_A \mu_0 \cdot H_{\mathrm{AC}} \cdot \mathrm{d}A = \mu_0 H_0 \omega A N_s \sin(\omega t) \tag{1.7}$$

where μ_0 is the magnetic permeability, Φ the magnetic flux, N_s the number of windings of the pick-up coil and A the cross-section. When inserting a sample into the pick-up coil, the induced voltage becomes

$$U_{\mathrm{ind}} = U_{\mathrm{ind}}^{\mathrm{vac}} + U_{\mathrm{ind}}^{\mathrm{sample}} = \mu_0 H_0 \omega A N_s \sin(\omega t)(1 + \chi f) \tag{1.8}$$

where f is the volume fraction of the sample inside the coil volume. As the filling factor $f < 1$, and typical susceptibilities $|\chi| \ll 1$, the induced voltage U_{ind} is dominated by the vacuum contribution. Therefore, a pair of balanced pick-up coils is used to eliminate the vacuum signal

during data acquisition. Small systematic deviations as well as parasitic signal contributions, however, do not permit a complete suppression of the vacuum signal. The combined differential voltage of both pick-up coils is recorded by a phase sensitive detector which is phase-locked to a current source providing the excitation current $I_e(\omega_e)$ at frequency ω_e of the primary coil.

The recorded vacuum signal U_{vac} exhibits a 90° phase shift compared to the excitation current, as may be seen from equation (1.7). The sample contribution of the signal, however, may lead to an additional phase shift as compared to the excitation current. Accordingly, the signal may be split up into two components. First, an in-phase component with a 90° phase shift to the reference signal, and second an out-of-phase component with 0° phase shift. In-phase and out-of-phase are hereby defined with respect to the induced vacuum signal, which has an intrinsic 90° phase-shift with respect to the reference signal. Both components may be recorded simultaneously by the lock-in amplifier. The contribution which is in phase with the vacuum signal may be regarded as a direct response of the sample and is associated with the real part, $\mathrm{Re}\chi$, of the susceptibility. The imaginary part, $\mathrm{Im}\chi$, of the susceptibility vanishes for $\omega \to 0$ and may only be determined at finite excitation frequency. This contribution accounts for a variety of physical effects such as domain wall motion or strong fluctuations.

$$\chi = \chi' + i\chi'' = \mathrm{Re}(\chi) + i \cdot \mathrm{Im}(\chi) \tag{1.9}$$

In this study, real and imaginary parts of the transverse and the longitudinal susceptibilities as defined in equations 1.5, 1.6 and 1.9, are investigated

1.2. Experimental Techniques

As part this thesis, three different AC susceptometers were developed. Each susceptometer was optimized to fulfil a set of requirements for a certain type of experiment. The measurements were carried out in different types of cryogenic systems allowing measurements down to 30 mK and up to 16 T. In the following, the most important aspects of design and construction of the susceptometers are summarised and the sample environment and the developed measurement automation software are introduced.

1.2.1. Low Temperature Susceptometer

Figure 1.1 shows two types of low temperature susceptometers. The first, (a), was designed for susceptibility measurements under transverse magnetic fields, the second, (b), was designed for longitudinal measurements. The major challenge in the construction of a low temperature susceptometer is to ensure good thermal coupling of all parts, while maintaining a reasonably low background signal. To reach temperatures as low as 30 mK, the measurements have to be conducted in high vacuum, hence, exchange gas cannot be used for thermalisation.
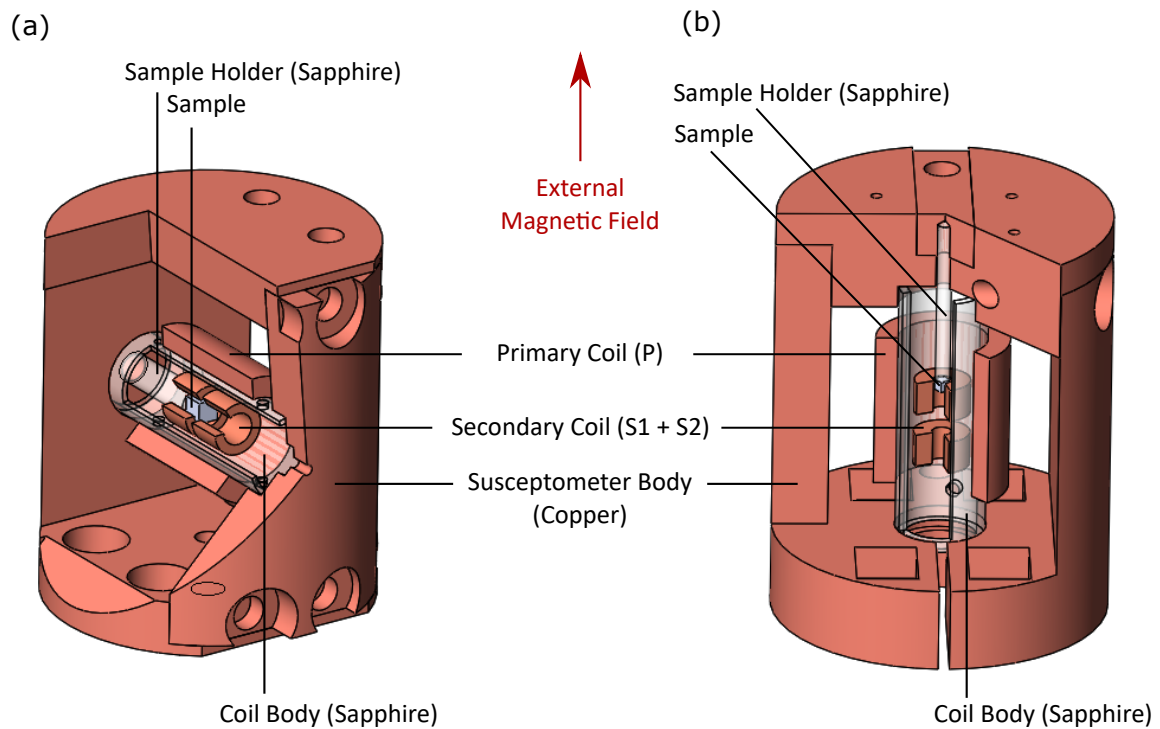
(a)

Sample Holder (Sapphire)

Sample

External
Magnetic Field

(b)

Sample Holder (Sapphire)

Sample

Primary Coil (P)

Secondary Coil (S1 + S2)

Susceptometer Body
(Copper)

Coil Body (Sapphire)

Coil Body (Sapphire)

Figure 1.1.: Schematic depiction of the low temperature susceptometers developed within this thesis. (a) Depiction of a susceptometer for transverse magnetic fields. The primary excitation coil (P) is wound onto a sapphire coil body which is attached to the copper susceptometer body. Free standing secondary coils (S1 + S2) are fixed inside the sapphire tube. The sample is mounted onto a sapphire rod to ensure thermal coupling to the bath. (b) Depiction of the corresponding configuration for measurements in longitudinal magnetic fields.

Both susceptometers are based on a support frame made from high purity oxygen free copper which provides a thermal anchor between the cryostat, the coils and the sample. The primary coil is wound onto a high purity single crystalline sapphire tube. This tube is thermally coupled to the copper frame and ensures the thermalisation of the primary coil. Single crystalline sapphire is used as thermal link for sample and coils, as metallic materials may generate unwanted eddy currents, preventing measurements at higher frequencies by generating a large parasitic signal. The primary coil is made from a 100 μm Rutherm VB 155 enamelled copper wire which was wound directly onto the sapphire tube. Two identical, commercially available free-standing coils, purchased from *Werap Wicklerei AG*, are used as a pair of balanced secondaries. They are attached to the inside of the former of the primary and, hence, thermally coupled to the cryostat. The free standing secondaries are used to maximize the volume fraction of the sample within the coil and thus, the recorded signal. The sample is glued onto a high purity single crystalline sapphire rod using GE Varnish and the rod is attached to the copper frame and

thermally coupled to the cryostat. Both susceptometers may be used in a variety of magnet cryostats (cf. section 1.2.5) and are suitable for large longitudinal and transverse static magnetic fields at temperatures down to below 30 mK.

1.2.2. Low Noise Susceptometer

A small drawback of the design of the susceptometer presented above is that the copper frame will generate a small parasitic signal, especially at larger frequencies. For measurements which require highest precision over a wide range of frequencies, all metallic materials in proximity of the susceptometer should be avoided. Figure 1.2 shows a susceptometer which was developed by the author as reported in [26] and refined within this study. In this case, the susceptometer consists of a polyether ether ketone (PEEK) body which is used as a primary coil former. The primary coil was wound directly onto the PEEK holder using a Meteor ME-301 coil winding
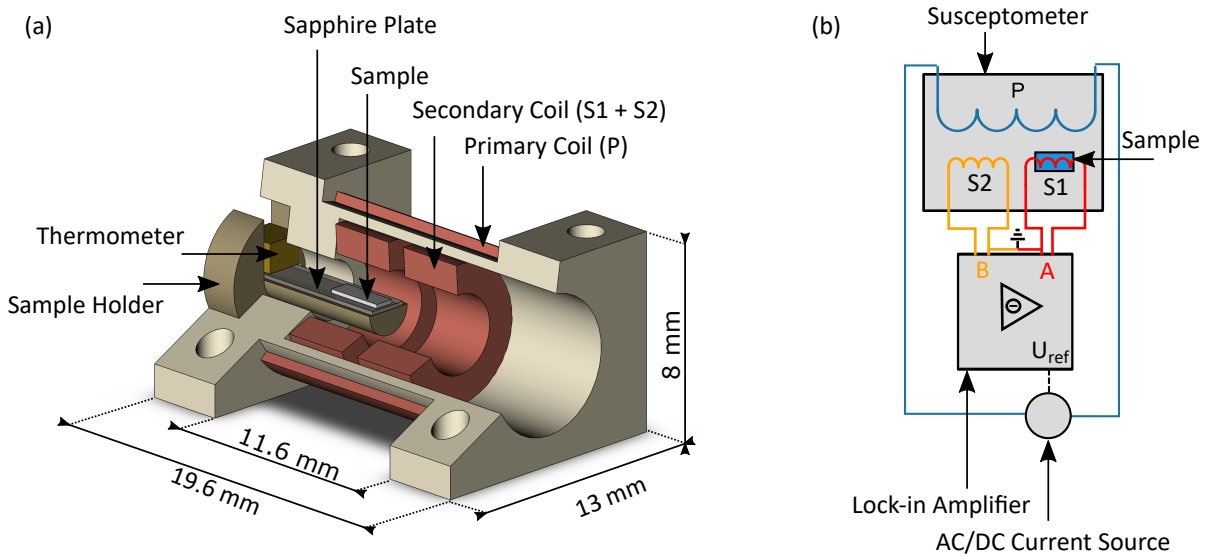
Figure 1.2.: Schematic depiction of the low noise susceptometer developed within this thesis and the corresponding measurement electronics. (a) Schematic depiction of the low noise susceptometer. The sample is mounted onto a 0.1 mm sapphire plate to ensure thermal contact with the thermometer. Susceptometer body and sample holder are manufactured from non-magnetic PEEK to reduce background noise. (b) Schematic depiction of the measurement electronics for all susceptibility measurements. A lock-in amplifier is used to record the voltage induced in both secondary coils (S1 + S2). The excitation field in the primary coil (P) is generated by an AC current source. The excitation frequency is provided to the lock-in amplifier as reference signal (U_{Ref}).

machine. A 100 μm Rutherm VB 155 enamelled copper wire was used to manufacture the primary coil. A set of two identical handmade secondaries are glued into the PEEK body. Detailed coil specifications for all susceptometers are summarised in table 1.1. A PEEK sample holder is used to which the sample is glued using GE varnish. As the thermalisation of the sample is purely achieved by exchange gas in this design, measurements are limited to temperatures down to $T \approx 1.4\,\mathrm{K}$. The cooling power of such a system is generally sufficient for most types of measurements. However, in certain applications, the cooling power of the gas flow might not be sufficient to thermalise the sample for temperatures below $\approx 30\,\mathrm{K}$ due to laminar gas flow. This is especially so for measurements with a large thermal load such as strong DC current generating ohmic heat (cf. chapter 3). Therefore, a small sapphire plate is attached to the sample holder on which the sample can be mounted. This sapphire plate is connected to the sample stick by a 1 mm silver wire, which serves as thermal anchor. Furthermore a sample thermometer is attached to the sapphire plate in order to detect the temperature as closely as possible to the sample.

Susceptometer	Coil	Windings	Res. (Ω)	Dimensions: l x d (mm)
TF	Primary	1497	168	16 x 8
TF	Secondary 1	1200	260	3.5 x 3
TF	Secondary 2	1200	260	3.5 x 3
LF	Primary	1432	161	16 x 8
LF	Secondary 1	1200	260	3.5 x 3
LF	Secondary 2	1200	260	3.5 x 3
Low Noise	Primary	1162	228.4	11.8 x 6
Low Noise	Secondary 1	704	83.8	3.85 x 2.3
Low Noise	Secondary 2	683	79.5	3.9 x 2.3

Table 1.1.: Overview of important parameters of the manufactured and purchased coils. The transverse field (TF) and longitudinal field (LF) susceptometers are manufactured using commercially available secondary coils with identical specifications. The coil dimensions refer to the coil length (l) and the inner diameter of the coil (d).

1.2.3. Detection Electronics

Figure 1.2 (b) shows a schematic depiction of the detection electronics used for both susceptometers. A Keithley 6221 alternating current source (A) was used to generate the oscillating magnetic field in the primary coil (P) and a Signal Recovery SR830 Lock-in Amplifier to pick up and subtract the voltages, induced in the secondary coils (S1 and S2). The output voltage of each channel is given as the convolution of the induced coil voltage $U_{\mathrm{ind},0}$ and the reference

signal $U_{r,0}$:

$$
\begin{aligned}
U_{\text{out}} &= \frac{1}{T} \int_0^T U_{\text{ind},0} \cos(\omega_m t + \varphi_m) U_{r0} \cos(\omega_r t + \varphi_r) \mathrm{d}t \\
&= \frac{1}{T} \int_0^T \frac{1}{2} U_{\text{ind},0} U_{r0} \cos(\omega_m t - \omega_r t + \varphi_m - \varphi_r) \mathrm{d}t - \\
&\quad \frac{1}{T} \int_0^T \frac{1}{2} U_{\text{ind},0} U_{r0} \cos(\omega_m t + \omega_r t + \varphi_m + \varphi_r) \mathrm{d}t
\end{aligned}
\tag{1.10}
$$

A low-pass filter, provided by the SR 830 lock-in amplifier, cancels out all signals exceeding the cut-off frequency $f_c = \frac{1}{2\pi T}$ leaving only low frequency contributions.

$$
U_{\text{out}}^{\text{LP}} = \frac{1}{T} \int_0^T \frac{1}{2} U_{m0} U_{r0} m \cos(\omega_m t - \omega_r t + \varphi_m - \varphi_r) \mathrm{d}t \tag{1.11}
$$

$$
\approx \frac{1}{2} U_{m0} U_{r0} m \cos(\varphi_m - \varphi_r) \tag{1.12}
$$

The signal observed this way is phase-locked to the excitation frequency of (A), leaving only contributions to the measurement signal, at $\omega_r = \omega_m$. The resulting voltage U_{out}^{LP} is then proportional to the real part of the susceptibility $\mathrm{Re}\chi$. A second phase-locked amplifier with $90°$ phase shift was used to record the imaginary part of the susceptibility, $\mathrm{Im}\chi$, simultaneously.

1.2.4. Susceptometer Calibration

Theoretically, the mutual inductance method, discussed in section 1.1.2, may provide an absolute susceptibility signal in SI units, given all variables in equation 1.8 are known. Some of theses parameters, however, such as the exact filling factor f, the excitation field H_{AC} or the cross-section A may only be approximated, introducing systematic errors of the measured susceptibility value. Therefore, a calibration was performed for each susceptometer presented above. For this purpose, two samples were investigated in a commercially available *Quantum Design Physical Properties Measurement System* (PPMS).

One measurement of the susceptibility in zero magnetic field was performed as a function of temperature between $T = 2\,\text{K}$ and $T = 5\,\text{K}$ for LiHoF$_4$ and between $T = 20\,\text{K}$ and $T = 60\,\text{K}$ for MnSi, both in the PPMS as well as with our bespoke susceptometers. The induced voltage U_{ind} in the susceptometer, detected by the lock-in amplifier (cf. section 1.1.2), could then be scaled to fit the susceptibility signal recorded by the PPMS, χ_{PPMS}, using:

$$
\chi = \chi_{\text{PPMS}} = \beta \cdot U_{\text{ind}} + \gamma. \tag{1.13}
$$

Here, $\beta = (H_0 \omega A N_s f)^{-1}$ is a linear scaling factor, where all parameters are specific to the susceptometer, as defined in equation 1.8. The parameter γ accounts for imperfect balancing of

the secondary coils, which cannot be avoided. Figure 1.3 shows the real part of the susceptibility as measured by the PPMS, χ_{PPMS}, as reference signal in SI units and the scaled induced voltage U_{ind} of the bespoke susceptometers as a function of temperature for a LiHoF$_4$ sample (a) and for a MnSi sample (b). U_{ind} was scaled and shifted by the factors $\beta = 2379.74\,\mathrm{V}^{-1}$ and $\gamma = -0.0004$ for LiHoF$_4$ and by the factors $\beta = 15388.76\,\mathrm{V}^{-1}$ and $\gamma = -0.103$ for MnSi, as indicated within figures 1.3 (a) and (b). The low γ contribution hereby indicates well balanced secondaries, while the value of β agrees well with a straight forward estimation of this parameter using the specific parameters of each susceptometer.
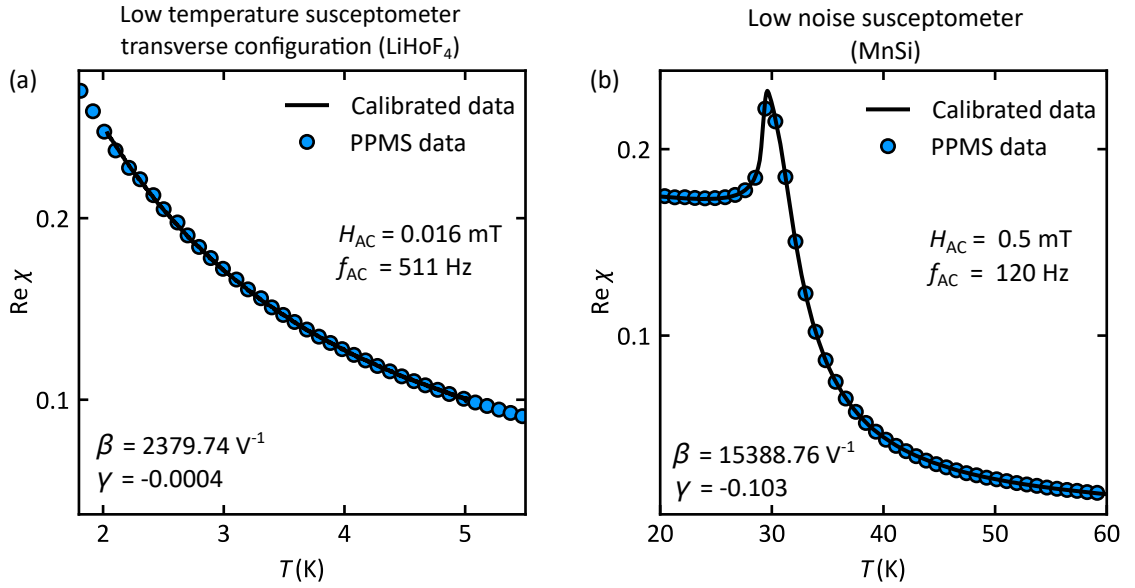
Figure 1.3.: Calibration curves for both types of susceptometers. (a) Measurement of the induced voltage in the transverse low temperature susceptometer. The susceptometer was loaded with a spherical LiHoF$_4$ sample (cf. section 2.2.1). The induced voltage was scaled by a factor of β with an offset γ (black line, calibrated data) to fit the PPMS reference data (blue dots, PPMS data). (b) Corresponding measurement of the induced voltage in the low noise susceptometer. The measurement was performed using a cubic MnSi sample (cf. section 3.2.1).

1.2.5. Sample Environment

In this study, measurements of the magnetic susceptibility are presented as a function of magnetic field and temperature. Two types of superconducting magnet systems were used in combination with different cryogenic inserts providing variable magnetic fields and temperature control as described in the following.

a) 16 T Superconducting Magnet System

A major part of the measurements were carried out using a conventional Oxford Instruments ^{4}He bath cryostat. The cryostat was equipped with a bipolar superconducting magnet providing magnetic fields up to $B = \pm 16\,\mathrm{T}$ along the vertical axis of the cryostat. The bath cryostat may be used in combination with a Variable Temperature Insert (VTI), as well as a JT Dilution Refrigerator Insert (JT).

b) 2D Vector Magnet

For the study of LiHoF$_4$ presented in chapter 2.3 an American Magnetics 2D superconducting magnet system was used. This system provides up to $B = \pm 9\,\mathrm{T}$ along the vertical (z-)axis and up to $B = \pm 4.5\,\mathrm{T}$ along the horizontal (y-)axis. As both coil systems may be controlled independently, this system allows to generate a magnetic field vector between $B = 4.5\,\mathrm{T}$ and $B = 9\,\mathrm{T}$ pointing along any arbitrary direction on the z-y plane. This allows for a very accurate adjustment of the angle between the magnetic field axis and a certain crystallographic direction of a sample, despite possible misalignments of the sample. This proves to be essential for the measurements presented in chapter 2, where the suppression of magnetic order of the Ising ferromagnet LiHoF$_4$ in a transverse magnetic field is discussed.

c) Variable Temperature Insert (VTI)

For the measurements on MnSi, presented in chapter 3, a conventional *Oxford Instruments* variable temperature insert with a temperature range from $1.5\,\mathrm{K}$ to $300\,\mathrm{K}$ was used. In this system, a needle valve at the bottom of the insert controls the ^{4}He gas flow through the insert, while a heater adjusts the temperature of the gas. In standard operation, once the desired temperature is stabilised, the PID controller reduces the heater power to a previously defined value. To keep the temperature constant during this process, the gas flow is reduced accordingly. This, however, results in a variation of the cooling power while the temperature remains constant. In the presence of ohmic heating, this effect is undesirable and results in systematic errors which are discussed in more detail in chapter 3. To avoid such variations in cooling power, the needle valve was kept at a constant value during all measurements and temperature control was only carried out by adjusting the heater output.

d) Joule-Thompson ^{3}He/^{4}He Dilution Refrigerator Insert (JT)

For studies below $1.5\,\mathrm{K}$, a Joule-Thompson ^{3}He/^{4}He dilution refrigerator insert purchased from *Oxford Instruments* was used. Such types of cryostats comprise several cooling stages. First, the ^{3}He/^{4}He mixture is pre-cooled in a nitrogen-trap and in an $4\,\mathrm{K}$ heat exchanger, which is coupled to the main ^{4}He bath. A Joule-Thompson expansion stage is used to pre-cool and condense the ^{3}He/^{4}He mixture further to a temperatures $T \approx 1\,\mathrm{K}$. Below $T = 850\,\mathrm{mK}$, the mixture separates

into a ^{3}He rich and a ^{3}He poor phase. Following this, cooling is achieved by a quasi evaporation of ^{3}He atoms from the ^{3}He rich into the ^{3}He poor phase, the so-called *dilution* [26–29]. This specific system used in this study is able to achieve temperatures as low as $T = 30$ mK. The cooling power of this system was determined to be above $P = 40$ μW at $T = 100$ mK. As part of this thesis, the JT insert was adapted to fit several magnet environments available to our group, including the 2D vector magnet as well as a 20 T magnet system.

1.2.6. Measurement Automation

The Labview-based measurement automation software **CryoTUM**, which has been developed over the past years in our group [26, 30] was completely restructured to meet the requirements of the new measurement options and new equipment used in this thesis. A complete description of the software exceeds the scope of this thesis. Hence, only the most important changes and improvements will be summarised in the following. A schematic overview of the measurement program is shown in figure 1.4.

First, a new user interface (*system monitor*) was developed to permit control of the magnet systems, the cryogenic inserts as well as the detection electronics simultaneously from a single front panel. The monitor constantly logs all relevant parameters during operation to permit error tracking and debugging. Additionally, the monitor provides several independent possibilities to view and evaluate data during the experiment, providing a live view. Furthermore, measurement routines may be started and controlled by the *system monitor*.

Second, control and communication with the cryogenic systems and magnet has been separated completely from the *system monitor* and other *measurement routines*. It is now provided by independent instrument-specific *monitors*. In this way, the *measurement routines* and the *system monitor* may be used separately and timed precisely, as they are independent from the response times of the equipment. Additionally, the new structure facilitates the integration of new experimental equipment or cryogenic systems. The possibility for the *system monitor* and the *measurement routines* to control the monitors is now provided using instrument clusters, which are passed to the *monitors* using *queues*. The use of more complicated, Labview-specific *queues* instead of global variables was necessary to avoid so-called race conditions which might occur, when the *system monitor* and a *measurement routine* simultaneously try to control a specific instrument *monitor*.

In the context of this thesis, the restructuring of the measurement software was necessary to be able to combine all cryostat and magnet options, presented above, as well as to ensure accurate measurement timing. Additionally, new equipment could be integrated to provide additional measurement parameters such as variable excitation currents and frequencies.
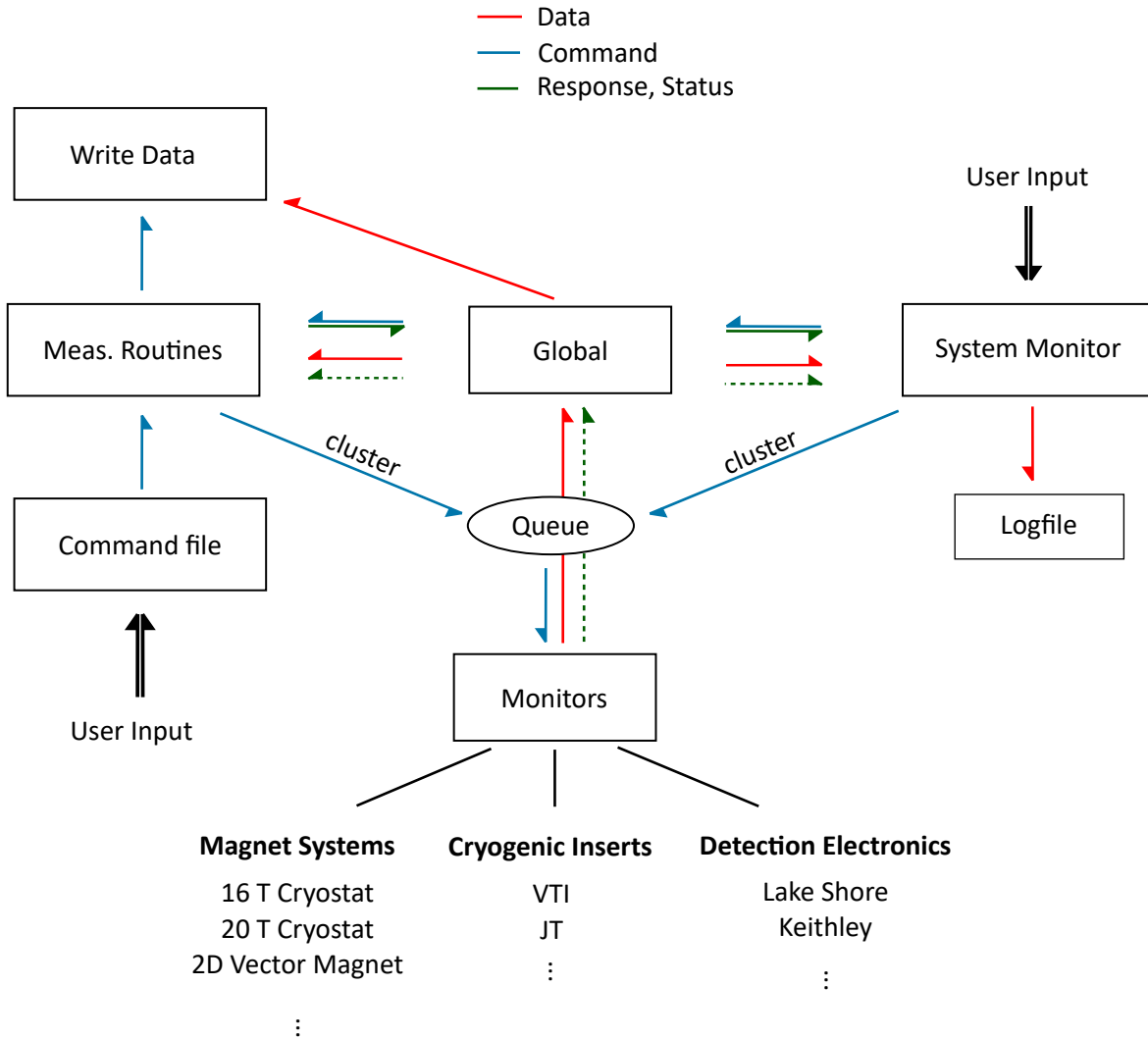
Figure 1.4.: Schematic overview over the restructured, Labview-based, measurement automation software **CryoTUM**. The depiction visualises the data and command flow within the software and summarises the most important functions. A central part is the *system monitor* which provides control of *measurement routines*, instruments and equipment and provides a live view of the collected measurement data. Global variables (*global*) are used to store the collected measurement data and pass commands from the *system monitor* to the *measurement routines*. Commands from the *measurement routines* and the *system monitor* are passed to the *monitors* using instrument-specific clusters which are passed into *queues* to avoid race conditions.

Quantum Phase Transition in the Ising Ferromagnet LiHoF$_4$

In this chapter, fundamental aspects of the transverse field-tuned quantum phase transition in the model magnet LiHoF$_4$, as investigated by means of magnetic AC susceptometry, are presented. In the literature, LiHoF$_4$ is portrayed as one of the simplest text book examples of a quantum phase transition. The investigation of such simple systems offers access to the generic properties of quantum phase transitions and the quantum critical regime, as the basis for the identification of new exotic states and complex phases of matter. In the case of LiHoF$_4$, various experimental studies claimed excellent agreement with the theoretical predictions for this kind of quantum phase transition. However, significant discrepancies between theory and experiment still indicate an incomplete picture and motivate further investigations.

This chapter is structured as follows. First, the fundamental theoretical concept of quantum phase transitions is introduced, followed by an overview of related experimental observations. The introduction concludes with a detailed presentation of the current state of research on the low temperature properties of LiHoF$_4$. Following this, details of the samples investigated and the experimental methods as well as the associated experimental uncertainties are discussed. Next, the experimental results are presented in two parts. First, details of the phase transition, such as the dependence on angular variations of the magnetic field, are investigated and compared to previous studies. Second, the properties of the ordered ferromagnetic state, in particular the question of domain-wall dynamics and the influence of a strong hyperfine coupling are addressed. The chapter concludes with an interpretation of our results and a summary.

2.1. Quantum Phase Transitions

2.1.1. Concept and Framework of Quantum Phase Transitions

Over the past couple of decades, a number of books and review papers have been published that present comprehensive introductions to physical concepts associated with quantum phase transitions [31, 32]. In the following the most important aspects as relevant to this thesis are reviewed. The presentation follows references [8, 10, 32].

A quantum phase transition (QPT) is a continuous transformation of a system from an ordered into a disordered state at zero temperature. Alternative definitions of quantum phase transitions are, a transition driven by quantum fluctuations, or a transition characterized by a change of macroscopic quantum entanglement. The QPT is hereby controlled by a non-thermal parameter g such as chemical doping, pressure or, applied magnetic field. In the simplest case the associated phases are characterised by an order parameter which is zero at one side of the transition, and non-zero on the other side. In case of a ferromagnetic QPT, the magnetization $\boldsymbol{M}$ represents this order parameter. However, the choice of the order parameter may be considerably more subtle in other transitions, such as metal-insulator transitions [33], where the correct order parameter is still a matter of debate [34, 35].
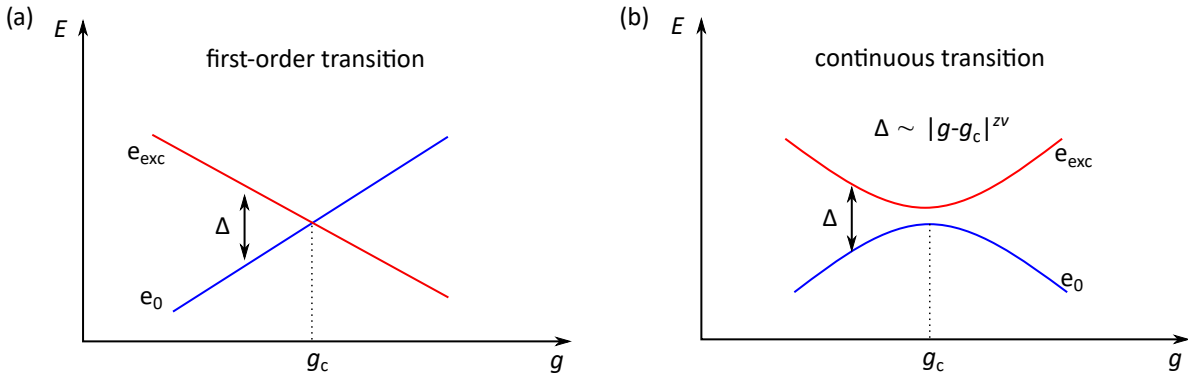
Figure 2.1.: Eigenvalues E of a Hamiltonian as a function of an external tuning parameter g. (a) Energies of the ground and the first excited states of a first-order transition. The transition exhibits a level-crossing at $g = g_c$ where an excited state e_{exc} becomes the new ground state. The order parameter exhibits a discontinuous jump. (b) Energies of the ground and the first excited states of a continuous phase transition. Continuous transitions show an avoided level-crossing in any finite lattice. In the infinite lattice limit, the energy gap Δ goes to zero as $\Delta \sim |g - g_c|^{\nu z}$, leading to a diverging correlation length ξ and a continuous change of the order parameter. Figure adapted from ref. [10].

From a theoretical point of view, a quantum phase transition is a point of non-analyticity of the ground state energy of the system at $g = g_c$. If this non-analyticity originates in a level-crossing of the eigenstates, the system transits discontinuously from one ground state into another, characteristic of a first order transition (cf. figure 2.1 (a)). More commonly, however, the non-analyticity originates in an avoided level-crossing in the limiting case of an infinite lattice, resulting in a continuous (second-order) phase transition (cf. figure 2.1 (b)). In the following, we focus our discussions on such quantum critical transitions. In this case, let Δ be the energy of the lowest excited state. For any value $g \neq g_c$ the first excited state will be separated from the ground state by a non-zero energy gap $\Delta \neq 0$. However, when approaching the quantum critical point (QCP) at $g = g_c$ in the infinite lattice limit, Δ vanishes as

$$\Delta \sim |g - g_c|^{z\nu}, \tag{2.1}$$

where, $z\nu$ is a universal critical exponent. Even though the order parameter in the disordered phase is zero in the thermodynamic average, non-zero order parameter fluctuations might be present. In fact, when approaching the critical point and as Δ vanishes, the spatial correlation length ξ of the order parameter fluctuations diverges as

$$\xi \sim |g - g_c|^{-\nu}, \tag{2.2}$$

with ν being the same critical exponent as in equation 2.1. Together with the spatial correlations ξ, the lifetime of the fluctuations, τ, diverges, approaching g_c as

$$\tau \sim |g - g_c|^{-z\nu}. \tag{2.3}$$

As a consequence, microscopic details of the Hamiltonian become irrelevant and the system is said to be scale-invariant.

This is in analogy to classical critical phenomena as studied extensively over the past decades. Comprehensive introductions to classical critical phenomena may be found in references [36–38]. Both the quantum and the classical critical regimes may be classified by a set of universal critical exponents which lead to universal macroscopic behaviour of intrinsically different physical systems. As a consequence, different types of phase transitions might exhibit equivalent critical exponents depending only on macroscopic parameters such as the type of the order parameter or dimensionality of the system. Except for the critical exponents ν and z, which have been introduced above, there exist a set of critical exponents connected to the order parameter of the system and to the field conjugate of the order parameter. Relevant critical exponents are briefly summarized in table 2.1. Note that these exponents are not independent, but connected by the so-called scaling relation

$$2 - \alpha = 2\beta + \gamma \tag{2.4}$$

and the hyperscaling relation

$$2 - \alpha = d\nu \tag{2.5}$$

with α, β and γ being the critical exponents of specific heat, order parameter and susceptibility, as defined in table 2.1 and d the dimensionality of the system. Note that the critical exponent of the correlation time z is not affected by the scaling relations and completely independent from all other exponents.

	Exponent	Definition
Specific heat	α	$C \sim |g - g_c|^{-\alpha}$
Order parameter	β	$m \sim (g_c - g)^{\beta}$
Susceptibility	γ	$\chi \sim |g - g_c|^{-\gamma}$
Correlation length	ν	$|g - g_c|^{-\nu}$
Correlation time	z	ξ^z

Table 2.1.: Overview of important critical exponents at a continuous quantum phase transition. Only exponents connected to the order parameter in the context of this work are shown.

Even though the scaling laws are valid for all continuous phase transitions, including classical phase transitions, it is important to note that the description of quantum phase transitions given above is only valid for the ground states and hence at absolute zero temperature. Nevertheless, the physical properties of a system close to g_c at non-zero temperature will be influenced strongly by the existence of the critical point at g_c.

The properties around a QCP at non-zero temperature are dominated by two relevant energy scales. First, the thermal energy of the system, given by $k_B T$, and second the energy of long-range order parameter fluctuations, given by $\hbar \omega_c$. We know from equation (2.3) that the characteristic time scale of such fluctuations diverge at the QCP. Consistently, the characteristic energy scale will vanish approaching g_c

$$\hbar \omega_c \sim |g - g_c|^{\nu z} \tag{2.6}$$

The phase diagram in figure 2.2 exhibits three different regions, separated by dashed crossover lines which correspond to $T \sim |g - g_c|^{\nu z}$. For $g \ll g_c$, a thermally disordered regime is observed. Here, the order is destroyed by classical thermal fluctuations of the order parameter and the energy gap Δ remains larger than the thermal energy, $\Delta \gg k_B T$. At low enough temperatures, an ordered phase might be observed, depending on the dimensionality of the system. Note, however, that the transition line of the ordered phase remains entirely classical down to lowest
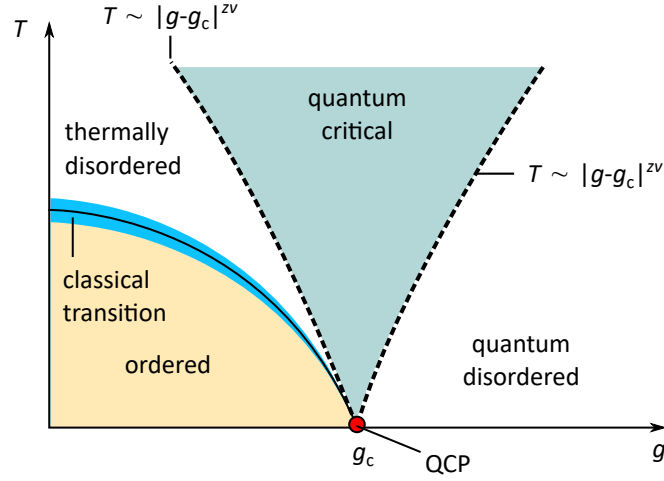
Figure 2.2.: Phase diagram of a typical quantum phase transition with dimensionality $d \geq 2$. The transition is controlled by a non-thermal tuning parameter g. The system exhibits an ordered state at low temperatures and small g which is transformed into a quantum disordered state as a function of g above the quantum critical point (QCP) at $g = g_c$. A V-shaped quantum critical region evolves above the QCP in which thermal excitations can couple directly to the entangled quantum states, leading to peculiar new behaviour.

temperatures, as $|g - g_c| < T_c^{1/\nu z}$ (cf. blue shaded region in figure 2.2). In both the ordered, as well as the thermally disordered state, the system is dominated by so-called elementary excitations, which posses a well-defined energy. Such particle-like states have been studied extensively over the past century and represent an important theoretical concept in our understanding of classical solid state physics. For $g \gg g_c$, a quantum mechanically disordered regime is observed in which the physics is governed by quantum fluctuations, resembling the quantum mechanical nature of the ground state. Nevertheless excitations by thermal fluctuations can be treated quasi-classical as they have no access to entangled quantum states, as $\Delta \gg k_B T$.

Most interesting, however, is the quantum critical regime enclosed by the dashed lines in figure 2.2. Here quantum fluctuations and thermally excited fluctuations have comparable energy scales, $\hbar \omega_c \sim k_B T$. As $\Delta \lesssim k_B T$, thermal excitations can couple directly to quantum-critical entangled states leading to peculiar new phenomena like non-Fermi liquid behaviour of metals or unconventional superconductivity. Furthermore, classical particle-like excitations are absent and replaced by a continuum of quantum fluctuations, and none of the theoretical methods of condensed-matter physics yield an accurate description, except for some special cases in lower dimensions. Surprisingly, the quantum critical nature of this regime is often enhanced with increasing temperature [8, 39], making this region, in contrast to the QCP, well accessible for experiments and facilitates the experimental investigation of quantum mechanical effects. Note,

however, that the quantum critical behaviour breaks down as the thermal energy exceeds the spin-spin interaction and microscopic details retain their importance due to the vanishing correlation length [8].

2.1.2. Experimental Studies of Quantum Phase Transitions

First experimental work on QPT was stimulated by the observation of non-Fermi liquid (NFL) behaviour in metallic magnets in the early nineties. First examples include the Kondo-alloy $Y_{1-x}U_xPd_3$ [40] and the heavy-fermion system $CeCu_{6-x}Au_x$ [41], in which a breakdown of the Fermi-liquid theory of metals could be observed as a function of chemical doping. Simultaneously, similar observations were reported for several intermetallic compounds such as $ZrZn_2$ [42] or MnSi [43, 44], in which ferromagnetic order could be suppressed by the application of hydrostatic pressure, allowing for a more controlled tuning of the phase transition as compared to chemical doping. Consecutive studies additionally revealed a metamagnetic transition as a function of an applied magnetic field, resulting in a quantum critical end point (QCEP) [45–48]. A schematic depiction of a generic phase diagram of such a systems is shown in figure 2.3 (a). The magnetic field and pressure dependence of MnSi will be discussed separately in chapter 3.1.1. Following these observations, the possibility of new types of emergent phases mediated by quantum criticality was discussed and the idea was further supported by the observation of an
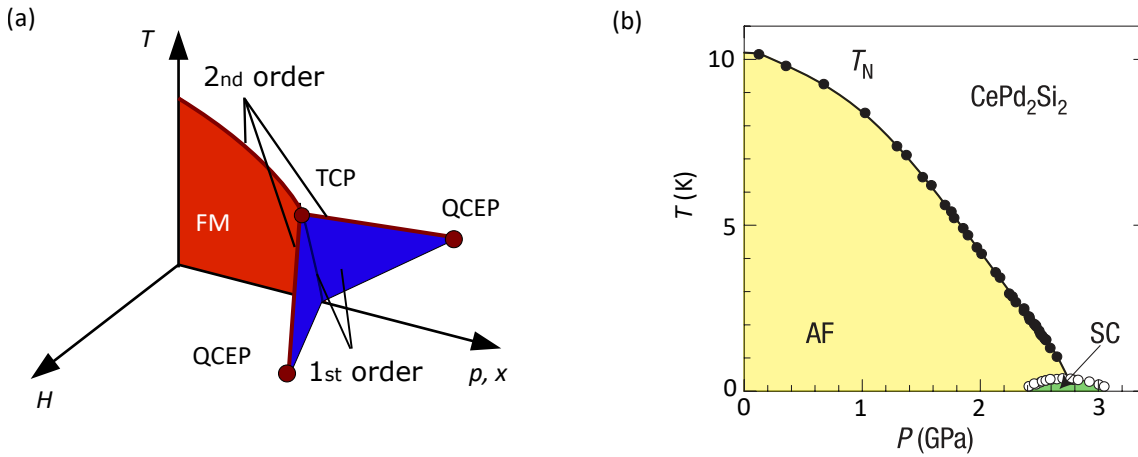
Figure 2.3.: Experimental observations of quantum phase transitions. (a) Schematic depiction of a typical phase diagram as a function of Temperature T, magnetic field H and pressure p or composition x, as observed in compounds such as MnSi, $ZrZn_2$ or UGe_2. Ferromagnetic order is suppressed by a non-thermal tuning parameter. A quantum critical point is avoided and wings of first order transitions emerge as a function of the magnetic field H, leading to a quantum critical end point (QCEP). Figure adapted from reference [31]. (b) Magnetic phase diagram of $CePd_2Si_2$ as inferred from electrical resistivity measurements. Antiferromagnetic order (AF) is suppressed by hydrostatic pressure and a dome of unconventional superconductivity (SC) emerges in the vicinity of a QCP. Figure taken from reference [49].

emergent dome of unconventional superconductivity in the vicinity of a pressure-induced quantum critical point in compounds such as $CePd_2Si_2$ (cf figure 2.3) or $CeIn_3$ [2, 50–55]. Since then, a large number of quantum phase transitions could be identified in similar metallic systems and quantum criticality became a roadmap towards the identification of emergent phenomena and complex new phases. However, despite the extensive theoretical and experimental efforts, many aspects of metallic quantum criticality remain an open topic in condensed matter theory [31, 48, 49, 56, 57].

In contrast, the theoretical framework is much more simple in certain types of insulating systems. On illustrative example is the Ising model in a transverse field. In their pioneering work, Bitko *et al.* [9] reported the suppression of ferromagnetic order by the application of a magnetic field, applied perpendicular to the magnetic Ising-axis, in the insulating Ising ferromagnet $LiHoF_4$, as predicted theoretically. The investigation of the low temperature properties of this compound will be the focus of this chapter and a comprehensive introduction to the state of research on this system is given in the next section. Other examples of insulating QPTs include the quasi 1D Ising-chain compound $CoNb_2O_6$ [58], where magnetic order can be suppressed by a magnetic field and the complex E_8 symmetry emerges in the vicinity of the QCP, as well as the Bose-Einstein condensation of dilute magnons in $TlCu_2Cl_3$ [59, 60], where quantum criticality is either mediated by a magnetic field, or by hydrostatic pressure. Even though such model systems represent particularly simple examples of quantum criticality as compared to their metallic counterparts, their investigation offers a detailed insight into fundamental concepts and properties of QPTs.

2.1.3. Transverse Field Tuned Quantum Phase Transition in LiHoF$_4$

In $LiHoF_4$, long range ferromagnetic order, which appears below a Curie temperature of $T_c = 1.53 \, \text{K}$, may be suppressed in a quantum phase transition by a magnetic field, applied perpendicular to the magnetic easy-axis, resulting in the well known magnetic phase diagram, depicted in figure 2.4 (a) [9]. The compound belongs to the isostructural group of lithium fluorides, $LiR_xYb_{1-x}F_4$, with R being a rear-earth metal, all crystallising in the tetragonal scheelite structure $I4_{1/a}$ [61]. Below T_c, ferromagnetic order appears, where the ordering process is dominated by magnetic dipole interactions, attributed to the partially filled $4f$ shells of the Ho^{3+} atoms [62]. The system exhibits an easy magnetic axis along the crystallographic c-direction, along which needle-shaped domains form. The ground state is a $^5I_8$ doublet, with the first excited state at approximately $11 \, \text{K}$ [63].

The strong uniaxial character of the ferromagnetic order of $LiHoF_4$ makes a theoretical description as an Ising-ferromagnet possible, where the degenerate ground states represents the *spin-up* and the *spin-down* configurations of the Ising Hamiltonian. Under an applied magnetic
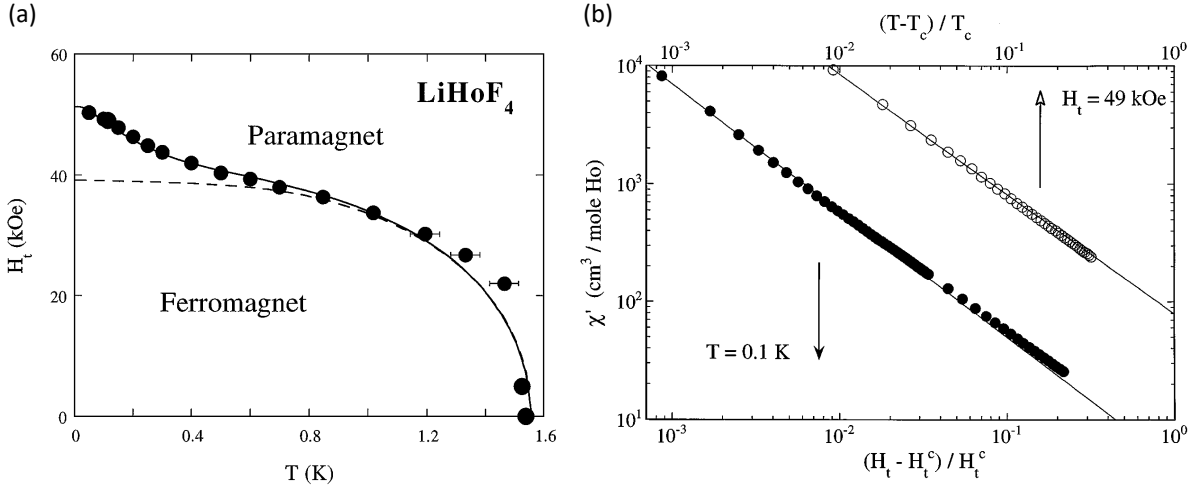
Figure 2.4.: Key characteristics of the transverse-field Ising transition in LiHoF$_4$. (a) Magnetic phase diagram of LiHoF$_4$, inferred from AC susceptibility. Ferromagnetic order is observed below a critical temperature $T_c \approx 1.53$ K. This order can be suppressed in a quantum phase transition as a function of a transverse magnetic field H_t above a critical field value of $\mu_0 H_c \approx 4.9$ T. (b) Field and temperature dependence of the real part of the AC susceptibility when approaching the classical transition at T_c as well as the quantum phase transition at H_c. In both cases the susceptibility diverges exponentially with a critical exponent $\gamma \approx 1$, indicating a mean-field transition. Figures taken from reference [9].

field perpendicular to the Ising direction, the field will induce fluctuations between the two spin-states and tune an order-disorder transition at $T = 0$. This motivates a description in terms of a Hamiltonian given by

$$\mathcal{H} = J \sum_{ij} \sigma_i^z \sigma_j^z + \Gamma \sum_i \sigma_i^x, \tag{2.7}$$

where J is the dipolar coupling, Γ the external transverse field and σ_i the Pauli matrices.

The theoretical investigation of such transitions dates back to the early sixties, when de Gennes considered the order-disorder transition in ferroelectrics [64]. Later on it was established that zero-temperature Ising quantum phase transitions, as observed in LiHoF$_4$, in d-dimensions, belong to the same universality class as the classical $(d + 1)$-dimensional Ising model [65–68]. A recent overview of theoretical models of quantum Ising systems may be found in reference [69]. In LiHoF$_4$, this so-called quantum-classical mapping was justified in terms of the critical exponent $\gamma \approx 1$ of the AC susceptibility down to temperatures of 3% above T_c (cf. figure 2.4 (b)), indicating a mean-field character of the quantum-phase transition [10, 67]. Accordingly, Bitko *et al.* interpret the path of the B/T transition line above $T = 0.6$ K in terms of a classical

mean-field model of a spin $\frac{1}{2}$ magnet in a transverse field, where

$$\coth\left(\frac{\Gamma}{2k_B T_c}\right) = \frac{J}{\Gamma}. \tag{2.8}$$

The resulting curve is shown as dashed line in figure 2.4 (a). Evidently, below $T = 0.6\,\mathrm{K}$ this curve does not represent the experimental data and an additional contribution, attributed to the hyperfine coupling of the applied field to the nuclear spins of the Ho ions is observed [9, 70, 71]. To account for this effect, Bitko and co-workers proposed an effective mean-field Hamiltonian using two free parameters, the transverse g-factor, $g_\perp$, and an effective dipole coupling strength $\mathcal{J}_0$,

$$\mathcal{H} = V_c - g_\perp \mu_B H_t \mathbf{J}_x + A(\mathbf{I} \cdot \mathbf{J}) + 2\mathcal{J}_0 \langle \mathbf{J}_z \rangle \mathbf{J}_z, \tag{2.9}$$

where V_c is a crystal field contribution and A the hyperfine interaction. Using this Hamiltonian, they were able to fit their experimental data successfully and present a complete theoretical description of the phase transitions in LiHoF$_4$ with best fit values for the effective coupling $\mathcal{J}_0 = 0.0270 \pm 0.0005\,\mathrm{K}$ and the transverse g-factor $g_\perp = 0.74 \pm 0.04$ (cf. solid line in figure 2.4 (a)).

In 2004, a theoretical study reported by Chakraborty *et. al* [63], a full microscopic Hamiltonian was considered as the basis of quantum Monte Carlo simulations to reproduce the experimentally observed magnetic phase diagram. As an additional aspect a small antiferromagnetic exchange interaction was taken into account as a free parameter. As their main result, the authors were able to reproduce the experimental findings from reference [9] qualitatively, including the correct transition temperature of $T_c = 1.53\,\mathrm{K}$. However small discrepancies around the classical ferromagnetic transition at small magnetic fields were observed and attributed to either an incomplete microscopical model of the system, or possible deficits in the theoretical tools [63].

More recently, Rønnow *et. al* investigated the excitation spectrum of the quantum phase transition in LiHoF$_4$ [71]. The authors were able to confirm a mode softening, when approaching the critical field H_c. This softening, however, remained incomplete with a residual energy-gap of $\Delta = 0.24\,\mathrm{meV}$, attributed to the mixing of nuclear and electronic spin contributions, which stabilise the magnetic order at a higher fields than expected, prohibiting a diverging correlation length. In a consecutive study [72], the authors proposed an effective-medium theory, noting that such mixed electronic and nuclear spin states may lead to combined modes with diverging correlation lengths at much lower energies ($< 10\,\mu\mathrm{eV}$) than observed in their study. Nevertheless, to obtain theoretical results in agreement with the experimental observations, the authors still had to scale the calculated energies by a factor of 1.15. They argued that this scaling may be attributed either to the effects of domain walls or to magnetoelastic coupling.
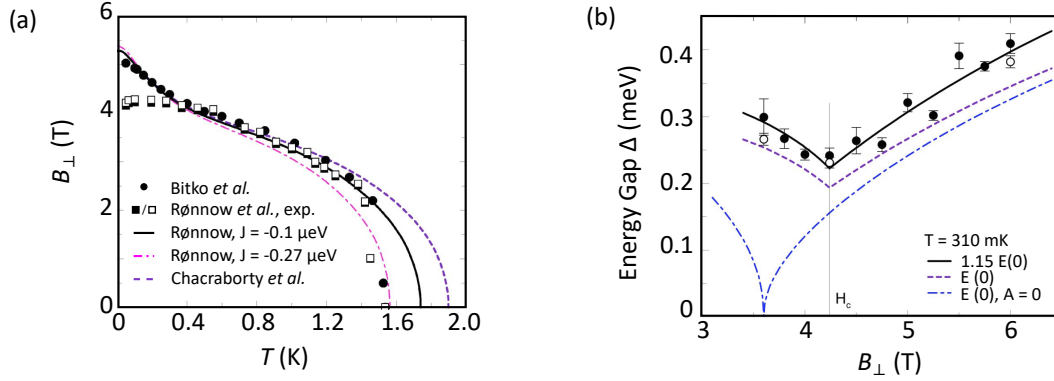
Figure 2.5.: Results of recent neutron scattering experiments on LiHoF$_4$ by Rønnow *et al.* [71, 72]. (a) Comparison between recent theoretical calculations by Rønnow and Chakraborty to the experimentally inferred phase diagram by Bitko *et al.* [9, 63, 72]. Using an additional free parameter J, representing an exchange coupling term, the experimentally inferred phase diagram can not be accounted for completely. (b) Energy gap of low lying excitations inferred from inelastic neutron scattering experiments [71]. The expected vanishing of the gap Δ at the QCP could not be observed. The incomplete mode-softening is attributed to strong hyperfine coupling.

Given that both Chakraborty as well as Rønnow were not able to present a complete theoretical explanation for the observed experimental data, without using free scaling parameters, Tabei *et. al* [73] revisited the microscopic Hamiltonian using a pertubative quantum Monte Carlo technique in order to resolve the remaining discrepancies. Based on their study, they concluded that the microscopic picture of LiHoF$_4$ remains incomplete, as they were able to exclude possible deficits in the theoretical tools, as one of the proposed reasons in reference [63]. Unfortunately, they were note able to modify the microscopic Hamiltonian to account for the complete phase diagram of the experimental data.

To confirm the theoretical picture presented by Rønnow *et al.* experimentally, Legl and co-workers investigated the magnetization M_x of LiHoF$_4$ along a magnetic hard axis as a function of the applied magnetic field along the same axis for various temperatures [74]. They compared their results, shown in figure 2.6 (b) and (d), to theoretical calculations by Rønnow, shown in figure 2.6 (a) and (c). While the calculations would predict a sharp transition at B_c, Legl and co-workers observed a broadening of the transition for temperatures below $T \leq 800\,\mathrm{mK}$. Interestingly, this broadening appears, at similar temperatures, at which the hyperfine coupling appears to gain importance. Legl concluded that his observations are not consistent with the theory presented by Rønnow and proposed an alternative scenario, in which the observed broadening is connected to a thermal broadening caused by the nuclear excitation spectrum. Confirmation
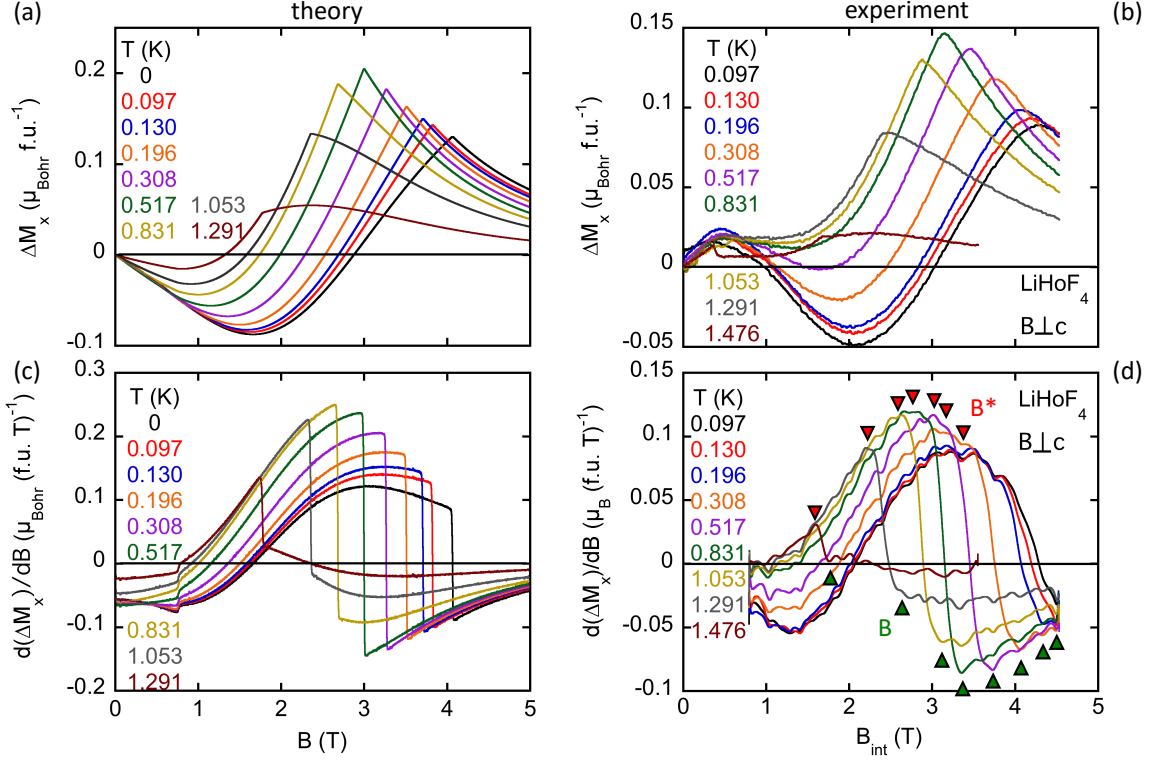
Figure 2.6.: Comparison between theoretical calculations by Rønnow *et al.* and experimental observations of the magnetization component M_x of LiHoF$_4$ by Legl *et al.* [74]. (a), (c) Change of the magnetization M and static susceptibility dM/dB along the magnetic hard x-axis with a magnetic field, applied along the same axes. dM/dB exhibits a distinct jump at the transition field B_c which shifts towards higher fields with decreasing temperature. (b), (d) Experimental observations of the same quantities. Here the jump in dM/dB broadens as the temperature is reduced, indicating a mismatch between theory and experiment at low temperatures.

of this effect would represent a first example of a thermal effect of the nuclear spin bath on an electronic system.

The inconclusive theoretical descriptions, taken together with several experimental studies suggest an inconsistent account of the nature of the magnetism and the phase transitions in LiHoF$_4$ at low temperatures. First, the incomplete mode softening observed in neutron scattering data which presents reasonable doubt, if the field tuned phase transition is really of continuous nature. Second, the strong discrepancies between theory and experiment close to the classical phase transition at small applied magnetic fields as well as the observed broadening of the transition at low temperatures, as reported by Legl *et al.*, still indicate an incomplete microscopic description. This motivated to revisit the transverse susceptibility, reported first by Bitko *et. al* [9], focussing in detail on the unresolved theoretical issues.

2.2. Experimental Methods

An overview of the experimental methods used in this thesis has already been given in chapter 1. In this section, specific aspects of the experimental methods used in the measurements of the transverse susceptibility of LiHoF$_4$ are summarised. First, the properties of the sample and the sample holder are introduced, then, measurement uncertainties, arising from magnetoresistance effects of the temperature sensors, are addressed.

2.2.1. Sample Properties and Sample Mount

Single crystal LiHoF$_4$ was purchased from *Altechna* with the tracking number **#523201216**. The crystal had the shape of a rod of 6 mm diameter, with the c-axis pointing along the cylinder axis. For the AC susceptibility measurements a cubic sample was cut by a diamond wire saw,
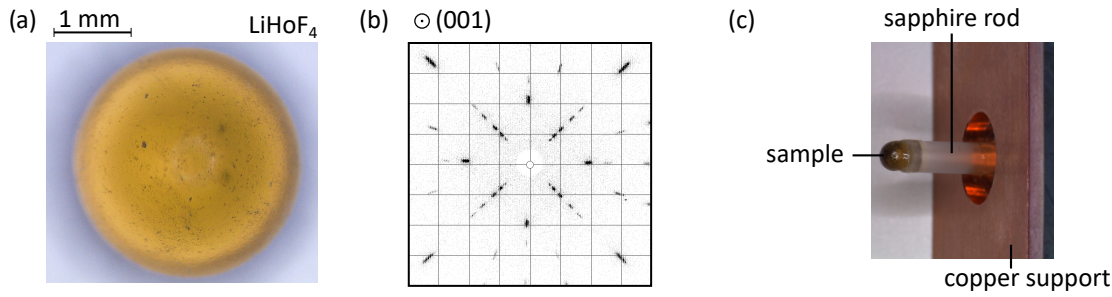

(a) 1 mm LiHoF$_4$ (b) ⊙ (001) (c) sapphire rod

sample

copper support

Figure 2.7.: Sample orientation and preparation of the LiHoF$_4$ crystal. (a) Photograph of the spherical LiHoF$_4$ sample, used throughout this thesis. (b) Picture of the Laue diffraction pattern of the sample, mounted onto the sample holder. The sample was oriented to point along a crystallographic ⟨001⟩ direction. (c) Photograph of the sample attached to the sample holder, consisting of a sapphire rod and a copper support.

and carefully ground and polished into a sphere of 2.8 mm diameter. A photograph of the sample is shown in figure 2.7 (a). The sample was oriented using Laue diffraction and attached to a sapphire rod using GE varnish. The corresponding scattering pattern is shown in figure 2.7 (b), where the crystallographic c-axis points perpendicular to the plane. The sapphire rod with the sample mounted was attached to a copper sample holder (cf. figure 2.7 (c)), which can be screwed onto the susceptometer, positioning the sample in the centre of one of the secondaries, as shown in section 1.2.1.

2.2.2. Evaluation of Measurement Uncertainties

For the low temperature studies, an Oxford Instruments JT-Kelvinox ^{3}He/^{4}He dilution refrigerator was used and adapted to the American Magnetic 2D vector magnet (AMI), as presented in section 1.2.5 (d) and (b), respectively. To fit the insert into the cryostat, it was necessary

to operate the mixing chamber with the susceptometer mounted directly onto the chamber in the high-field region of the vector magnet. As a consequence, sample and mixing chamber thermometer reading were subject to the presence of strong magnetic fields. This made a temperature correction of the thermometry necessary.
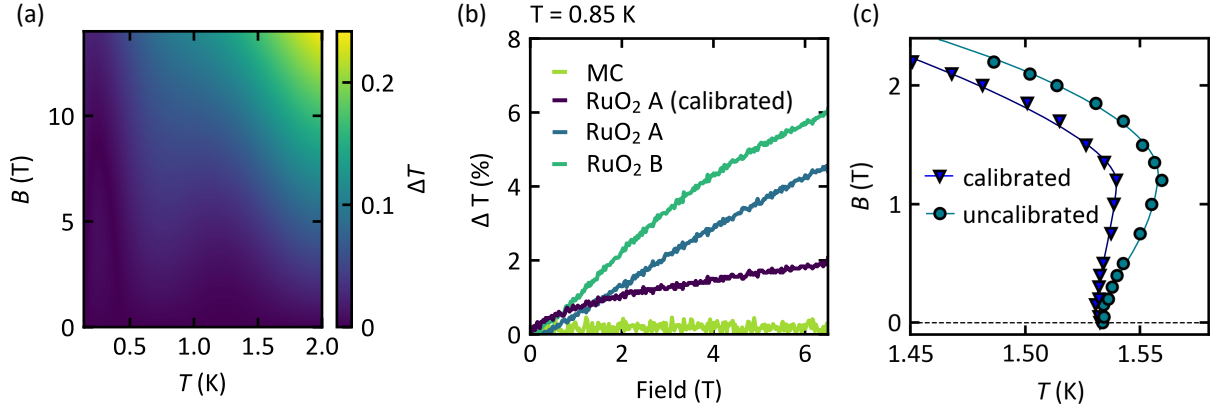

Figure 2.8.: Evaluation of systematic changes of the putatuive sample temperature due to the magnetoresistance of the sample thermometers. (a) 2D map of the temperature shift ΔT of the sample thermometer, caused by the magnetoresistance of the thermometers as a function of temperature T and magnetic field B. (b) Relative temperature deviation ΔT of all sample thermometers (RuO$_2$ A and B) as compared to the temperature of the mixing chamber (MC) as a function of an external magnetic field B. Calibration of one of the sensors allowed to reduce the deviation to below 2%. (c) Influence of the thermometer calibration on the exact phase boundaries, determined in this thesis.

Two calibrated RuO$_2$ temperature sensors were used, mounted close to the sample onto the susceptometer, to detect the sample temperature. The thermometers were purchased from *Lake Shore Cryotronics, Inc.* and from *K. Neumeier, WMI*, and are calibrated in zero magnetic field. Additionally, another calibrated RuO$_2$ sensor purchased from *Lake Shore Cryotronics, Inc.* was used to control the temperature of the mixing chamber in combination with a resistive heater. Unfortunately, all sensors show a non-vanishing magnetoresistance as a function of the applied magnetic field, causing systematic deviations in strong magnetic fields. According to *Lake Shore Cryotronics, Inc.*, this error remains below 5% for fields up to $5\,\mathrm{T}$. Nevertheless, to ensure a correct temperature reading especially when determining the critical temperature T_c, one of the thermometers was calibrated in magnetic fields up to $B = 14\,\mathrm{T}$. The calibration was carried out in the JT dilution refrigerator, however ,using a different magnet system, with a field-compensated region at the mixing chamber for a reliable reference temperature. Similar calibrations have been reported by the author in reference [26], where further details on the experimental configuration may be found. The thermometer was calibrated at temperatures between $T = 150\,\mathrm{mK}$ and $T = 4\,\mathrm{K}$ under magnetic fields between $B = 0\,\mathrm{T}$ and $B = 14\,\mathrm{T}$. Shown

in figure 2.8 (a) is the temperature offset, detected as a function of reference temperature and magnetic field.

Using the grid shown in figure 2.8, the temperature reading recorded during each measurements was corrected. For instance, shown in figure 2.8 (b) are the temperatures detected with both RuO$_2$ sensors at the sample positions (RuO$_2$ A and RuO$_2$ B), the mixing chamber temperature (MC) as well as the calibrated temperature reading of RuO$_2$ A as a function of the magnetic field at a constant control temperature of $T = 1.4\,\mathrm{K}$. The magnetoresistive effect of both sample thermometers generate an error of the temperature reading of up to 5%, consistent with the corresponding data sheets. Note that the corrected temperature still exhibits a small offset as compared to the temperature detected at the mixing chamber of approx. 1-2 %. This is attributed to the magnetoresistance of the control thermometer, which results in an effective change of the sample temperature during the sweep. Note, moreover, that the calibrated measurement represents the actual sample temperature and may thus be used as the correct sample temperature. The calibration turns out to be important for the magnetic phase boundaries of LiHoF$_4$. As shown in figure 2.8 (c), neglecting this effect results in a shifted phase boundary. This correction has therefore been applied to all data, presented in this chapter.

In the measurement configuration used in this thesis, the 2D vector field was generated by two Helmholtz pairs pointing along the horizontal x-axis and the vertical z-axis, respectively. Both fields were controlled by separate current sources and the angular resolution of the resulting vector field was limited by the resolution of each current source. Hence precision problems will only arise if one or both components of the vector field fall below the resolution limit of approximately $100\,\mu\mathrm{T}$. This is most likely the case for a magnetic field vector pointing very close to the x-axis or the z-axis, resulting in a vanishingly small component of the other respective field axis.

Figure 2.9 shows the recorded deviation from a magnetic field angle of $\varphi_\perp = 1.75°$, where the angle is defined as $\varphi = \arctan(\frac{B_x}{B_z})$, as a function of the absolute value of the external magnetic field B. $\varphi_\perp$ represents a perpendicular alignment of sample and magnetic field, as shown below in section 2.3.2, as used mostly throughout this thesis. For this angle, the deviation $\Delta\varphi = \varphi - \varphi_\perp$ remains below $\Delta\varphi = 0.001°$ for all magnetic fields above $B > 0.9\,\mathrm{T}$. For fields between $B = 0.1\,\mathrm{T}$ and $B = 0.9\,\mathrm{T}$ an upper limit of $\Delta\varphi = 0.01°$ is observed reaching up to $\Delta\varphi = 0.1°$ when approaching $B \approx 0$. For the measurements presented in this thesis, the deviation $\Delta\varphi$ for magnetic fields between $B = 4\,\mathrm{T}$ and $B = 6\,\mathrm{T}$ are relevant, as this is the critical field of the quantum phase transition in LiHoF$_4$. The deviation in this field range is well below $0.001°$ and the measurement uncertainty may be neglected safely. Note that for systems with very small transition fields and with high angular resolution, an initial angle $\varphi_\perp$ of $45°$ is best suited for most accurate orientation.
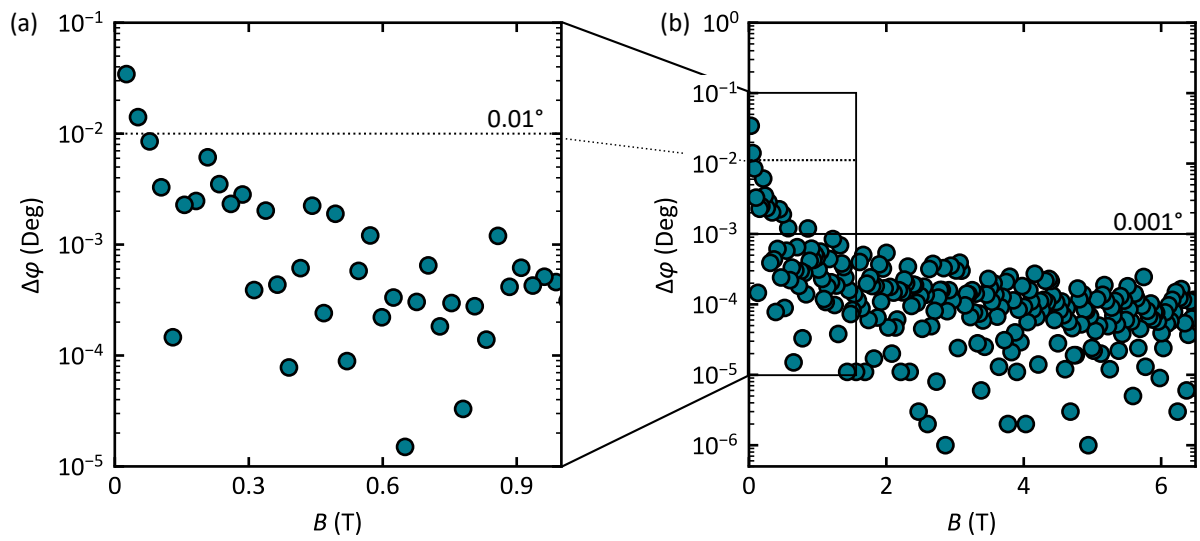
Figure 2.9.: Angular deviation $\Delta\varphi$ from an desired angle $\varphi = 1.75°$ of the vector magnet used throughout this thesis, as a function of the absolute value of the magnetic field B. (a) Close-up view of the low field regime. Deviations larger than $0.01°$ are restricted to magnetic fields $B < 0.2\,\mathrm{T}$. (b) Angular deviation for large magnetic fields. The precision is better than $\Delta\varphi \leq 0.001°$ for $B > 1\,\mathrm{T}$.

2.3. Experimental Results

In this section, measurements of the transverse magnetic AC susceptibility, $\chi_\perp$, in LiHoF$_4$ are presented. First, the magnetic phase diagram, inferred from magnetic field and temperature sweeps of the susceptibility, is shown. An overview of generic features of typical data is given and the transition temperature T_c and the transition field B_c are defined. Following that, the data are discussed in detail, starting with an evaluation of the dependence of $\chi_\perp$ on the relative orientation between applied magnetic field and the crystallographic orientation of the sample. Subsequently, our results are compared to measurements reported in the literature, confirming previous experimental findings such as the observation of mean-field critical exponents along the phase transition line down to lowest temperatures. Finally, two distinct features, which remained unappreciated in previous studies, are discussed. First, the influence of dynamical properties of the domain-walls on $\chi_\perp$, and second, an additional contribution to $\chi_\perp$, which may be attributed to a strong interaction between the applied magnetic field and the nuclear spin system.

2.3.1. Magnetic Phase Diagram of LiHoF$_4$

Shown in 2.10 are transverse susceptibility data of LiHoF$_4$ recorded as part of this thesis. Figure 2.10 (a) shows a 2D colorplot of the real part of the transverse susceptibility, Re $\chi_\perp$, as a function of the applied magnetic field B and the sample temperature T, while figures (c)-(f) depict typical magnetic field and temperature sweeps of Re $\chi_\perp$ and Im $\chi_\perp$ to illustrate the definition of the transition temperature T_c and the transition field B_c. Figure 2.10 (b) schematically depicts the geometric configuration of the measurement with the applied field, B, applied perpendicular to the crystallographic c-axis as well as to the oscillating excitation field B_{AC}. The measurements have been carried out at temperatures between $T = 69\,\mathrm{mK}$ and $T = 1.75\,\mathrm{K}$ as well as for magnetic fields ranging from $B = 0$ to $B = 6.5\,\mathrm{T}$. The same excitation amplitude, $B_{AC} = 0.16\,\mathrm{mT}$, and excitation frequency, $f_{AC} = 511\,\mathrm{Hz}$, were used for all measurements throughout this thesis, if not stated differently.

As a function of decreasing temperature, the real part of the transverse susceptibility, Re $\chi_\perp$, increases monotonically and reaches a plateau below the critical temperature value of $T_c \approx 1.53\,\mathrm{K}$ in zero field as shown in figures 2.10 (a) and (c). For larger magnetic fields, this value does not change significantly up to approximately $2\,\mathrm{T}$, above which the transition temperature is gradually suppressed as a function of increasing magnetic field. The transition temperatures T_c, indicated as blue diamonds in figure (a), have been extracted from temperature sweeps similar to the sweep shown in figure 2.10 (c), in which the transition temperature is indicated by a small blue triangle. No significant contribution to the imaginary part may be observed around this transition. Details of this phase boundary have been reported in references [9, 63, 73, 75] and the nature of this transition, in particular the detailed temperature dependence of the phase

boundary at small magnetic fields, will be presented in detail in section 2.3.3.

At the lowest temperatures, a quantum phase transition may be observed as a function of the applied magnetic field B, with a transition from a ferromagnetic into a paramagnetic state at $B_c \approx 5\,\mathrm{T}$. Shown in figure 2.10 (d) are typical magnetic field dependences of $\mathrm{Re}\,\chi_\perp$ and $\mathrm{Im}\,\chi_\perp$ at the lowest temperature accessible. Starting at high magnetic fields, $\mathrm{Re}\,\chi_\perp$ increases and reaches a plateau of approx 0.33 at the critical field $B_c \approx 5\,\mathrm{T}$, indicated by the blue triangle. This plateau of $\mathrm{Re}\,\chi_\perp$ is constant down to a magnetic field of approximately $B_\mathrm{d} = 2\,\mathrm{T}$, where a sudden decrease of $\mathrm{Re}\,\chi_\perp$ can be observed. This transition, indicated by a red triangle, is most
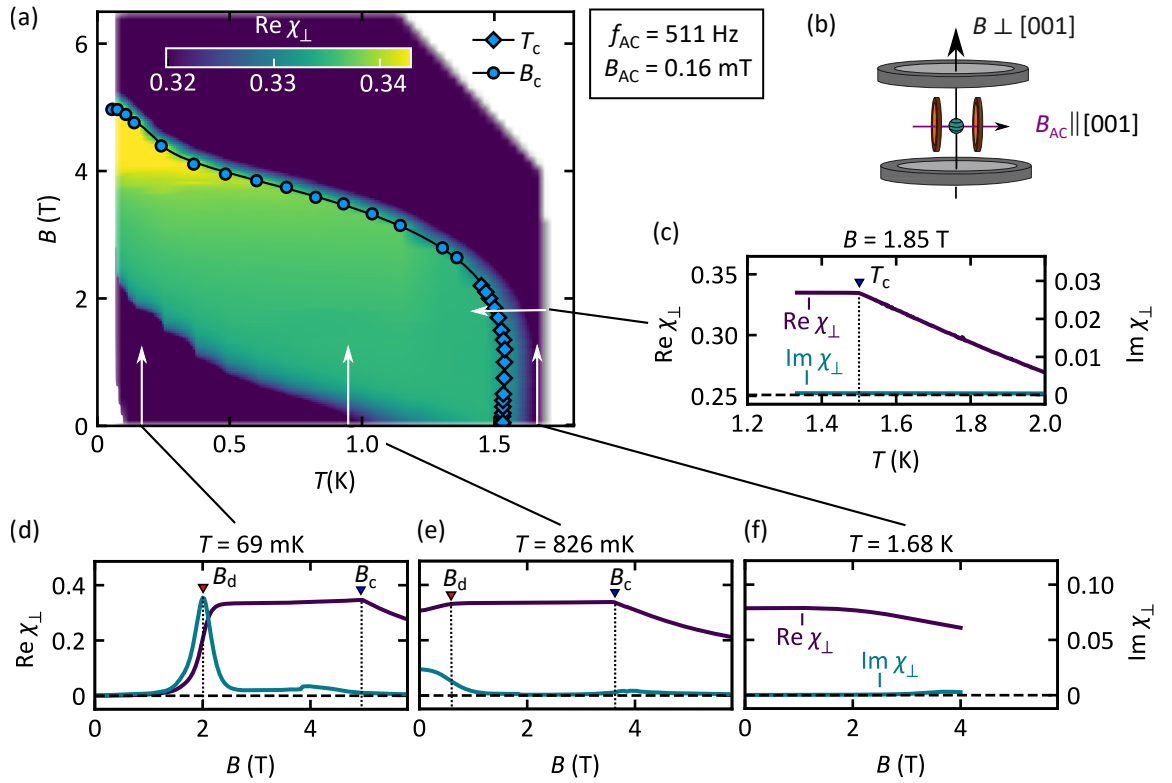

Figure 2.10.: Measurement of the transverse AC susceptibility $\chi_\perp$ of LiHoF$_4$. (a) $\chi_\perp$ as a function of temperature and transverse magnetic field. The data was recorded in magnetic field and temperature sweeps at an excitation frequency $f_\mathrm{AC} = 511\,\mathrm{Hz}$ and an excitation amplitude $B_\mathrm{AC} = 0.16\,\mathrm{mT}$, where circles and diamonds denote values inferred from field and temperature sweeps, respectively. (b) Schematic depiction of the field configuration used in the transverse susceptibility measurements. (c) Typical temperature sweep of real and imaginary parts of $\chi_\perp$. The blue triangle marks the transition temperature T_c. (d)-(f) Typical magnetic field sweeps of $\mathrm{Re}\,\chi_\perp$ and $\mathrm{Im}\,\chi_\perp$ at different temperatures. Blue triangles mark the transition to the ferromagnetic state at B_c; red triangles indicate a distinct transition at lower temperatures, B_d.

likely associated with domain-wall freezing, as comprehensively discussed in section 2.3.5. The transition is accompanied by a strong peak in $\operatorname{Im}\chi_\perp$, while $\operatorname{Im}\chi_\perp$ remains negligible everywhere, except for a small contribution around $B \approx 4\,\mathrm{T}$ of unidentified origin. Below B_d, $\operatorname{Re}\chi_\perp$ remains negligible down to zero magnetic field.

At higher temperatures, shown in figure 2.10 (e) for $T = 826\,\mathrm{mK}$, the generic shape of $\operatorname{Re}\chi_\perp$ is retained with the transition field B_c being shifted to smaller values. Significant differences may only be observed at small magnetic fields where B_d is strongly reduced, leading to a small decrease of $\operatorname{Re}\chi_\perp$ below B_d as compared to the low temperature data. Consistently, the strong contribution to $\operatorname{Im}\chi_\perp$ at B_d is shifted towards lower fields. The unidentified contribution at approximately $4\,\mathrm{T}$, however, persists independently from the value of B_c. At temperatures above T_c, depicted in figure 2.10 (f), as expected, no sharp transition is visible in $\operatorname{Re}\chi_\perp$. Only the contribution around $4\,\mathrm{T}$ appears to remain unchanged, which is discussed further in section 2.3.5. Finally, a small additional contribution to the plateau value of $\operatorname{Re}\chi_\perp$ can be observed as yellow shaded area around the critical field at very low temperatures in the colorplot of figure 2.10. Here, the strong hyperfine-coupling, which is known to exist in this compound, appears to contribute to the susceptibility as discussed in section 2.3.6.

2.3.2. Angular Dependence of the Transverse Susceptibility

One of the main challenges in the investigation of transverse field-tuned quantum phase transitions is the precise alignment of the crystallographic easy axis and the applied magnetic field. Unfortunately, fixing the mechanical orientation of the sample is rather challenging, especially for spherical samples. To correct the misalignment of the sample with respect to the support, we used a 2D vector magnet to generate the applied static field. In such a system, as discussed in section 1.1.2, two separate coils systems allow a rotation of the magnetic field within the x-z plane. With this, the precise perpendicular position between the applied magnetic field and the crystallographic easy axis may be determined by a study of the transverse susceptibility as a function of the changing field orientation, measured by the angle φ. As will be shown in the following section, the angle $\varphi_\perp$, accounting for the perpendicular orientation, may then be determined by evaluating the shape of the susceptibility, as well as the critical field.

Figure 2.11 (a) shows a schematic drawing of the field configuration and the angle definitions used throughout this chapter. The static magnetic field B is applied to the sample at a variable angle φ with respect to the vertical z-axis. The possible misalignment of the crystallographic [001] axis of the sample from the horizontal x-axis, $\varphi_\perp$, is unknown and has to be determined. The oscillating excitation field B_AC is applied along the horizontal x-axis. It is important to note that the misalignment between the excitation field B_AC of the susceptometer and the crystallographic [001] direction does not affect the experimental results significantly.
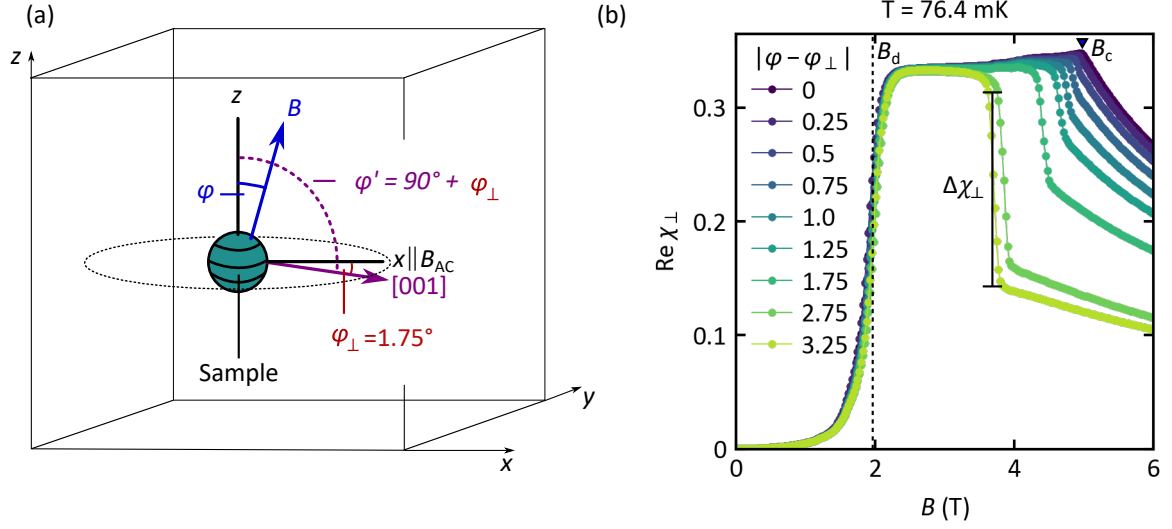
Figure 2.11.: Investigation of the quantum phase transition at low temperatures as a function of field orientation. (a) Schematic depiction of the field geometry during the measurements. The static magnetic field B is applied at a variable angle φ with respect to the vertical z-axis. The oscillating magnetic field B_{AC} is superposed along the horizontal x-axis. A small misalignment of the sample with respect to the horizontal x-axis determined in this paragraph, $\varphi_\perp \approx 1.75°$, may be compensated by a rotation of B in the x-z plane. (b) Field sweeps of the real part of $\chi_\perp$ at different angles φ between the static magnetic field B and the crystallographic c-axis, $|\varphi - \varphi_\perp|$, at $T = 76.4\,\mathrm{mK}$. The highest transition field B_c is observed in perpendicular orientation, $\varphi = \varphi_\perp$, and shifts towards smaller fields when $\varphi \neq \varphi_\perp$. B_{d} remains unaffected.

Figure 2.11 (b) shows the real part of the susceptibility, $\mathrm{Re}\,\chi_\perp$, as a function of the applied magnetic field B for different field orientations $|\varphi - \varphi_\perp|$. All data were taken at the lowest accessible temperature of $T = 76.4\,\mathrm{mK}$ to reduce thermal influences on the quantum phase transition. At $\varphi_\perp = 1.75°$, the easy-axis of the sample is aligned perpendicular to the magnetic field. The value of $\varphi_\perp$ is determined in the following. Starting at the highest measured angular deviation of $|\varphi - \varphi_\perp| = 3.25°$, $\mathrm{Re}\,\chi_\perp$ exhibits a clear step $\Delta\chi_\perp$ at a transition field B_c just below $B = 4\,\mathrm{T}$, at which the susceptibility suddenly increases to a plateau value of $\mathrm{Re}\,\chi_\perp \approx 0.33$. When the field is reduced, $\mathrm{Re}\,\chi_\perp$ remains constant before decreasing to zero at $B_{\mathrm{d}} \approx 2\,\mathrm{T}$. Note that this decrease, associated with a domain-wall freezing, does not show any angular dependence for the range of angles investigated in this study. In general, the angular dependence of this decrease over a broader range of angles might be helpful to unambiguously identify this phenomenon. By rotating the applied field, the angular deviation $|\varphi - \varphi_\perp|$ may be reduced and the jump of the susceptibility $\Delta\chi_\perp$ decreases strongly as a function of φ, until it vanishes completely for perfect perpendicular alignment $|\varphi - \varphi_\perp| = 0°$. Additionally, the transition field B_c varies strongly as a function of φ, as depicted in figure 2.12 (a). Assuming that the highest critical
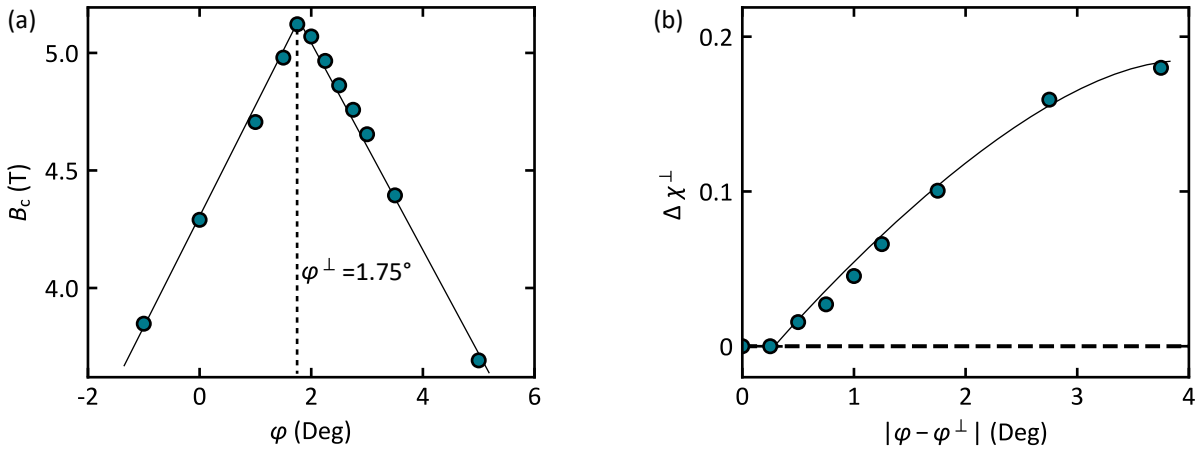
Figure 2.12.: Variation of the quantum phase transition in LiHoF$_4$ at low temperatures as a function of field orientation. (a) Variation of the transition field B_c as a function of the applied magnetic field angle φ, as defined in figure 2.11 (a). The highest transition field is observed for $\varphi = \varphi_\perp = 1.75°$, which represents a perpendicular alignment of applied magnetic field B and crystallographic easy axis. (c) Jump $\Delta\chi_\perp$ of the susceptibility at B_c as a function of the magnetic field deviation from the perpendicular orientation $|\varphi - \varphi^\perp|$. A jump is observed for field deviations $|\varphi - \varphi^\perp| > 0.25°$.

field value represents perfect perpendicular orientation, consistent with previous studies, we may extract the misalignment as $\varphi_\perp = 1.75°$. An evaluation of $\Delta\chi_\perp$ as a function of the angle of the applied magnetic field, φ, as depicted in figure 2.12 (b), reveals a monotonic decrease of $\Delta\chi_\perp$ approaching the perpendicular orientation before it vanishes completely below $|\varphi - \varphi_\perp| = \leq 0.25°$.

In summary, two distinct characteristics of $\mathrm{Re}\,\chi_\perp$ were determined which vary as a function of the angle between the crystallographic c-axis of the sample and the applied magnetic field. First, the critical field B_c, which decreases strongly for small misalignments and second, the shape of $\mathrm{Re}\,\chi_\perp$ around B_c, which exhibits a discontinuous jump under misalignments exceeding $0.25°$. The latter indicates that the nature of the transition might change as a function of the applied field angle and that the precise orientation is vital for the observation of a continuous quantum phase transition in a transverse magnetic field.

2.3.3. Comparison to Previous Studies

The most comprehensive study of the magnetic susceptibility of LiHoF so-far was reported over two decades ago by Bitko and co-workers [9, 75]. They investigated the detailed magnetic field and temperature dependence at the transverse field tuned QPT, establishing the well known magnetic phase diagram of LiHoF$_4$, shown in figure 2.4. As part of this thesis, these measurements were essentially repeated. It is therefore useful to compare the data collected within this

study with literature. In the following, the magnetic phase diagram, inferred from susceptibility measurements, as well as single magnetic field sweeps of the susceptibility, collected within this study are compared to the data set presented by Bitko in order to highlight similarities as well as discrepancies between both studies.
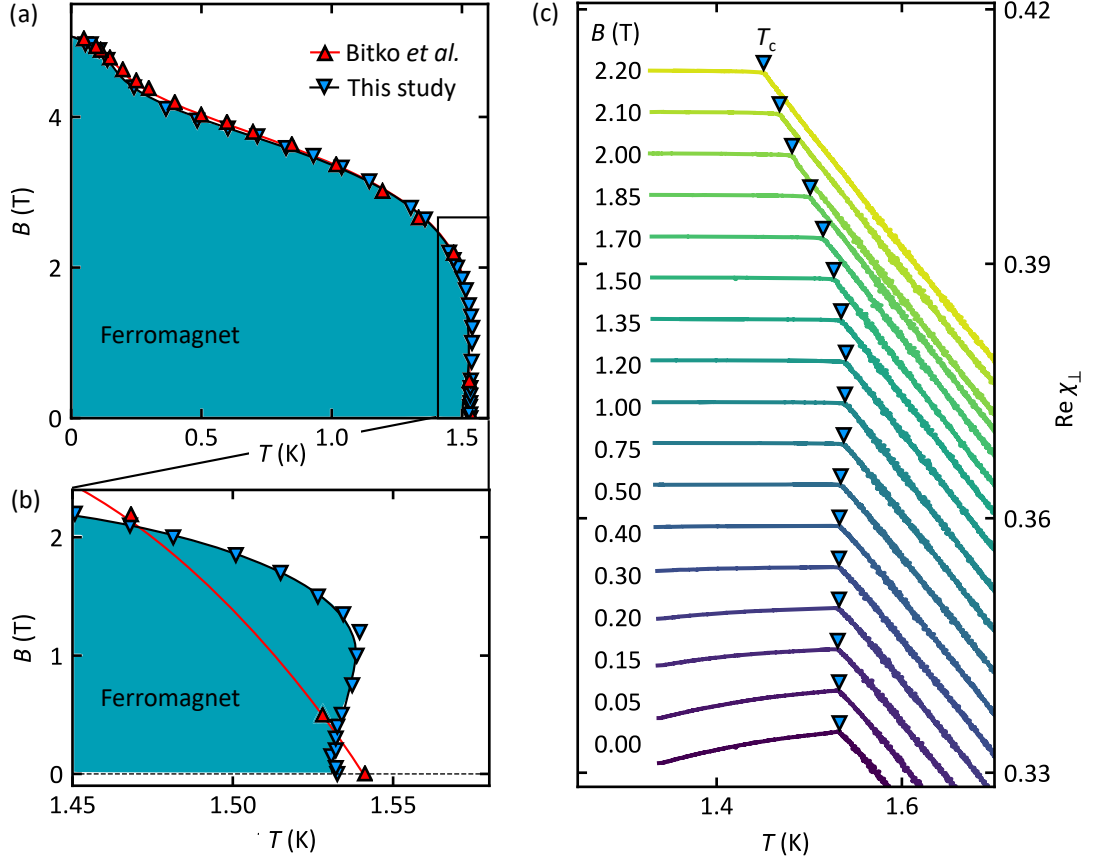

Figure 2.13.: Comparison of the magnetic phase diagrams reported by Bitko *et al.* [9] and this study. (a) Magnetic phase diagram of LiHoF$_4$ inferred from magnetic susceptibility measurements by Bitko *et al.* (red triangles) and this study (blue triangles). Lines are shown to guide the eye. Excellent agreement is observed over a wide range of the phase diagram. (b) Close-up view of the phase boundary around the critical temperature T_c at low magnetic fields. The enhanced data density of this study reveals an unconventional course of the phase boundary (green shaded area), which was not covered in previous studies (red triangles and line) (c) Typical susceptibility data recorded in temperature sweeps to define the phase boundary shown in (b). Blue triangles mark the transition temperatures T_c.

Figure 2.13 shows the phase boundaries of the magnetic phase diagram extracted from reference [9] (red triangles pointing up) as well as the boundaries extracted within this study (blue triangles pointing down). The green shaded area represents the ferromagnetic phase. Both data sets are in excellent agreement, showing a transition temperature of $T_c = 1.53\,\text{K}$ and a critical field

$B_c \approx 5$ T. As shown in the previous section, the critical field B_c in this compound is very sensitive to the magnetic field orientation, hence the similar values of B_c in both studies indicate a comparable sample orientation.

A detailed examination of the phase boundary close to the transition temperature, shown in figure 2.13 (b), reveals an unusual temperature dependence contrasting previous studies. Here, the transition temperature T_c increases at intermediate magnetic fields up to approximately 1.2 T, before it decreases for higher magnetic fields. Figure 2.13 (c) shows the corresponding temperature sweeps of the real part of the transverse susceptibility, from which the phase boundary has been extracted. The temperature dependence of the phase boundary is surprising, considering a classical mean-field model, which would yield the dashed line in figure 2.13 (b), in stark contrast to the phase boundary observed experimentally.
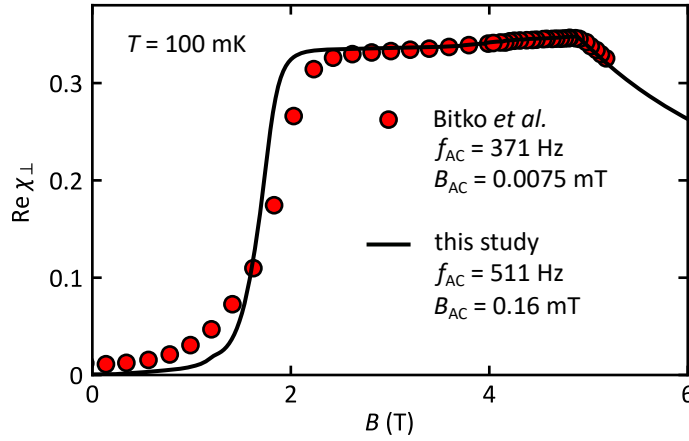

Figure 2.14.: Detailed comparison between two magnetic field sweeps from [75] and this study recorded at 100 mK. Both measurements were carried out at similar frequencies. The excitation field of the study by Bitko, $B_{AC} = 7.5\,\mu$T was considerably smaller than in this study. The data sets are in excellent qualitative and quantitative agreement. Note that the susceptibility extracted from [75] had to be scaled by a linear factor of 0.00145 to match our data, as no units are given in the work of Bitko *et al.*.

A comparison of the magnetic field dependence of $\chi_\perp$ with that presented by Bitko in reference [75] is shown in figure 2.14 for a temperature of $T = 100$ mK. The data reported by Bitko was collected using an excitation frequency of $f_{AC} = 371$ Hz and an excitation field of $B_{AC} = 7.5\,\mu$T. In comparison, in this study a similar excitation frequency of $f_{AC} = 511$ Hz was used, however with a significantly larger excitation amplitude of $B_{AC} = 0.16$ mT. Note that the data presented by Bitko was scaled by a factor of 0.00144 to fit our results in SI units. We find both curves to agree qualitatively and quantitatively for magnetic fields between $B = 3$ T and $B = 5$ T. The drop of the susceptibility around $B = 2$ T is also visible in both data sets, however, the

transition appears to be shifted slightly towards higher magnetic fields and to be broadened in the measurements of Bitko *et al.*.

In summary, the data reported by Bitko *et al.* are in excellent agreement with the data reported as part of this thesis, given the fact that different experimental set ups as well as different samples were used. The higher density of data points reported here proves to be important in the context of the incomplete theoretical account, which failed to explain the phase boundary. It is hoped that the detailed data presented in this study allows to reach better agreement. Additionally, Bitko and co-workers were not able to identify the origin of the decrease of the susceptibility at low magnetic fields and suggested a quantum glass state [75]. In section 2.3.5 an alternative explanation is offered, connected to complex domain-wall dynamics.

2.3.4. Evaluation of Critical Exponents

For the classification of the nature of the second order phase transition, the critical exponent γ as defined in section 2.1.1, was determined. Cooke and co-workers [62] report that the magnetic domain walls in the ordered state of $LiHoF_4$ and related Ising ferromagnets are completely free to move, leading to an infinite susceptibility in the ordered state which is reduced to a finite constant value by demagnetization effects. To extract the critical exponent γ we therefore follow reference [76] and define

$$\chi_\perp^{\mathrm{th}} = \frac{1}{(\chi_\perp)^{-1} - (\chi_\perp^{\mathrm{max}})^{-1}}, \tag{2.10}$$

which represents the expected signal of a sample with subtracted demagnetization contributions. Here, $\chi_\perp$ is the experimentally determined signal of the sample, and $\chi_\perp^{\mathrm{max}}$ the corresponding plateau of the recorded susceptibility $\chi_\perp$ at $B \leq B_c$.

Figure 2.15 (a) shows the corrected real part of the transverse susceptibility, Re $\chi_\perp^{th}$, as a function of the applied static magnetic field B at two different temperatures $T = 580\,\mathrm{mK}$ and $T = 57\,\mathrm{mK}$. The dashed lines mark the transitions fields $B_c = 4.95\,\mathrm{T}$ and $B_c = 3.87\,\mathrm{T}$, respectively. The value of $\chi_\perp(B = B_c)$ at the transition field B_c is used as $\chi_\perp^{\mathrm{max}}$ in the ordered phase in order to calculate $\chi_\perp^{th}$. Figure 2.11 (a) and figure 2.18 show that the susceptibility in the ordered phase is not constant down to zero magnetic field, as it may be expected based on theoretical considerations. Consequently, the determination of $\chi_\perp^{\mathrm{max}}$ is difficult and will lead to a systematic error of the critical exponent. A detailed evaluation of this uncertainty, however, shows that the influence of variations of $\chi_\perp^{\mathrm{max}}$ does not affect the critical exponent. The calculated value of $\chi_\perp^{\mathrm{th}}$ shows the expected critical behaviour of the susceptibility and the critical exponent γ may be extracted from our data set using an exponential fit

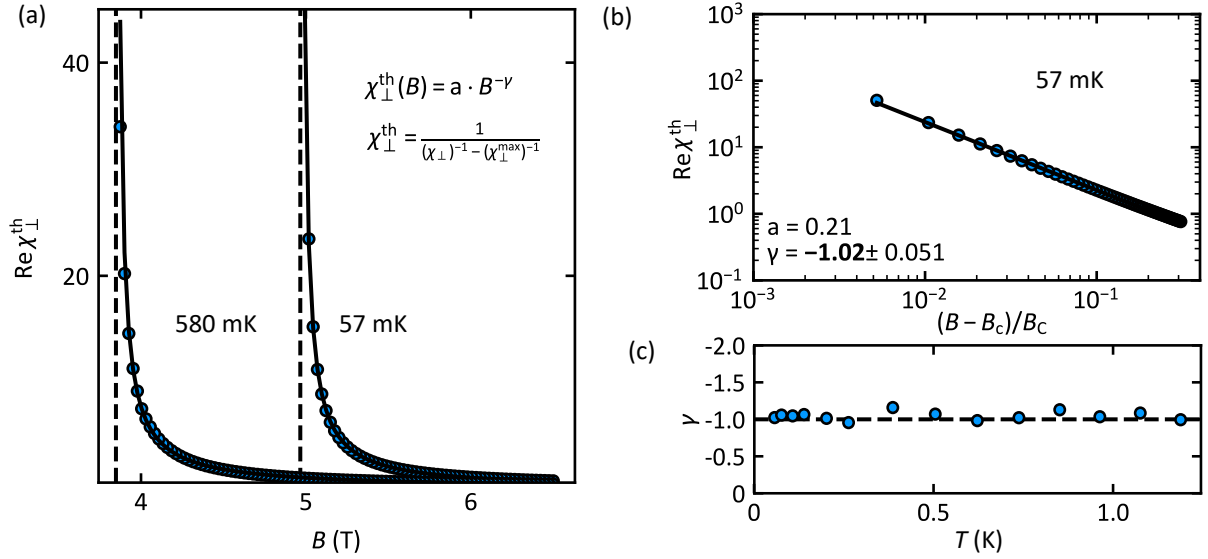$$\chi_\perp^{\mathrm{th}}(B) = a \cdot B^{-\gamma}. \tag{2.11}$$

Figure 2.15.: Evaluation of the critical exponent γ at B_c. (a) Transverse susceptibility $\chi_\perp^{th}$ as a function of the magnetic field B for two different temperatures. Both curves show an exponential divergence when approaching the critical field B_c, indicated by the dashed lines. The blue points are data points. The black line is an exponential fit to the data. (b) Data and exponential fit on a logarithmic scale for $T = 54\,\text{mK}$, the lowest temperature measured. (c) Critical exponents between $T = 54\,\text{mK}$ and $T = 1.2\,\text{K}$ as inferred from magnetic field sweeps. The exponent remains close to $\gamma = 1$, as expected for a continuous mean-field transition.

We find $\gamma = 1.02 \pm 0.002$ for $57\,\text{mK}$, the lowest temperature measured. The fit is shown on a logarithmic scale in figure 2.15 (b). Note that the statistical error of the fit is negligible compared to the uncertainty, stemming from the demagnetisation correction, as discussed in the last paragraph. Introducing biased values of $\chi_\perp^{max}$ and B_c artificially, we find that the main result is not affected by details of the demagnetization correction, and the error is expected to remain below $\Delta\gamma \lesssim 0.05$. Figure 2.15 (c) additionally shows the value of the critical exponent γ along the phase transition line for increasing temperatures. Within the error boundaries, the exponent is unchanged $\gamma \approx 1$ over the whole range of the phase diagram.

In summary, we find a critical exponent of $\gamma = 1.02 \pm 0.05$ at the magnetic quantum phase transition of LiHoF$_4$ at B_c. Following the transition line towards higher temperatures, the critical exponent as a function of the magnetic field remains constant within our error boundaries over the whole temperature range of the ferromagnetic phase. The critical region hereby extends to values of $b = |B - B_c|/B_c > 10^{-1}$, in agreement with theoretical predictions for a classical transition [76, 77]. Furthermore, our critical exponent is in perfect agreement with Bitko *et al.*, who reported a critical exponent of $\gamma = 1.07 \pm 0.11$ [9]. We conclude that the system re-

tains its mean-field character down to the lowest accessible temperature of $57\,\mathrm{mK}$. This agrees with the theoretical concept of quantum-classical mapping, in which a d-dimensional quantum Ising-system in a transverse field is associated with a classical $(d+1)$ Ising transition at finite temperature without applied field, yielding a mean-field behaviour in the case of LiHoF$_4$ [10, 67]. Furthermore, our study confirms the continuous nature of the quantum phase transition, as expected in the vicinity of a quantum critical point.

2.3.5. Ferromagnetic State at Low Temperatures and Small Magnetic Fields

In the following, a detailed study of the transverse susceptibility, $\chi_\perp$, in the ferromagnetic regime of LiHoF$_4$ as a function of magnetic field and temperature, depicted in figure 2.16, will be presented. This is complemented by an examination of the dependence of $\chi_\perp$ on changes of the excitation frequency f_{AC}, presented in figure 2.17. As our main result, we find a small pocket of reduced susceptibility at low temperatures and small magnetic fields within the ferromagnetic phase of LiHoF$_4$, which is discussed in detail at the end of this section.

Figure 2.16 shows an overview of magnetic field and temperature sweeps of the real and the imaginary parts of the transverse susceptibility, $\mathrm{Re}\,\chi_\perp$ and $\mathrm{Im}\,\chi_\perp$. All data were recorded at an excitation frequency and amplitude of $f_{\mathrm{AC}} = 511\,\mathrm{Hz}$ and $B_{\mathrm{AC}} = 0.16\,\mathrm{mT}$, respectively. Figures 2.16 (a) and (b) show a set of selected magnetic field sweeps of $\mathrm{Re}\,\chi_\perp$ and $\mathrm{Im}\,\chi_\perp$, at different temperatures between $T = 69\,\mathrm{mK}$ and $T = 1.57\,\mathrm{K}$, and at a field rate of $\frac{\mathrm{d}B}{\mathrm{d}t} = -2\,\frac{\mathrm{mT}}{\mathrm{s}}$. Figures 2.16 (c) and (d) show the temperature dependence of $\mathrm{Re}\,\chi_\perp$ and $\mathrm{Im}\,\chi_\perp$ recorded at a sweep rate of $\frac{\mathrm{d}T}{\mathrm{d}t} = -5\,\frac{\mathrm{mK}}{\mathrm{s}}$ at static magnetic field values of $B = 0$, $1\,\mathrm{T}$ and $2\,\mathrm{T}$. Finally, figure 2.16 (e) shows a colorplot of $\mathrm{Im}\,\chi_\perp$ as a function of the magnetic field and temperature, complementing figure 2.10 (a), where the corresponding real part has been presented.

As shown in figure 2.16 (a), data recorded at the highest temperature of $T = 1.57\,\mathrm{K}$, i.e. above the critical temperature T_c, shows a featureless increase of the susceptibility towards small fields. At $T = 1.36\,\mathrm{K}$, just below T_c, $\mathrm{Re}\,\chi_\perp$ exhibits a kink at the critical field B_c, marked by the blue triangle. Here, the system transits from a field-polarised state at $B > B_c$ into the ferromagnetic phase at $B \leq B_c$. The value of the susceptibility at the plateau below B_c remains constant down to zero magnetic field. With decreasing temperature, the transition field B_c shifts to higher fields, consistent with our discussion above. At low magnetic fields, where the susceptibility is expected to remain constant down to zero magnetic field, the susceptibility shows a distinct decrease at magnetic fields below $B < 0.5\,\mathrm{T}$ for $T \leq 1\,\mathrm{K}$. This reduction becomes more pronounced for decreasing temperatures until the susceptibility vanishes completely below approximately $T = 150\,\mathrm{mK}$ and magnetic fields below $B \approx 1.8\,\mathrm{T}$, i.e. the onset of the reduced susceptibility shifts towards higher magnetic fields with decreasing temperature.
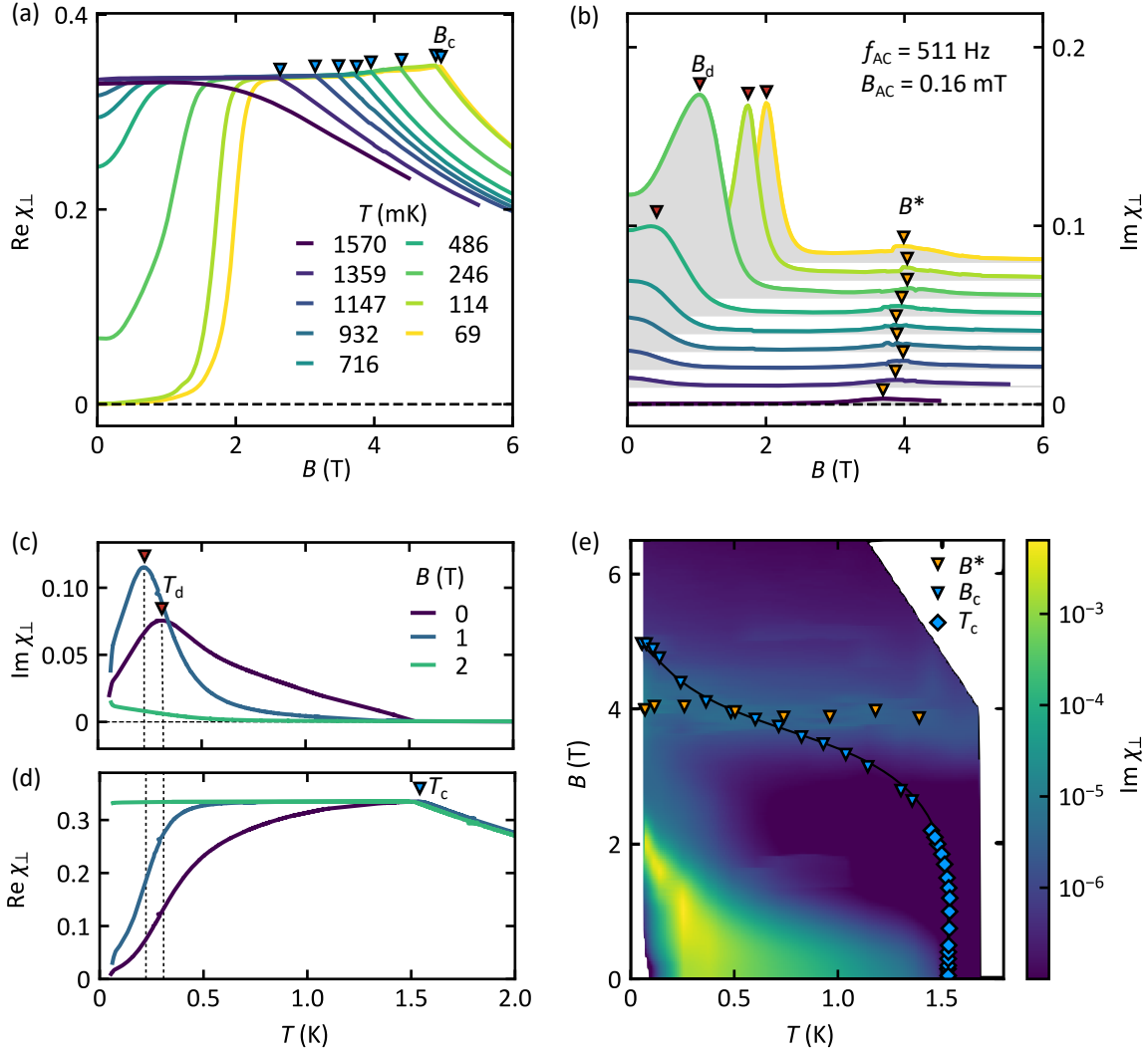
Figure 2.16.: Overview of measurements of the transverse susceptibility, $\chi_\perp$, as a function of temperature and magnetic field. (a) Magnetic field sweeps of the real part of the transverse susceptibility, $\mathrm{Re}\,\chi_\perp$, as a function of the external magnetic field B for temperatures between $T = 1.57\,\mathrm{K}$ and $T = 69\,\mathrm{mK}$. $\mathrm{Re}\,\chi_\perp$ shows a distinct drop at small magnetic fields. (b) Imaginary part of the transverse susceptibility, $\mathrm{Im}\,\chi_\perp$, at different temperatures. Yellow triangles mark an additional contribution to $\mathrm{Im}\,\chi_\perp$, B^*, of unknown origin. Red triangles mark the field, below which the domain-wall mobility is reduced, B_d. (c),(d) $\mathrm{Re}\,\chi_\perp$ and $\mathrm{Im}\,\chi_\perp$ as a function of temperature for selected magnetic field values. Dashed lines mark the peak positions in $\mathrm{Im}\,\chi_\perp$, T_d, associate with the freezing of domain-walls. (e) 2D grid of $\mathrm{Re}\,\chi_\perp$ as a function of the static magnetic field B and temperature T. Yellow triangles indicate the position of the peaks, extracted from (b). Blue triangles and diamonds indicate the phase transition line between ferromagnetic and paramagnetic state, extracted from magnetic field and temperature sweeps, respectively.

Figure 2.16 (b) shows the corresponding imaginary part, Im $\chi_\perp$, which exhibits a small contribution at $B^* \approx 4\,\mathrm{T}$, indicated by the yellow triangles, as well as a strong peak-like contribution at small magnetic fields. The contribution around $4\,\mathrm{T}$ exhibits a shallow maximum centred around $4\,\mathrm{T}$ for all temperatures investigated in this study. This contribution cannot be associated with any feature in the real part Re $\chi_\perp$ and the origin remains unclear. Possible scenarios include a parasitic contribution from the susceptometer, which may most likely be ruled out by detailed background measurements, or a small contribution associated with the possible existence of a quantum critical point at $B \approx 4\,\mathrm{T}$.

The strong peak at small magnetic fields, may be clearly associated with the decrease of Re $\chi_\perp$, observed in figure 2.16 (a). In contrast to the real part Re $\chi_\perp$, a small contribution to Im $\chi_\perp$ may already be observed at the highest temperature of $T = 1.36\,\mathrm{K}$ in the ferromagnetic phase, where Re $\chi_\perp$ does not show a visible signature yet. When reducing the temperature, the peak is strongly enhanced and shifted towards higher magnetic fields consistent with the observations in the real part. Additionally, the shape of the contribution changes from a small, broad peak at high temperatures to a large and sharp peak at the lowest temperatures studies.

A similar behaviour may be observed in the temperature dependence of Re $\chi_\perp$ and Im $\chi_\perp$, shown in figures 2.16 (c) and (d). Here, Im $\chi_\perp$ displays an analogous contribution at small temperatures for $B = 0$ and $B = 1\,\mathrm{T}$. For $B = 2\,\mathrm{T}$, a clear peak as a function of temperature is seen as well as a small increase at very low temperatures. Again, the contribution in the imaginary part is accompanied by a simultaneous decrease of the real part, Re $\chi_\perp$, as shown in figure 2.16 (d). The point of inflection of the decrease in Re $\chi_\perp$ can be associated with the peak in Im $\chi_\perp$, as indicated by the dashed vertical lines. Figures 2.16 (b) and (c) are summarised in a colorplot in figure 2.16 (e), where the magnetic field sweeps are combined to generate a 2D grid of Im $\chi_\perp$. This emphasises first, the feature at small magnetic fields $B \leq 2.5\,\mathrm{T}$, which extends to higher temperatures for smaller magnetic fields (yellow region) and second, the tiny contribution at $B^* \approx 4\,\mathrm{T}$, which is present over the whole range of temperatures as indicated by the yellow triangles. The phase boundaries of the ferromagnetic phase, as extracted from Re $\chi_\perp$, are depicted as blue triangles and diamonds.

To characterise the nature of the distinct behaviour of $\chi_\perp$ at low temperatures and small magnetic fields further, a study of the frequency dependence of this feature was carried out. Therefore, similar measurements as presented in the previous paragraphs have been performed at a temperature $T = 139\,\mathrm{mK}$, using various different excitation frequencies between $f_{\mathrm{AC}} = 10\,\mathrm{Hz}$ and $5011\,\mathrm{Hz}$. Figure 2.17 (a) shows magnetic field sweeps of Re $\chi_\perp$ for different excitation frequencies. In the high field region, $B > B_c$, all curves display the same field dependence. Note that a small offset that may be attributed to the generation of eddy currents in the susceptometer has been subtracted. At $B_{\mathrm{d}} \approx 2\,\mathrm{T}$, the data recorded at the highest excitation frequency
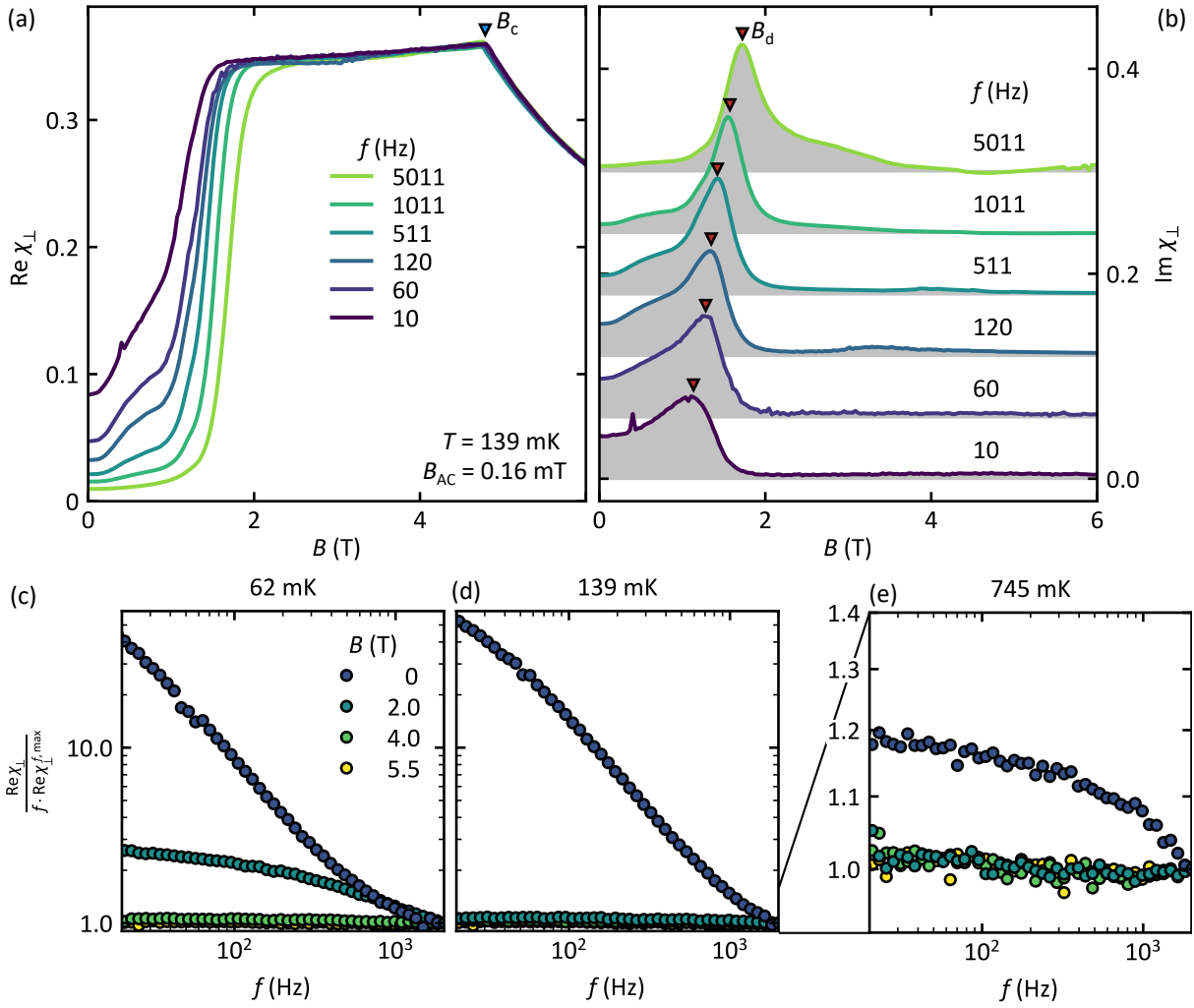
Figure 2.17.: Frequency dependence of the real and imaginary parts of the susceptibility in the low temperature region. (a) Re $\chi_\perp$ as a function of the magnetic field at $T = 139\,\text{mK}$ for excitation frequencies between $f_{\text{AC}} = 10\,\text{Hz}$ and $5011\,\text{Hz}$ (b) Im $\chi_\perp$ as a function of the magnetic field at $T = 139\,\text{mK}$ for various frequencies. Im $\chi_\perp$ shows a strong peak-shaped contribution at low magnetic fields for all measured frequencies, indicated by red triangles. (c) - (e) Detailed evaluation of the frequency dependence of Re $\chi_\perp$ at $T = 62\,\text{mK}$, $139\,\text{mK}$ and $745\,\text{mK}$, respectively. Re $\chi_\perp$ is normalized to the excitation frequency f_{AC} and the value of the susceptibility for the highest measured frequency, Re $\chi_\perp^{f,\,\text{max}}$. For classical ferromagnets a constant value of 1 is expected. Deviations from 1 indicate unusual physical behaviour.

starts to decrease sharply. By reducing the excitation frequency, B_{d} can be shifted towards lower magnetic fields. Additionally, the size of the drop is reduced for smaller frequencies, with the susceptibility saturating at a finite value for $B = 0$. For all frequencies below $f_{\text{AC}} = 5011\,\text{Hz}$, a small additional shoulder around $1\,\text{T}$ emerges. This contribution is most prominent for frequen-

cies around $f_{AC} \approx 511\,\mathrm{Hz}$. However, it is clearly visible for all frequencies down to $f_{AC} = 10\,\mathrm{Hz}$, the lowest frequency measured. The origin of this contribution could not be identified.

The corresponding imaginary part, $\mathrm{Im}\,\chi_\perp$, is shown in figure 2.17 (b). For better visibility, the data were shifted by 0.06 with respect to each other. In the high field region, no contribution to $\mathrm{Im}\,\chi_\perp$ is observed at all frequencies, while a broad peak may be observed in the low field region, consistent with the presentation above. The shape of this peak, as well as its position change as a function of excitation frequency. Starting at the lowest frequency, the peak is centred around $B_d \approx 1\,\mathrm{T}$ and exhibits a strongly asymmetric field dependence, with an extended wing towards zero magnetic field. When increasing the frequency, the peak shifts towards larger magnetic fields. The asymmetric contribution towards lower magnetic fields persists up to $f_{AC} = 1011\,\mathrm{Hz}$. At $f_{AC} = 5011\,\mathrm{Hz}$, the highest frequency measured, the contribution on the low field side of the peak vanishes and an additional shoulder on the high field side appears, which is not present in all other measurements.

Figures 2.17 (c) - (e) display the frequency dependence of $\mathrm{Re}\,\chi_\perp$ in further detail for three different temperatures and four different magnetic fields. Here, the value of $\mathrm{Re}\,\chi_\perp$ is normalised to the excitation frequency f_{AC} and the maximum value of the real part of the susceptibility at the highest measured frequency, $\mathrm{Re}\,\chi_\perp^{\mathrm{f,\,max}}$. The resulting normalised susceptibility, $\chi_\perp^{\mathrm{norm}} = \frac{\mathrm{Re}\,\chi_\perp}{f \cdot \mathrm{Re}\,\chi_\perp^{\mathrm{f,\,max}}}$, is shown as a function of the excitation frequency f_{AC}. For a conventional ferromagnet, this value is expected to remain constant, $\chi_\perp^{\mathrm{norm}} = 1$, for all frequencies. For the measurements presented in figure 2.17 (c), recorded at a temperature of $62\,\mathrm{mK}$, we observe such a behaviour above $B > 2\,\mathrm{T}$. At magnetic fields $B \leq 2\,\mathrm{T}$, the normalised susceptibility $\chi_\perp^{\mathrm{norm}}$ increases exponentially as a function of decreasing excitation frequency. Within the range of our measurements, $\chi_\perp^{\mathrm{norm}}$ appears to increase beyond the lowest accessible frequencies. Nevertheless, the shape of the curve suggests a maximum well below a frequency of $f_{AC} \ll 10\,\mathrm{Hz}$. At $T = 139\,\mathrm{mK}$, shown in figure 2.17 (d), similar behaviour may be observed, however restricted to zero magnetic field, while data at $B = 2\,\mathrm{T}$ remain constant over the whole range of frequencies. Finally, at the highest temperature of $T = 745\,\mathrm{mK}$, the deviation of the zero field measurement remains present, however, strongly reduced as compared to the low temperature measurements.

The detailed investigation of $\chi_\perp$ in the ferromagnetic regime of LiHoF$_4$ revealed a particular region in the phase diagram at small magnetic fields and low temperatures, in which our measurements deviate from the classical picture of an Ising ferromagnet. In the ordered phase of a conventional Ising-type ferromagnet, the domain-walls are free to move under an applied magnetic field. This allows to maintain an internal field equal to zero [62, 76], leading to a diverging susceptibility over the whole ferromagnetic regime. Finite demagnetization effects, in turn, prevent the experimentally observed susceptibility from showing such a divergence and lead to a plateau of constant susceptibility in the ordered phase, as reported in previous studies

consistent with our data [9, 62, 76]. However, in contrast to this simple theoretical picture, we find that the susceptibility gradually decreases with decreasing temperature, until Re $\chi_\perp$ vanishes at very low temperatures. We attribute this behaviour to a reduction of the domain-wall mobility due to the lack of thermal fluctuations at low temperatures. This interpretation is supported by the strong peak in the imaginary part Im $\chi_\perp$, presented in figures 2.16 (b), (c), and (e), suggesting strong dissipative effects at low temperatures, as well as by the distinct frequency dependence of this regime, presented in figure 2.17.

Surprisingly, the finite value of the susceptibility is recovered even at the lowest temperatures under a transverse magnetic field, above a critical field value $B_\mathrm{d} \approx 2.5\,\mathrm{T}$. In analogy to a study of Brooke *et al.* [78] on the isostructural doped compound LiHo$_{1-x}$Y$_x$F$_4$, with $x = 0.56$, we propose that the recovery of Re $\chi_\perp$ for $B > B*$ is caused by quantum fluctuations which facilitate a tunnelling of the domain-walls. Again, the strong frequency dependence of the susceptibility observed in the low temperature regime as a function of the applied field supports this suggestion. It is intuitive that the position of the domain walls are frozen-in at high excitation frequencies, while they are able to follow the applied field at low frequencies, leading to a smaller region of reduced susceptibility for small excitation frequencies f_AC and to an increase of the region for high frequencies, as depicted in figure 2.17. Several studies [71, 73] suggested that such complex domain-wall behaviour may play an important role in the description of the quantum critical point, as well as the classical phase boundaries in this compound. In this thesis, a first detailed experimental study of the properties of the ferromagnetic state in LiHioF$_4$ was presented providing an ideal starting point for further theoretical investigations of the microscopic picture of this compound.

2.3.6. Hyperfine Contribution to the Transverse Susceptibility

The phase boundary at the quantum phase transition between ferromagnetic and paramagnetic phase in LiHoF$_4$ is distinctly shifted towards higher magnetic fields at low temperatures, exceeding the values obtained by a straight-forward mean-field calculation (cf. figure 2.4). Bitko and co-workers concluded that strong hyperfine interactions may cause this unexpected upturn of the critical field at low temperatures, reproducing the experimentally determined phase boundary in this regime by including hyperfine interactions [9]. This was followed by Rønnow *et al.* [71] who argued that the incomplete mode softening, observed in their neutron scattering experiments, is caused by hyperfine interactions. The resulting mixture of nuclear and electronic spin contributions then leads to a stabilization of the magnetic order at higher magnetic fields. Even though both experiments underline the importance of hyperfine contributions for the magnetic properties of this compound, previous studies failed to observe any signature of this coupling in susceptibility measurements. In the following, we present detailed measurements of the transverse susceptibility in the ordered phase of LiHoF$_4$ which show an additional contribution, that

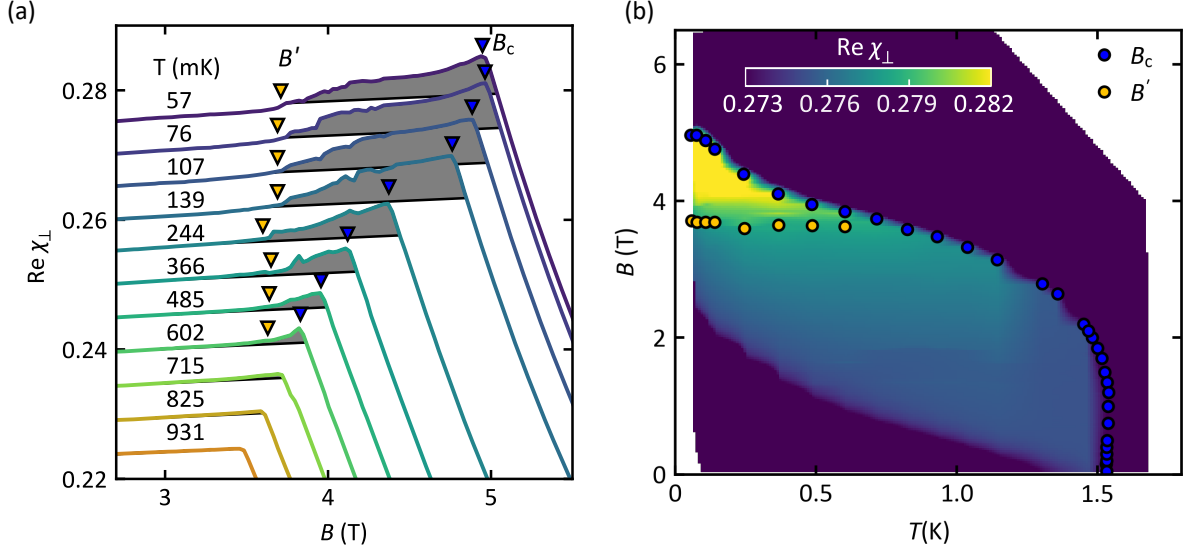may be attributed to the hyperfine interactions in $LiHoF_4$.

Figure 2.18.: Emergence of an additional contribution to $\chi_\perp$ in the vicinity of the quantum phase transition at B_c. (a) Close-up view of magnetic field sweeps of $\mathrm{Re}\,\chi_\perp$ for temperatures between $T = 57\,\mathrm{mK}$ and $T = 931\,\mathrm{mK}$. Yellow triangles mark the onset of the shaded area at B_c', indicating the additional contribution to $\mathrm{Re}\,\chi_\perp$. Blue triangles mark the transition field B_c. (b) 2D colorplot of $\mathrm{Re}\,\chi_\perp$ as a function of external magnetic field B and temperature T. An additional contribution to $\mathrm{Re}\,\chi_\perp$ emerges, visible as a yellow shaded area of increased $\mathrm{Re}\,\chi_\perp$. Yellow circles correspond to the field values B_c', marked by a yellow triangle in panel (a). The blue circles indicate the phase transition line at B_c.

Figure 2.18 summarises measurements of the real part of the transverse susceptibility, $\mathrm{Re}\,\chi_\perp$, as a function of magnetic field and temperature. Figure 2.18 (a) shows a close-up view of $\mathrm{Re}\,\chi_\perp$ close to the quantum phase transition at B_c, recorded at an excitation frequency $f_{\mathrm{AC}} = 511\,\mathrm{Hz}$ and an excitation amplitude $B_{\mathrm{AC}} = 0.16\,\mathrm{mT}$. For clarity of presentation, an offset has been added to the data. The sweeps shown here were recorded at temperatures between $T = 57\,\mathrm{mK}$ and $T = 931\,\mathrm{mK}$. Data are shown for applied static magnetic fields between $B = 2.8\,\mathrm{T}$ and $B = 5\,\mathrm{T}$. The complete data set without offset was shown and discussed above (cf. figure 2.16 (a)). The grey shaded area indicates an additional contribution to $\mathrm{Re}\,\chi_\perp$, which exceeds $\mathrm{Re}\,\chi_\perp$ as limited purely by demagnetisation effects. The onset of this contribution on the low-field limit is indicated by yellow triangles and will be refereed to as B' in the following . For the highest temperature of $T = 932\,\mathrm{mK}$ shown here, no additional contribution is observed and $\mathrm{Re}\,\chi_\perp$ exhibits the expected constant value below B_c. By reducing the temperature, the transition field shifts towards higher magnetic fields. For temperatures below $T \approx 700\,\mathrm{mK}$, the additional contribution to $\mathrm{Re}\,\chi_\perp$ can be observed between $B' \approx 3.7\,\mathrm{T}$ and B_c. By reducing the temperature further, the additional contribution increases in size and magnitude and the

transition field B_c is shifted towards higher magnetic fields. The onset of the contribution, however, appears to be independent of temperature and appears unchanged for fields exceeding $B' \approx 3.7$ T. Figure 2.18 (b) shows $\text{Re}\,\chi_\perp$ as a function of the magnetic field and temperature. The additional contribution is highlighted by color-coding of the susceptibility in a 2D grid, where the largest value (yellow) emerges above $B' \approx 3.7$ T and below B_c for temperatures below $T \approx 700$ mK. The constant value of $\text{Re}\,\chi_\perp$ can be observed in the rest of the ordered region, except for the low temperature and low field regime, which has been discussed separately in the previous section.

In summary, an additional contribution to the transverse susceptibility of LiHoF$_4$ was observed that may be attributed empirically to the nuclear spin system around the critical field B_c at low temperatures. This contribution may only be observed at an external transverse magnetic field exceeding $B' \approx 3.7\,T$ in good agreement with previous studies of the hyperfine coupling in this system. These measurements provide direct access to the coupling between the nuclear and the electronic spin system in LiHoF$_4$, representing key information for the interpretation of the magnetic properties and the quantum phase transition in this material.

2.4. Summary & Outlook

In this chapter, the low temperature properties of the dipolar-coupled Ising-magnet $LiHoF_4$, representing a model system for a magnetic quantum phase transition, were investigated. Therefore, transverse susceptibility measurements have been performed as a function of a magnetic field, applied perpendicular to the magnetic easy-axis, mediating the quantum phase transition. Our results were presented in two steps. First, properties of the magnetic quantum phase transition and the thermal phase transition were discussed. Then, details of the ferromagnetic state at low temperatures were investigated.

After an overview of the data collected, the first part of this chapter started with an account for small angular variations of the applied magnetic field with respect to the magnetic easy axis. We find that the nature of the QPT changes abruptly for angular displacements above approximately 0.25° from the perpendicular orientation, as identified by a distinct jump of the transverse susceptibility. A careful orientation of the sample with respect to the applied magnetic field, hence, proves to be essential for a successful investigation of the magnetic QPT. Subsequently, a detailed study of the phase boundaries of the ferromagnetic state was presented and the results were compared to previous studies. We find excellent agreement with the results from literature, however, an increased data point density in this study revealed significant discrepancies to the published mean-field behaviour around T_c. This might suggest a so-far incomplete theoretical picture of the microscopic details of this system, as proposed by Tabei *et al.* [73]. Nevertheless, an investigation of the critical exponents around B_c as a function of applied magnetic field at different temperatures yields, consistent with previous work, $\gamma \approx 1$, which agrees with the predicted mean-field behaviour as expected from quantum-classical mapping.

In the second part of this chapter, properties of the ferromagnetic state were investigated and three distinct regions within the ferromagnetic regime could be identified. First, a classical region at small magnetic fields and temperatures just below T_c, in which the ordered state is dominated by the formation of long needle-shaped domains. In this regime, highly mobile domain-walls are able to compensate any applied magnetic field, leading to a diverging susceptibility within the entire ferromagnetic phase. This divergence, however, is reduced to a finite susceptibility value by demagnetization effects, as observed over a broad range of the phase diagram in this study. Second, at lower temperatures, a significant decrease of transverse susceptibility is observed, which is most likely a result of reduced domain-wall mobility due to the decreasing energy of thermal excitations in this regime. The susceptibility vanishes in the limiting case of very low temperatures, suggesting a frozen state with no remaining domain-wall mobility. This interpretation is supported by a detailed investigation of the dependence of $\chi_\perp$ on the excitation frequency f_{AC}, which shows an enhanced region of reduced susceptibility for high excitation frequencies and a reduced region for small frequencies. Interestingly, the application

of a transverse magnetic field at low temperatures leads to a recovery of the previously observed plateau value, suggesting free domain-wall motion at magnetic fields larger than $B_d \approx 2\,\text{T}$. Due to the lack of thermal energy, we suspect that this effect is mediated by the transverse magnetic field which allows for quantum fluctuations, facilitating quantum tunnelling of the domain-walls even at zero temperature. Similar observations have been reported previously in a study of the isostructural doped compound LiHo$_{1-x}$Y$_x$F$_4$, with $x = 0.56$ [78]. Third, an additional contribution to $\chi_\perp$ was observed within the ferromagnetic phase at temperatures below $T < 700\,\text{mK}$ and for magnetic fields between $B' \approx 3.7\,\text{T}$ and B_c. This contribution might be a signature of the strong hyperfine coupling, which is believed to stabilise the magnetic order in this regime.

Even though LiHoF$_4$ is regarded as a textbook example for a transverse field-tuned quantum phase transition, various discrepancies between theoretical predictions and experimental observations remain an open topic in current research and demand further studies of this compound. In this thesis, we have addressed several of these issues, providing comprehensive experimental data of the low temperature regime of this compound. Based on our observations, we suggest a refinement of the present microscopical description of the ferromagnetic state in this compound, taking into account the precise course of the phase boundary around T_c, as determined in this study. Additionally, we suggest to revisit inelastic neutron scattering experiments at lowest temperatures possible, taking into account the importance of the orientation of applied field and crystallographic orientation determined above, to further investigate the nature of the quantum phase transition and possible influences of the hyperfine-coupling on the magnetic order. Furthermore, we propose to continue the study of the transverse susceptibility as presented here, to investigate the dependence of the hyperfine-contribution as a function of field rotation, which may be complemented by an investigation of all three magnetisation components in the same field configurations.

CHAPTER 3

Spin-Transfer Torques in the Skyrmion Lattice of MnSi

In this chapter, spin-transfer torques in the skyrmion lattice phase of the chiral magnet MnSi are investigated using transverse susceptibility measurements. As our main result, we find that the threshold current density above which spin-transfer torque effects are observed, may be reduced below an extremely low value $j_c \leq 0.14\,\mathrm{MAm}^{-2}$ by the application of an oscillating magnetic field. As a point of reference, a detailed investigation of the transverse susceptibility as a function of excitation frequency and amplitude was performed without current applied. Next, under applied DC current, we find that the oscillating magnetic field favours an unpinning of the skyrmion lattice, reducing the critical current density. Our results are in excellent agreement with complementary studies using time-resolved small-angle neutron experiments (TISANE).

The chapter is organised as follows. First, an introduction to cubic helimagnets and to the topological properties of MnSi is given, motivating the key questions addressed in this thesis. This is followed by an overview of related experimental work, particularly focusing on the skyrmion lattice. Second, the experimental set-up and the data treatment procedure correcting for ohmic heating are described. Third, the results of our measurements of the transverse susceptibility of MnSi are presented. A variation of the excitation frequency and amplitude in the skyrmion lattice phase at zero applied current establishes two distinct limits of the susceptibility, representing single-spin and collective responses, respectively. Next, measurements under applied DC current are presented. Following an account for the influence of the applied current on the transverse susceptibility at fixed excitation amplitude, we show that increasing the amplitude leads to the reduction of the critical current density j_c by over one order of magnitude.

3.1. Topologically Non-Trivial Spin-Textures in MnSi

This introduction comprises three parts. First, the properties of cubic helimagnets with a special focus on MnSi and the associated generic magnetic phase diagram is introduced. Second, the non-Fermi liquid regime of MnSi at high pressures is reviewed, which emerges in the vicinity of a quantum phase transition and features the signatures of of spin textures with non-trivial topology. This motivates a comprehensive introduction of skyrmion lattice order in chiral magnets. Here we focus on the topological properties of the magnetic structure and the associated very efficient coupling to spin-currents. Excellent introductions and reviews beyond the scope of this thesis may be found in references [79–84].

3.1.1. The Cubic Helimagnet MnSi

MnSi has started to raise interest along with other monosilicides and monogermanides in the early seventies, when it was identified as a weak itinerant magnet with a helical ground state below a transition temperature $T_c \approx 29\,\mathrm{K}$ [85–87]. MnSi crystallises in the non non-centrosymmetric cubic B20 structure with the P2$_1$3 space group and a lattice constant $a = 4.56$ Å [86]. The helical ground state was identified in neutron scattering experiments, showing a period of $\lambda \approx 180$ Å along the $\langle 111 \rangle$ cubic space diagonals [88–90]. The nature of the magnetic phase diagram and the pressure dependence generated great theoretical and experimental interest and due to extensive efforts over the past decades, most aspects of the low temperature properties of this system are well understood. As a consequence, MnSi represents an ideal candidate to investigate more complex behaviour such as dynamical properties of the magnetic textures or the interplay of conduction electrons with the magnetic structure, as presented in this study [36, 91–96].

a) Magnetic Phase Diagram of Cubic Helimagnets

The magnetic phase diagram of cubic helimagnets, as depicted in figure 3.1, may be fully accounted for by a hierarchy of energy scales that has been pointed out long ago [36]. On the strongest scale, ferromagnetic exchange interactions favour parallel spin alignment. On the second strongest scale, the Dzyaloshinskii-Moriya interaction [91, 92], originating from the lack of inversion symmetry of the underlying crystal structure, favours perpendicular spin alignment. Taken together, both interactions result in the formation of a helical ground state, depicted in figure 3.1 (a). The detailed properties of this ground state are material-specific. A summary of different compounds may be found in references [79, 80]. On the weakest scale, magneto-crystalline anisotropies, representing higher order spin-orbit coupling, give rise to a preferred orientation of the propagation direction of the helix along certain crystallographic directions, such as the $\langle 111 \rangle$ axes in case of MnSi. The combination of all interactions leads to the generic phase diagram show in figure 3.1, which will be discussed in the following for the example of MnSi.
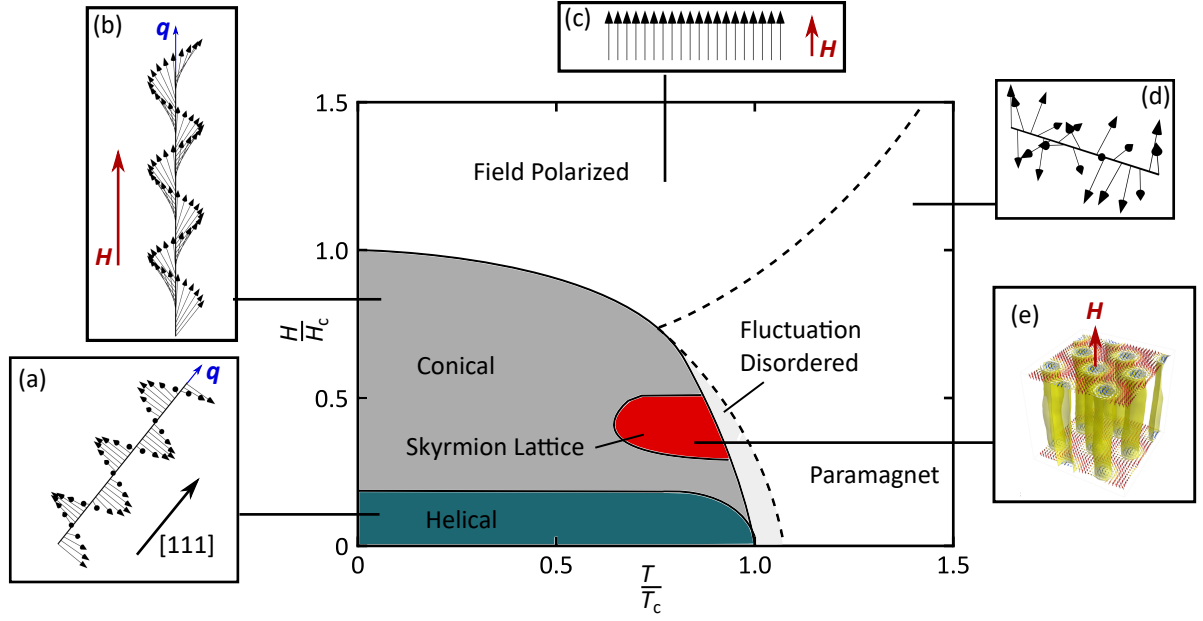
Figure 3.1.: Generic phase diagram of cubic helimagnets. (a) Spin configuration in the helical phase. The helix propagates along the ⟨111⟩ directions for the case of MnSi. (b) - (d) Spin configurations in the conical, field-polarised, and paramagnetic states. (e) Schematic drawing of a skyrmion, stabilising in a hexagonal lattice in a small phase pocket (red). Phase diagram based on [97], figure (e) taken from M. Garst.

At high temperatures, well above $T_c \approx 29\,\mathrm{K}$, the system is paramagnetic with a large fluctuating moment [98] (cf. figure 3.1 (d)). With decreasing temperature, helimagnetic order emerges below T_c. The nature of this transition has been discussed controversially [94, 99–102], however, recent studies by Janoschek *et al.* [103] established conclusively a fluctuation-induced first-order transition, as predicted theoretically by Brazovskii in the late seventies [104]. The transition is accompanied by a fluctuation-disordered regime just above T_c, in which the transition is suppressed due to strongly interacting chiral fluctuations, indicated as a light grey area and enclosed by the dashed line.

Under applied magnetic field, the propagation direction of the helix rotates into the field direction above a transition field $B_{c1} \approx 0.1\,\mathrm{T}$ and the spins are canted towards the propagation vector, forming a conical state (cf. figure 3.1 (b)). This transition has recently been investigated in detail, revealing a complete reorientation as well as putative evidence for topological disclination defects [105]. Above an upper critical field $B_{c2} \approx 600\,\mathrm{mT}$, the system enters a field-polarised state in which all spins are aligned along the applied magnetic field (cf. figure 3.1 (c)). The limits of high-field/low-temperature and high-temperature/low-field are separated by a smooth

crossover. Finally, just below T_c at a small applied magnetic field of $B \approx 200 \, \text{mT}$, the phase diagram exhibits a small phase pocket, first referred to as A-Phase [87, 89]. Small angle neutron scattering (SANS) identified this phase as a lattice of topologically non-trivial magnetic whirls, so-called skyrmions [7]. A schematic drawing of a skyrmion lattice is shown in figure 3.1 (e). The investigation of this magnetic structure represents a central part of this thesis and important properties will be discussed in detail in section 3.1.2.

b) Topological Non-Fermi Liquid at High Pressures

MnSi has attracted great attention already twenty years ago for its distinct properties at high hydrostatic pressures [44]. First studies identified a breakdown of Fermi-liquid theory at a pressure-induced quantum phase transition above a critical pressure $p_c \approx 14.6 \, \text{kbar}$ [11, 106–108]. Here, the helimagnetic ground state is suppressed monotonically with increasing pressure and vanishes completely above p_c. The pressure dependence of MnSi has been studied in great detail and is shown in figure 3.2 [46, 109–111]. Above p_c, neutron diffraction studies [112] could identify a region of partial magnetic order (PO), with the remaining magnetic scattering intensity forming an unusual pattern on the surface of a sphere in reciprocal space, reminiscent of partial order in liquid crystals. Follow up studies of muon spin resonance and nuclear magnetic resonance furthermore identified a region of phase separation (PS) for pressures above $p^* \approx 12 \, \text{kbar}$. The muon relaxation data together with the neutron scattering experiments imply a slow dynamic character of the spin correlations in the partial magnetic order regime (as opposed to being static) on a time-scale between $10^{-10} \, \text{s}$ and $10^{-11} \, \text{s}$ [79, 113].
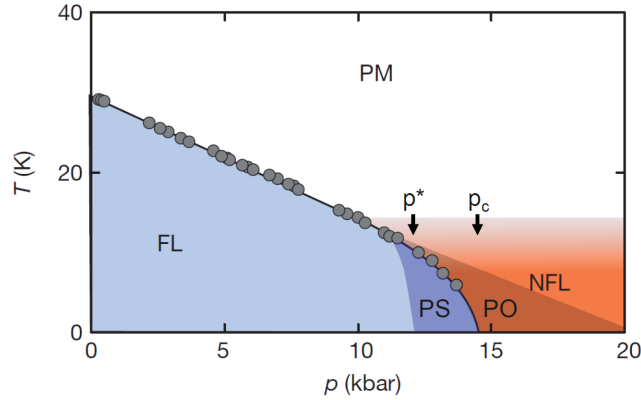

Figure 3.2.: Phase diagram of MnSi as a function of pressure p and temperature T. The resistivity in the magnetically ordered phase obeys the conventional quadratic Fermi-liquid (FL) theory at low pressures and low temperatures. With increasing pressure, the transition temperature is reduced. Above a pressure of $p^* \approx 12 \, \text{kbar}$, a phase separation (PS) is observed in neutron scattering, µSR and NMR, before partial order (PO) and an extended non-Fermi liquid regime (NFL) emerge above the critical pressure $p_c \approx 14.6 \, \text{kbar}$. Figure taken from reference [79], adapted from reference [13].

Even though the ferromagnetic or helimagnetic order in MnSi is suppressed by a non-thermal control parameter, the transition cannot be regarded as a simple example of a conventional quantum critical point (QCP) in an itinerant electron system. This is due to the change from a second-order transition, characteristic for a QCP, to a first-order transition at pressures $p > p^*$ [12]. In many examples, exciting new phenomena have been observed around such ferromagnetic quantum critical points, attributed to strong quantum fluctuations. Examples include an emergent dome of superconductivity as observed for instance in UGe_2 [114] as well as spin-density wave (SDW) order as discussed for $NbFe_2$ [115]. Consequently, it has been discussed, if the Fermi-liquid breakdown in MnSi is driven by the proximity to the quantum critical point. Lamor diffraction studies, combined with the previously discussed results, however, ruled out the quantum critical point as the origin of the extended NFL behaviour in MnSi, consistent with the large extent of the NFL phase of over three times the critical pressure p_c, leaving the origin of the NFL state unidentified.

A recent study by Ritz *et al.* [13, 116] presented measurements of the metallic state of MnSi at high hydrostatic pressures. The authors report that a topological Hall effect (THE), as a key signature of the skyrmion lattice at ambient pressure, persists as the magnetic order is suppressed at large pressures. An introduction to the THE in the skyrmion lattice at ambient pressure will be given in the following section. Moreover, the high-pressure region showing a THE coincides perfectly with the boundaries of the extended NFL regime. Accordingly, the authors conclude that spin correlations with non-trivial topology, which are believed to be the origin of the topological Hall contribution, may drive the breakdown of Fermi-liquid theory in MnSi.

3.1.2. The Skyrmion Lattice

Besides the complex behaviour at high-pressures, great interest in cubic helimagnets over the last decade was attracted by the identification of a new type of complex, topologically non-trivial magnetic order, the skyrmion lattice. In the following, the most important aspects of the skyrmion lattice in MnSi are presented, focussing in particular on topological properties as well as the interaction with the conduction electrons.

The term skyrmion pays tribute to the theoretical physicist Tony Skyrme, who proposed topologically non-trivial solitonic excitations in the context of nuclear field theories in the early sixties [117, 118]. Since then, the concept has been adapted to various fields of physics, including quantum Hall states [119–124], Bose-Einstein condensates [125–127] or liquid crystals [128, 129]. In the context of magnetic materials, skyrmions refer to a certain type of spin whirl exhibiting non-trivial topological winding, which prohibits a continuous transformation of the skyrmion into a

topologically trivial state such as a ferromagnet or a paramagnet. In bulk systems, skyrmions were first observed in a small phase pocket in MnSi, as mentioned above [87, 89], where they stabilise in a two-dimensional trigonal lattice [7]. This lattice can essentially be described by the superposition of three helices where the three propagation vectors q_i are in a plane perpendicular to the applied static magnetic field under an angle of $120°$ with respect to each other. Taken together, the appearance is similar to vortex lines in type-II superconductors [130] as depicted in figure 3.3.
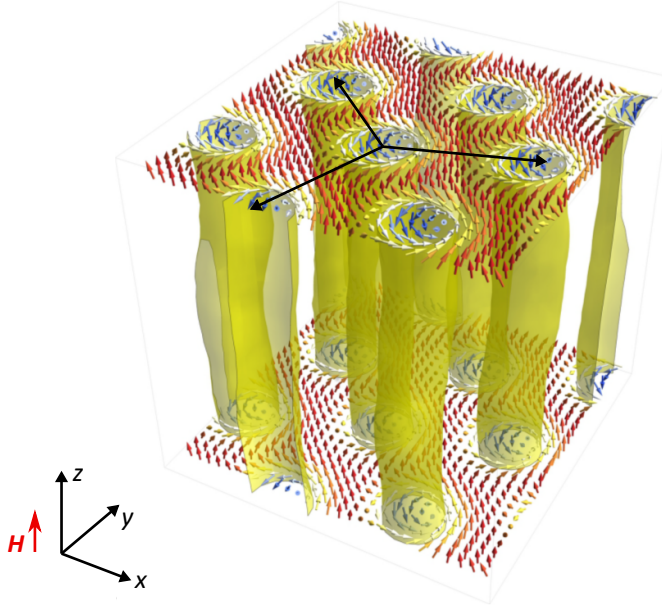

Figure 3.3.: Schematic drawing of a skyrmion lattice. The superposition of three helices (indicated by black arrows) and an uniform magnetisation results in the formation of a two dimensional lattice of skyrmions. Repeating this structure regularly along the external field direction H leads to a formation of skyrmion tubes along the same direction, similar to vortex lines in superconductors. Drawing taken from reference [131].

The identification of the A-Phase, in which the skyrmion lattice stabilises, in MnSi remained an open challenge for over two decades, with several studies falsely interpreting this phase as paramagnetic [132], single-Q spin-flop state [133] or a Bose-Einstein condensate of spin waves [134, 135]. Only in 2009, Mühlbauer *et al.* could identify the A-phase as a lattice of trigonally arranged skyrmion tubes, the skyrmion lattice (cf. figure 3.3), using small angle neutron scattering (SANS). This was followed by similar observations in other cubic helimagnets, showing the same the generic phase diagram as depicted in figure 3.1 [136–140]. Real space observations of the skyrmion lattice using Lorentz force transmission electron microscopy (LTEM) [141, 142],

as well as magnetic force microscopy (MFM) [131], confirmed the interpretation of the SANS data. Recently, even three dimensional measurements of the skyrmion lattice have been reported using electron holography [143]. Selected seminal experimental observations of skyrmion lattices are shown in figure 3.4.

Energetically, the stabilisation of the skyrmion lattice can be captured by a standard Landau-Ginzburg model, taking into account Gaussian thermal fluctuations [7]. This is in contrast to earlier predictions of magnetic vortices, which considered magnetic anisotropies as stabilising mechanism [7, 144, 145]. Despite the observation of skyrmion lattices in bulk materials, a large number of thin film and multi-layer structures could be used to stabilise skyrmions [146–149]. Here, in contrast to bulk samples, typical stabilising mechanisms include strong interfacial Dzyaloshinskii-Moryia interaction, four-spin interactions as well as magnetic anisotropies [83, 146, 150].
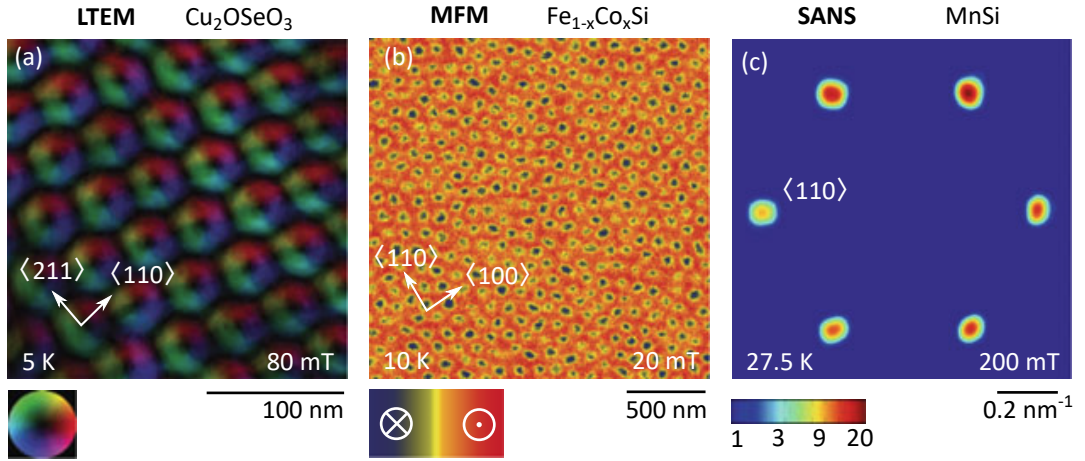

Figure 3.4.: Real space and reciprocal space observation of skyrmion lattices in different B20 compounds. (a) Lorentz Transmission Electron Microscopy (LTEM) of the skyrmion lattice phase in Cu_2OSeO_3 [141, 142] (b) Real space observation of a skyrmion lattice in $Fe_{1-x}Co_xSi$ performed by Magnetic Force Microscopy (MFM) [131] (c) Small Angle Neutron Scattering (SANS) pattern of the skyrmion lattice phase in MnSi [7, 151].

The most intriguing property of the skyrmion lattice, the non-trivial topology, relates to the fact that the magnetic structure is topologically protected and may not be continuously transformed into simple magnetic structures such as a ferromagnet or paramagnet. In general, topology is a mathematical concept that describes properties of structures, which are conserved under a continuous transformation. Two structures are topologically identical, if a continuous deformation from one into another leaves a certain property of the structure, the so-called topological invariant, unchanged. In the skyrmion lattice, this topological invariant is the so-called winding

number, defined as

$$\mathcal{W} = \int\limits_{\text{Unit cell}} \sigma_{\text{top}} \, dx \, dy, \tag{3.1}$$

where σ_{top} is the skyrmion density

$$\sigma_{\text{top}} = \frac{1}{4\pi} \hat{n} (\partial_x \hat{n} \times \partial_y \hat{n}) \tag{3.2}$$

with the magnetisation direction $\hat{n} = \boldsymbol{M}/|\boldsymbol{M}|$[16, 84]. In the case of MnSi, an evaluation of the the winding number in the skyrmion lattice yields $\mathcal{W} = -1$. In contrast, other magnetic phases, such as the conical phase or the paramagnetic phase yield $\mathcal{W} = 0$, indicating a trivial topology.
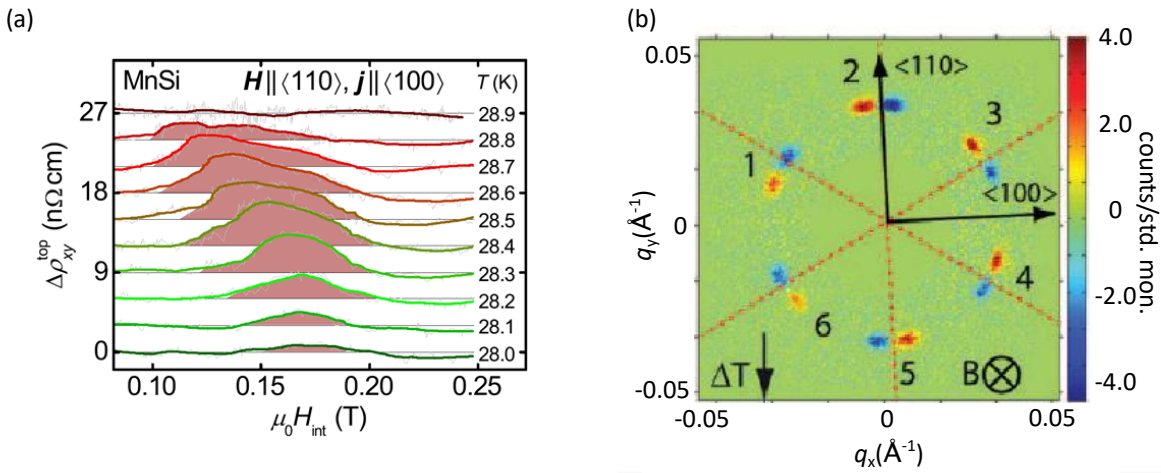

Figure 3.5.: Experimental evidence of the non-trivial topology of the skyrmion lattice phase in MnSi. (a) Measurements of the Hall-effect in the skyrmion lattice phase of MnSi as a function of applied magnetic field. An additional contribution to the Hall-Effect, the topological Hall-effect, $\Delta\rho_{xy}^{\text{top}}$, may be observed as a result of the non-trivial topology of the skyrmion lattice. (b) Small angle neutron scattering (SANS) intensity for two data sets, recorded with an DC current applied to the sample in the skyrmion lattice phase. The spin current leads to a rotation of the 6-fold SANS pattern due to spin-transfer torque effects at ultra low current densities, which originate in the efficient coupling between spin current and topologically non-trivial spin-texture.

Two important consequences of the non-trivial topology of the skyrmion lattice were demonstrated experimentally in the seminal works of Neubauer *et al.* [14], Jonietz *et al.* [15] and Schulz *et al.* [16]. In a study of the electrical resistivity, Neubauer *et al.* first reported a topologically quantised Berry phase contribution to the conventional Hall effect, the so-called topological Hall-effect, as shown in figure 3.5 (a). Additionally, Jonietz *et al.* reported a rotation of the six-fold SANS pattern of the skyrmion lattice when applying a DC current above a certain

threshold current j_c, as shown in figure 3.5 (b). This translates directly to a rotation of the skyrmion lattice in real space as a result of the applied current, representing the observation of so-called spin-transfer torque effects at ultra-low current densities. This observation was complemented by Schulz *et al.*, who detected an emergent electric field as a result of the movement of the skyrmion lattice above j_c, using electrical transport measurements. Both the topological Hall-effect as well as the spin-torque effects observed in MnSi motivated an enormous number of follow-up studies on Skyrmions in solid state physics in general over the past decade (cf. reviews [80, 82, 152] and references therein). Both effects can be captured theoretically in terms of an emergent electrodynamics which is introduced in the following section. Subsequently, the most important experimental work in this context is discussed in more detail.

3.1.3. Emergent Electrodynamics in the Skyrmion Lattice of MnSi

Considering an electron travelling through a topologically non-trivial spin structure $\hat{n}(\vec{r}, t)$, such as a skyrmion. In first approximation, the electron will adiabatically follow the local spin direction and the deflection of the electron can be described in terms of an emergent electrodynamics. In the skyrmion lattice, where the magnetic texture does not vary along the z-direction, the resulting emergent magnetic field $\boldsymbol{B}_z^e$ and emergent electric field $\boldsymbol{E}_\alpha^e$ can be explicitly calculated from the Schrödinger equation [84] as

$$\boldsymbol{B}_z^e = \frac{2\pi\hbar}{e}\sigma_{\text{top}}. \tag{3.3}$$

$$\boldsymbol{E}_\alpha^e = \frac{2\pi\hbar}{e}j_\beta^{\text{top}} \tag{3.4}$$

The emergent fields are determined by the skyrmion density σ_{top} as defined in equation (3.2), representing the non-trivial topology, and by the topological charge current

$$j_\alpha^{\text{top}} = \frac{1}{4\pi}\epsilon_{0\alpha\beta}\hat{n}(\partial_\beta\hat{n} \times \partial_t\hat{n}), \tag{3.5}$$

which is connected to the skyrmion density by the continuity equation [80, 84]. Here, $\epsilon_{0\alpha\beta}$ is the antisymmetric unit tensor and $\alpha, \beta = x, y$.

a) Topological Hall-Effect

The emergent magnetic field of the static skyrmion crystal $\boldsymbol{B}_z^e$ can be regarded as an ficti-tious internal field B^{eff} which leads to an additional contribution to the Hall effect. As $\boldsymbol{B}_z^e$ is a direct consequence of the non-trivial topology, this contribution is called topological Hall effect (THE) ρ_{xy}^{top}. In a semi-classical picture, the topological Hall effect corresponds to a Berry phase in real space, which is picked-up when the electron adiabatically adapts to the local magnetisation while passing through a topologically protected spin texture. A complete semi-classical analysis is beyond the scope of this thesis, however, note that besides the Berry phase in

real space, there also exists a contribution in momentum space, which gives rise to the intrinsic anomalous Hall-effect, as well as combinations of Berry phases in real and momentum spaces, which are not explored experimentally in detail, yet [116].

To estimate the size of the topological Hall-effect quantitatively, several assumptions have to be made and a detailed account may be found in reference [116]. In the limit of low temperatures, where interband (spin-flip) scattering is strongly suppressed, the THE may then be approximated by

$$\rho_{xy}^{\text{top}} = R_0 B^{\text{eff}} P, \tag{3.6}$$

where R_0 is the conventional Hall constant, capturing the intraband (non-spin-flip) scattering and P is the charge carrier spin polarization. It is interesting to note that ρ_{xy}^{top} is proportional to the emergent magnetic field $\boldsymbol{B}^{\text{e}}$ and hence to the skyrmion density σ_{top}, leading to a vanishing contribution for topologically trivial structures.

In the skyrmion lattice in MnSi, the the topological Hall contribution was first observed by Neubauer *et al.* [14], who reported a THE in the order of $\rho_{xy}^{\text{top}} \approx 5 \text{n}\Omega\text{cm}$ (cf. figure 3.5). A subsequent study, however, corrected this value to $\rho_{xy}^{\text{top}} \approx 50 \text{ n}\Omega\text{cm}$ by accounting correctly for finite temperature effects such as spin-flip scattering, yielding an effective field value of $|B^{\text{eff}}| \approx 13 \text{ T}$ [13]. This is in accordance with a direct calculation of the effective field, which yields $|B^{\text{eff}}| \approx 13.15 \text{ T}$ [13].

Subsequently, additional Hall contributions have been observed in a number of similar, non-centrosymmetric B20 helimagnets, such as FeGe or the doping series $\text{Fe}_{1-x}\text{Co}_x\text{Si}$ or $\text{Mn}_{1-x}\text{Fe}_x\text{Si}$ [153–155]. However, large unconventional Hall contributions have not only been observed in connection with the skyrmion lattice, but also in a large number of distinct compounds, mediated by different microscopic properties. Examples include the short period non-coplanar helimagnet MnGe [156], where the unconventional Hall effect is believed to be of topological nature, and the double-exchange ferromagnet CrO_2 [157] where an additional contribution to the Hall effect is caused by topological defects. Large anomalous Hall effects have also been reported earlier in non-topological structures like frustrated magnets with pyrochlore structure, with the most prominent examples being $\text{Pr}_2\text{Ir}_2\text{O}_7$ or $\text{Nd}_2\text{Mo}_2\text{O}_7$ [158–160]. Most recently, an additional contribution to the Hall effect has been discovered in the non-collinear antiferromagnetic phases of the series Mn_3Sn, Mn_3Ir and Mn_3Ga as well as in Mn_5Si_2 [161–163].

b) Spin-Transfer Torques

We have seen in the last section that an electron, passing through the skyrmion lattice, will be deflected by the magnetic structure, leading to an additional contribution to the Hall effect. In accordance to Newton's second law, this implies that the electron itself will transfer a momen-

tum to the magnetic structure as it passes through the skyrmion. This concept, referred to as spin-transfer torque, is well known for conventional ferromagnets, where magnetic domain walls can be moved by a strong spin current [164–167]. This mechanism was considered of particular interest in the context of magnetic data storage for many years, and the recent proposal of so-called race-track memories, in which information is stored in magnetic domains which are moved through nano-wires by an applied spin current, has attracted additional attention over the past decade [18, 168]. However, up to now, a large scale realisation of a spin torque based memory device was prevented by several problems such as very high threshold current densities, so-called critical currents, in the order of $10^9 - 10^{11} \, \text{Am}^{-2}$ as well as small drift velocities of the domain walls [169].

In MnSi, spin-torque effects were first observed in SANS measurements as well as in Hall-effect measurements revealing extremely low current densities of below $10^6 \, \text{Am}^{-2}$ [15, 16]. The small critical currents were ascribed to a combination of low collective pinning of the skyrmion lattice and the strong coupling of the conduction electrons to the magnetic structure, as a result of the non-trivial topology [15]. A full theoretical account for spin torque effects in MnSi lies beyond the scope of this thesis. Nevertheless, we want to emphasis the most important aspects of the theoretical descriptions given in references [84, 170, 171].

The dynamic orientation of the magnetisation $\hat{n}(\boldsymbol{r}, t) = \boldsymbol{M}(\boldsymbol{r}, t)/|\boldsymbol{M}(\boldsymbol{r}, t)|$ of a magnetic texture, such as a skyrmion, in the presence of a spin current is given by the generalised Landau-Lifschitz-Gilbert (LLG) equation [167, 172, 173]

$$[\partial_t + (\boldsymbol{v}_s \nabla)]\hat{n} = -\gamma \hat{n} \times B_{\text{eff}} + \hat{n} \times [\alpha \partial_t + \beta(\boldsymbol{v}_s \nabla)]\hat{n} \tag{3.7}$$

with the effective spin velocity $\boldsymbol{v}_s$ parallel to the spin current and two relaxation constants α and β, describing a Gilbert damping and a dissipative spin-transfer torque, respectively. Careful theoretical considerations show that this description can be simplified by projecting equation 3.7 onto the translational mode and integrating over the full magnetic unit cell, following the so-called Thiele approach [84, 170, 174–176]. The equation of motion for a single skyrmion at site $\boldsymbol{x}(t)$ is then given by

$$\underbrace{\boldsymbol{G} \times [\boldsymbol{v}_s - \dot{\boldsymbol{x}}(t)]}_{\boldsymbol{F}_{\text{Magnus}}} + \underbrace{\boldsymbol{D}[\beta \boldsymbol{v}_s - \alpha \dot{\boldsymbol{x}}(t)]}_{\boldsymbol{F}_{\text{Drag}}} = \boldsymbol{F}_{\text{Pinning}}. \tag{3.8}$$

The first part of the left side of this equation represents a Magnus force, $\boldsymbol{F}_{\text{Magnus}}$, acting perpendicular to the spin current with the gyromagnetic coupling vector

$$G_i = \mathcal{G}\hat{B}_i, \quad \mathcal{G} = 4\pi M \mathcal{W}, \tag{3.9}$$

which is proportional to the topological winding number $\mathcal{W} = -1$ (cf. equation (3.1)). The second part represents a drag force $\boldsymbol{F}_{\mathrm{drag}}$, acting parallel to the spin current with a dissipative tensor $\boldsymbol{D}$. Both forces counteract to the material specific pinning forces $\boldsymbol{F}_{\mathrm{Pinning}}$, which may only be accounted for phenomenologically [177–179]. A schematic drawing of the forces acting on the skyrmion lattice due to an applied current j is shown in figure 3.6 (a).
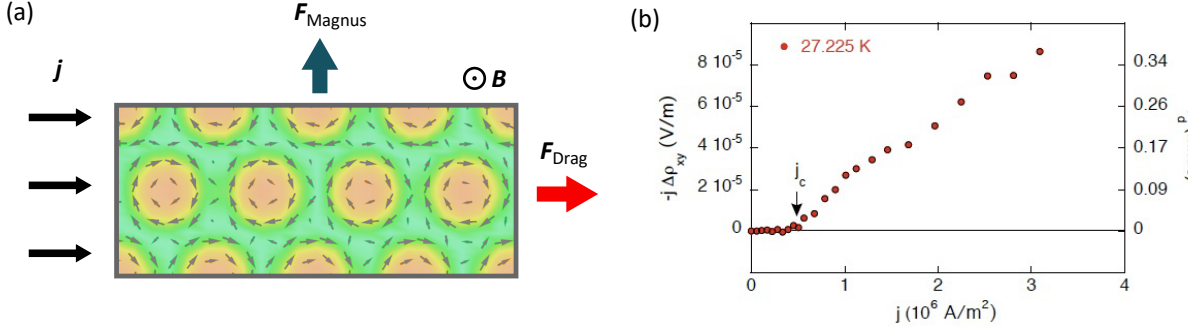
Figure 3.6.: Spin-transfer torque effects in MnSi. (a) Schematic depiction of the forces acting on the skyrmion lattice with applied current density $\boldsymbol{j}$. The skyrmion lattice is stabilised by a magnetic field B pointing out of the plane. The applied spin current $\boldsymbol{j}$ causes a Magnus force F_{Magnus}, perpendicular to the current direction, and a drag force F_{Drag}, resulting in a drift of the skyrmion lattice in the plane of the current flow above a critical current density j_c. Depiction of the skyrmion lattice by W. Simeth. (b) Drift velocity of the skyrmion lattice as a function of applied current density j. Above a critical current j_c the magnetic structure depins and starts to move. Figure taken from reference [16].

The skyrmion, which moves through the sample will, in analogy to the THE, generate an emergent electric field $\boldsymbol{E}^{\mathrm{e}}$, proportional to the drift velocity $\boldsymbol{v}_d$ [16, 180]

$$\boldsymbol{E}^e = -\boldsymbol{v}_d \times \boldsymbol{B}^e. \tag{3.10}$$

Naturally, this additional field will influence the Hall effect measurements in terms of an emergent Lorentz force. The emergent electric field perpendicular to the spin current direction is therefore connected to a reduction of the topological Hall effect as follows:

$$\Delta E_\perp = \Delta\rho_{yx} \cdot j = -\Delta\rho_{xy} \cdot j. \tag{3.11}$$

Schulz *et. al* [16] were able to detect this reduction of the topological Hall effect and connect it to the size of the emergent electric field and, thus, to the drift velocity of the skyrmions as shown in figure 3.6 (b). Consequently, they were able to extract the critical current density j_c, above which the skyrmion lattice starts to move. This critical current density of $j_c \approx 0.5$ MAm^{-2} is enhanced for temperatures just below the transition temperature T_c, but stays constant throughout the

whole skyrmion lattice phase to its lower temperature boundary. These measurements represent the first observation of emergent electrodynamics in connection with spin-transfer torques in a skyrmion lattice.
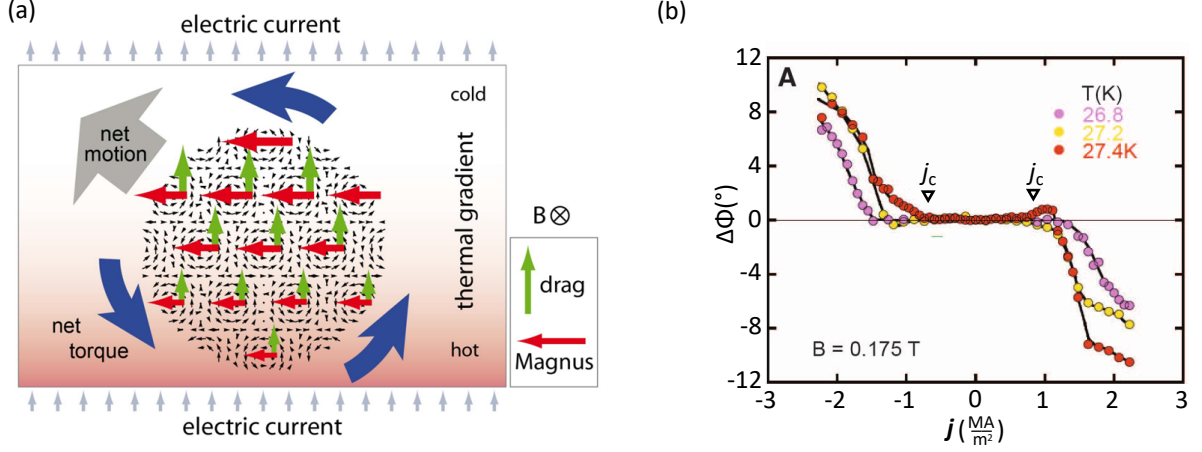

Figure 3.7.: Observation of spin-transfer torques in small angle neutron scattering (SANS). (a) Schematic depiction of the forces acting on the skyrmion lattice with an electric current and a thermal gradient applied to the sample. The thermal gradient results in a variation of the forces, leading to a rotation of the skyrmion lattice, additional to a linear motion. (b) Relative rotation of the scattering pattern of the skyrmion lattice $\Delta\Phi$ as a result of the applied current density j at different temperatures. A rotation may be clearly observed above $j_c \approx 0.8\,\mathrm{MAm}^{-2}$ as indicated by black triangles. Figures adapted from reference [15].

The first direct observation of spin-transfer torques in MnSi was realised in SANS experiments [15]. However, as the reciprocal image of the lattice remains unchanged for a translational movement of the lattice in real space, it was necessary to apply an additional thermal gradient to the sample to visualise spin-torque effects. Figure 3.7 (a) shows the influence of a thermal gradient, together with an applied electric current, on the forces acting on the skyrmion lattice. Both, the strength of the Magnus force, as well as the strength of the drag force are dependent on the temperature and are more pronounced on the cold side of the sample. In total, this results in a net rotational movement of the skyrmion lattice, which can directly be captured by SANS measurements. The rotation was shown in figure 3.5 (b), where two scattering patterns of inverted current directions are depicted. In their work, Jonietz *et al.* could connect this clear rotational effect unambiguously to the rotation of the skyrmion lattice as a result of spin-transfer torques [15]. In figure 3.7 (b), the relative rotation $\Delta\Phi$ is shown as a function of applied current density j, where the critical currents j_c are indicated by triangles. Theoretically, the rotation of the skyrmion lattice may be described by the LLG equations in combination with additional damping terms and a phenomenological account for pinning forces, as reported by Everschor *et al.* [175]. Note that spin torque effects may only be observed when the current is

applied perpendicular to the skyrmion tubes, i.e. perpendicular to the applied magnetic field. Recently, a rotation of the skyrmion lattice could also be observed in insulating compounds such as Cu_2OSeO_3, where the momentum transfer is mediated by magnon currents [181–183].

The discovery of the low threshold currents in the skyrmion lattice motivated a large number of follow up studies, trying to explore the nature and potential applications of spin-torque effects in detail. This includes theoretical and experimental studies trying to create, stabilise, annihilate and move single skyrmions in thin-films, multi-layers and nano-wires [19, 21, 184–188]. However, only a few studies recently focused on the origin of the low current threshold or the detailed nature of the interactions and pinning forces in skyrmion lattices [189–191]. A theoretical study by Iwasaki [189] recently reported on micromagnetic details of the skyrmion movement, however focussing on the movement at high current densities, exceeding $10^8 \, \text{MAm}^{-2}$.

One particularly important study in the context of this thesis was performed by Mühlbauer *et al.* [192], who investigated the elasticity and the impurity pinning in the skyrmion lattice phase in MnSi using time-resolved small angle neutron experiments (TISANE). In their work, a small oscillating magnetic field B_{AC} was applied in addition to the static magnetic field B_{stat}, stabilising the skyrmion lattice, as shown in figure 3.8 (a). A schematic depiction of the measurement configuration is shown in figure 3.8 (b). As their main result they report an oscillation of the magnetic scattering intensity as a function of time, representing a tilting motion of the skyrmion lattice, as a result of the applied oscillating field (cf. figure 3.8 (c)). The oscillatory movement of the skyrmion lattice, however, shows a threshold amplitude of the oscillating field, below which no motion is visible. This appears closely related to spin torque effects, where a motion of the skyrmion lattice can only be observed above a critical current j_c. Mühlbauer *et al.* concluded that this behaviour is characteristic for an unpinning of the skyrmion lattice from defects at a frequency of $f = 325 \, \text{Hz}$ and for oscillation amplitude exceeding a threshold of approximately $\epsilon_c \approx 0.4°$. In the skyrmion lattice phase, where $B_{stat} \approx 200 \, \text{mT}$, this corresponds to an amplitude $B_{AC} \approx 4 \, \text{mT}$.

In this study, the response of the skyrmion lattice to an oscillating magnetic field is studied over a broad range of excitation frequencies and amplitudes. In agreement with the study of Mühlbauer, we observe an unpinning of the skyrmion lattice in a certain range of excitation frequencies and amplitudes. Additionally, the effects of an applied oscillating magnetic field are investigated in combination with an applied DC current. Consistent with previous studies [15, 16], we observe spin torque effects as a result of the applied current density and find that the critical current density j_c is reduced by the additional application of a strong oscillating magnetic field.
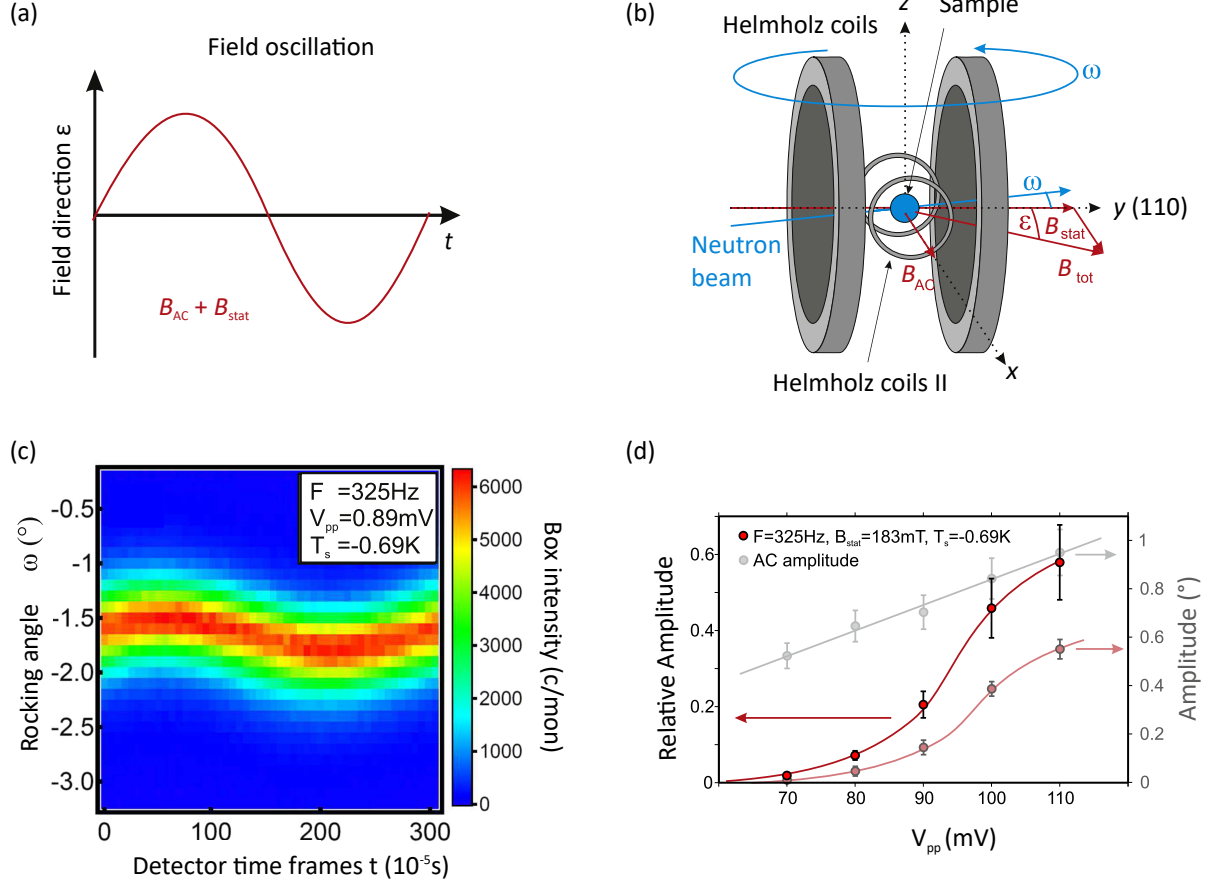
Figure 3.8.: Time resolved small angle neutron experiment (TISANE) in the skyrmion lattice phase of MnSi. (a) Field direction ϵ of the total magnetic field B_{tot} as a function of time. A combination of a static magnetic field B_{stat}, used to stabilise the skyrmion lattice, and a small oscillating magnetic field B_{AC} result in an effective rotation of the field direction. (b) Measurement configuration of the TISANE experiment. B_{AC} is applied along the x-axis, perpendicular to B_{stat}. The neutron beam is applied parallel to B_{stat} and rotated by an rocking angle ω in the x-y plane. (c) Scattering intensity of the skyrmion lattice as a function of time at a temperature $T_s = -0.69\,\text{K}$ below the critical temperature T_{cA}. The sinusoidal shape representing the field direction ϵ is clearly visible for a frequency $f = 325\,\text{Hz}$ and an amplitude of $V_{\text{pp}} = 0.89\,\text{mV}$. (d) Relative amplitude of the scattering pattern compared to the absolute oscillation amplitude of the magnetic field as a function of the field amplitude. It is visible that the magnetic structure starts to oscillate with an amplitude of up to 0.5° above a critical oscillation amplitude of the magnetic field $V_{\text{pp}} \geq 80\,\text{mV} \,\hat{\approx}\, 0.6°$.

3.2. Experimental Methods

In this section, important aspects of the experimental environment are discussed. After a description of the samples and the sample holder used in this study, properties of the cryogenic environment and their implications on the measurements reported in this chapter are discussed. Subsequently possible measurement disturbances are addressed. First, the influence of ohmic heating as a consequence of the strong applied DC currents is discussed in detail and a generic temperature correction routine is presented. Then, the additional influence of magnetoresistance effects on this correction is estimated. Finally, a possible disturbance of the collected data by Oersted fields, generated by the applied current, is addressed at the end of this section.

3.2.1. Samples

Three different single crystalline samples, prepared by optical float zoning, were studied. Details on the single crystal preparation may be found in reference [81]. X-Ray Laue diffraction was used to orient the samples and a wire saw was used to cut small oriented cuboids. An overview over all samples may be found in table 3.1. All samples and their crystallographic orientations are shown in figure 3.9. Samples A and B are cubic with 2 mm edge length. These samples have been used to perform longitudinal and transverse susceptibility measurements, respectively. Sample C was used for the spin-transfer torque measurements. Its dimensions are 0.41 mm x 0.88 mm x 3.15 mm, with a crystallographic $\langle 001 \rangle$ axis normal to the largest surface, and a $\langle 110 \rangle$ axis parallel to the longest side of the sample. Current contacts have been soldered to the smallest sides of the sample to generate a current flow along the crystallographic $\langle 110 \rangle$ direction. The contacts are shown in figure 3.10 (c). Sample C exhibits a residual resistivity ratio of 80, as typical for samples studied in the literature [81].

Sample	Growth number	Dimensions (mm) l x w x h	Measurement
A	OFZ16-L3-44	2 x 2 x 2	LS
B	OFZ69-3-2-6-k	2 x 2 x 2	TS
C	OFZ69-3-2-7-e3	3.15 x 0.88 x 0.41	TS + STT

Table 3.1.: Overview of the MnSi samples studied in this thesis. Samples A and B are cubic with 2 mm edge length and used for transverse susceptibility (TS) and longitudinal susceptibility (LS) measurements. Sample C is a thin cuboid used for the spin-transfer torque experiments (STT) in combination with transverse susceptibility measurements. A photograph of the samples and a schematic drawing of the crystallographic orientations may be found in figure 3.9.
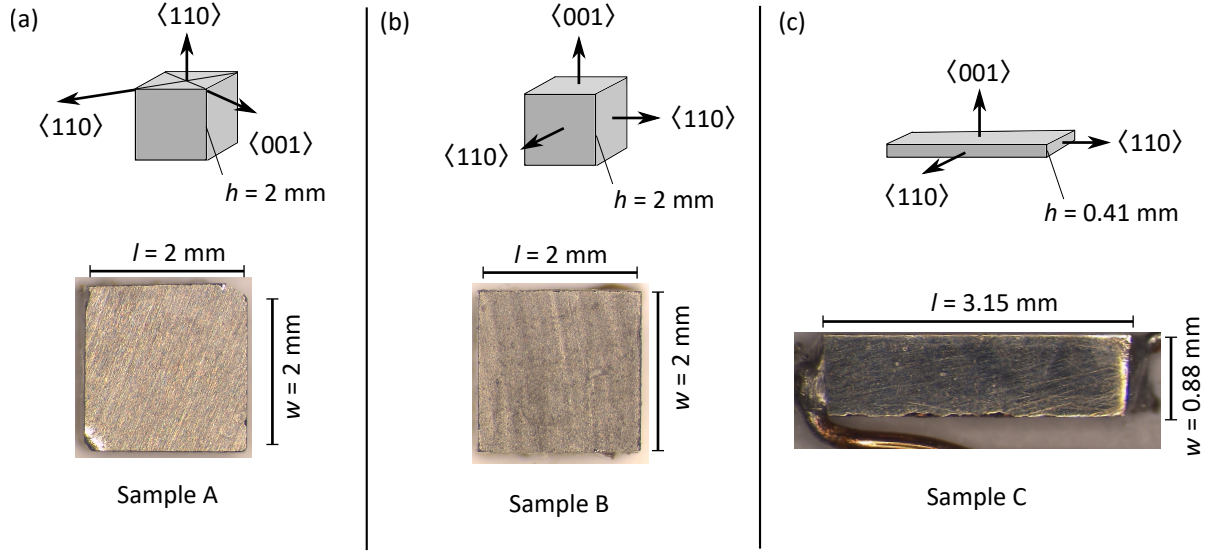
Figure 3.9.: Photograph and crystallographic orientations of the MnSi samples used in this study. (a) Sample A: Cube with $2\,\mathrm{mm}$ side length, used for the longitudinal susceptibility measurements. (b) Sample B: $2\,\mathrm{mm}$ cube used for transverse susceptibility measurements without applied DC current. (c) Sample C: 0.41 mm thick cuboid, used for the transverse susceptibility measurements with applied DC current. The soldered contacts of the current wiring are visible at both ends of the sample, resulting in a current flow along a crystallographic $\langle 110 \rangle$ direction.

3.2.2. Sample Holder

For our measurements, we used the bespoke low-noise susceptometer, described in section 1.2.2. This susceptometer may be used in combination with the two types of sample holders, shown in figures 3.10 (a) and (b). The first sample holder (figure 3.10 (a)) is a cylinder made of polyether ether ketone (PEEK) to which the sample is attached using GE varnish. The holder was used to measure the longitudinal and transverse AC susceptibility without DC current. Figure 3.10 (a) shows sample B mounted to the holder. The longitudinal static field B is applied along the cylinder axis, parallel to the excitation field B_{AC}. The transverse field B is applied perpendicular to the cylinder axis. The sample holder used for the spin torque experiments is shown in figure 3.10 (b). Here, the sample was mounted on a $0.2\,\mathrm{mm}$ sapphire plate using GE Varnish and Teflon ribbon. A schematic drawing of the sample holder with a sample mounted is shown in figure 3.10 (c). Two 250 µm enamelled copper wires provide the electrical contacts for the DC currents resulting in a current flow along a crystallographic $\langle 110 \rangle$ direction. Next to the sample a *Lake Shore* Cernox CX-1030 SD temperature sensor was mounted on the sapphire plate to track the sample temperature. The sapphire plate provides an excellent thermal contact between sample and thermometer due to high thermal conductivity of the sapphire plate and systematic errors are minimized. Furthermore, a $1\,\mathrm{mm}$ silver wire connects the sapphire plate and the sample stick to ensure thermal equilibrium between sample stick and sample holder.
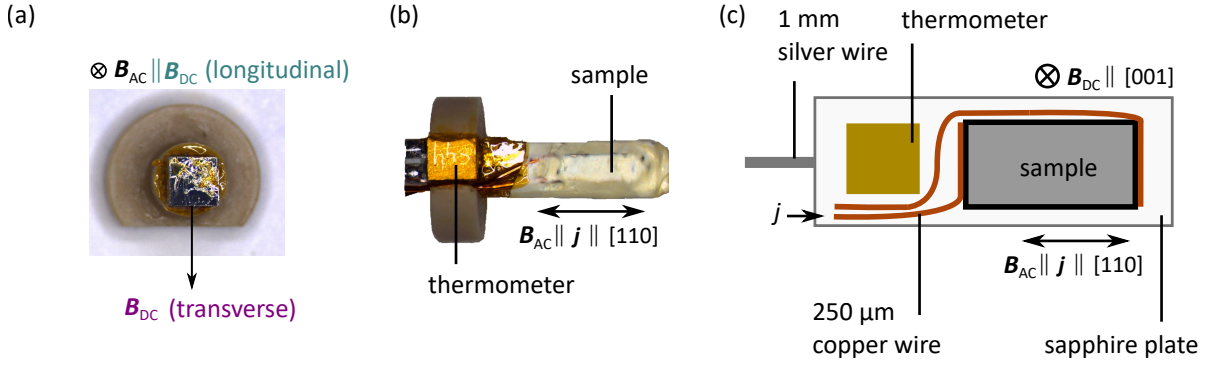
(a)

$\otimes \boldsymbol{B}_{AC} \| \boldsymbol{B}_{DC}$ (longitudinal)

$\boldsymbol{B}_{DC}$ (transverse)

(b)

sample

$\boldsymbol{B}_{AC} \| \boldsymbol{j} \| [110]$

thermometer

(c) 1 mm silver wire   thermometer

$\otimes \boldsymbol{B}_{DC} \| [001]$

$j \rightarrow$

sample

250 μm copper wire

$\boldsymbol{B}_{AC} \| \boldsymbol{j} \| [110]$

sapphire plate

Figure 3.10.: Overview of sample holders used in this study. (a) Photograph of the sample holder for longitudinal and transverse susceptibility measurements without DC current. The sample is mounted to the PEEK holder using GE Varnish. (b) Photograph of the sample holder for the spin torque experiments. The sample is wrapped in a thin layer of Teflon ribbon to fix the sample on the holder. (c) Schematic drawing of the measurement configuration on the spin torque sample holder. Two 250 μm enamelled copper wires are soldered to the small sides of the sample as current contacts. The sample and wires are mounted on a sapphire plate. A Lake Shore Cernox temperature sensor is mounted onto the same sapphire plate close to the sample to ensure good thermal contact. The sample holder is thermally coupled to the sample stick by a 1 mm silver wire, as well as exchange gas.

3.2.3. Cryogenic Environment

All measurements presented in this chapter were carried out in an *Oxford Instruments* Variable Temperature Insert (VTI), mounted in a $16\,\mathrm{T}$ He^4 bath magnet cryostat described in sections 1.2.5 (a) and (c). A sample stick with a rotatable platform as support of the susceptometer was used, permitting to rotate the cylindrical axis of the susceptometer with respect to the applied magnetic field. This provided the possibility to switch between longitudinal and transverse field geometries for the susceptibility measurements. The susceptometer as mounted for the transverse field geometry is shown in figure 3.11. The temperature of the cryostat was set by means of the helium gas flow, regulated by a needle valve, and a resistive heater. During the measurements a PID-controller adjusted the needle valve and heater current to maintain a constant temperature in the sample chamber. To reduce the helium consumption, the controller is programmed to gradually reduce the heater power and needle valve percentage continuously to a predefined minimal value, while keeping the temperature constant. In general, this behaviour is desired and does not influence the measurement. However, if the gas flow is reduced, the pressure in the sample chamber decreases and the cooling power of the system changes. In the case of spin-transfer torque experiments, where the ohmic heat generated in the sample is of comparable size as the cooling power of the cryostat, this will have an influence on the effective sample temperature, even if the cryostat temperature may be kept constant. Therefore, to

achieve a constant cooling power, the needle valve was adjusted to a constant value. However, even for these conditions, a small thermal gradient of order $1\,\mathrm{K}$ between sample and sample thermometer could not be avoided. To account for this effect, a complex temperature correction was applied, as described in the following.
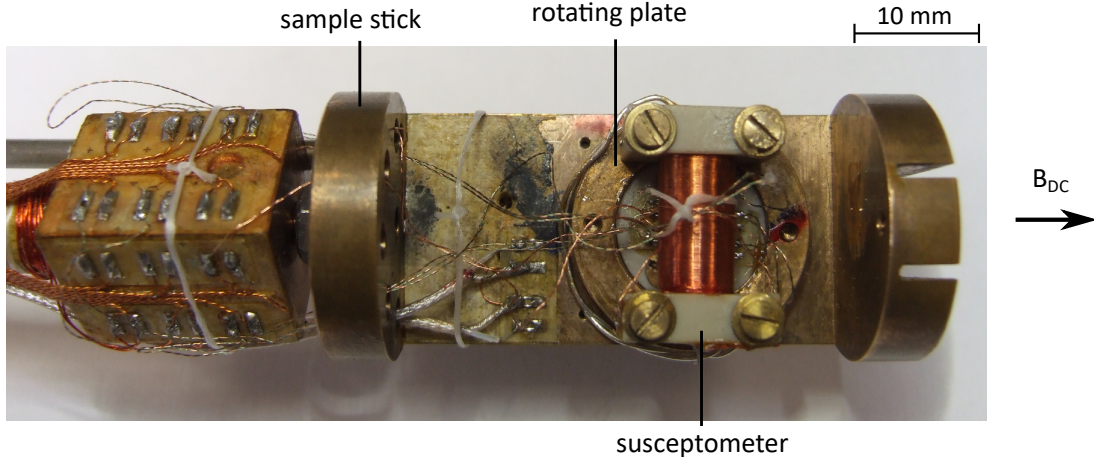

Figure 3.11.: Sample stick with the bespoke susceptometer, used for all susceptibility measurements on MnSi. The susceptometer is mounted on a rotating plate capable to change the orientation from longitudinal to transverse, with the applied field direction pointing along the sample stick. The photograph shows the configuration for measurement in transverse fields. The sample holder was additionally connected to the sample stick for better thermal coupling by a $1\,\mathrm{mm}$ silver wire.

3.2.4. Temperature Correction

Despite the efforts described above to reduce temperature differences between the sample and the thermometer during the spin torque experiments, a small remaining gradient made a complicated temperature correction necessary. Figure 3.12 summarises the temperature definitions used in the following paragraph. In this set up, the control temperature of the cryostat defines the temperature of the gas flow in the sample chamber, T_{cryo}. The temperature, recorded by the sample thermometer, T_{ST}, which is mounted close to the sample on a sapphire plate, usually represents a reliable value of the actual temperature of sample, T_{S}. However, in spin torque experiments, ohmic heating, generated by the applied DC current, might locally heat the sample and result in a thermal gradient between T_{S} and T_{ST}. This temperature offset, $\Delta T = T_{\mathrm{S}} - T_{\mathrm{ST}}$, depends on a number of variables:

a) The cooling power P of the cryostat, which varies as a function of temperature and which can not be determined easily.

b) The ohmic heating in the sample, which varies as a function of the applied current I.

c) The applied magnetic field B, which changes the sample resistivity and consequently the ohmic heating in the sample.

In this paragraph, a procedure is presented which allows to correct for the effects of a) and b). Section 3.2.5 will address the influence of magnetoresistance effects, c).
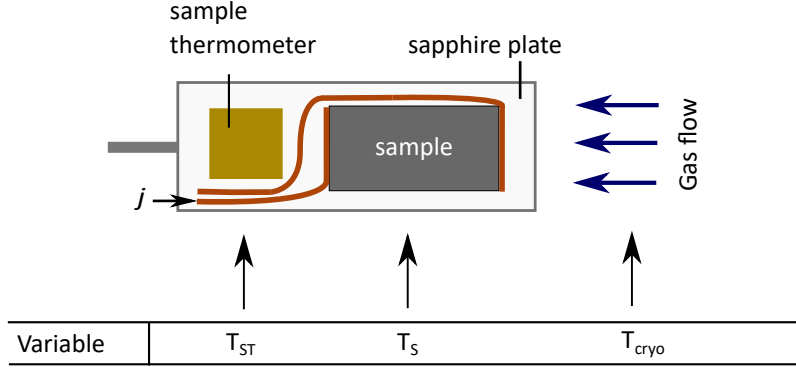

Figure 3.12.: Schematic depiction of important temperature definitions during a spin torque experiment. T_{ST} represents the temperature, detected by the sample thermometer. T_{s} denotes the actual sample temperature, which might show an offset compared to T_{ST} as a result of internal ohmic heating due to the applied DC current density j. T_{cryo} represents the control temperature of the cryostat.

A flow chart of the temperature correction is shown in figure 3.13. Note that the temperature correction presented here assumes a constant transverse susceptibility in the field-polarised phase of MnSi as a function of applied DC current I. This assumption appears valid here, as spin torque effects in the ferromagnetic regime are restricted to current densities exceeding the currents presented in this study by several orders of magnitude.

In this study, the transverse susceptibility was recorded as a function of an applied magnetic field between $B = 0$ and $B = 0.7\,\mathrm{T}$ at several temperatures between $T = 27\,\mathrm{K}$ and $T = 29\,\mathrm{K}$. These measurements were repeated at different applied currents between $I = 0$ and $I = 1\,\mathrm{A}$. Two typical data sets, recorded at the same temperature $T_{ST} = 28\,\mathrm{K}$, detected by the sample thermometer, and $I = 0$ and $I = 1\,\mathrm{A}$, respectively, are shown in figure 3.13 (a). The measurement curve at $I = 1\,\mathrm{A}$ is shifted, compared to the curve recorded at zero current. The main part of this shift, however, is not attributed to spin torque effects, but to ohmic heating of the sample at high currents which increases the effective sample temperature T_{s}. Hence, the temperature detected by the sample thermometer, T_{ST}, is only reliable at zero current, while the sample temperature during the high current measurements, T_{s}, is unknown and must be determined.

To correct for this effect, as a first step, all measurements recorded at the same DC current are interpolated on a fine 2D grid to obtain the transverse susceptibility $\chi_\perp$ as a function of
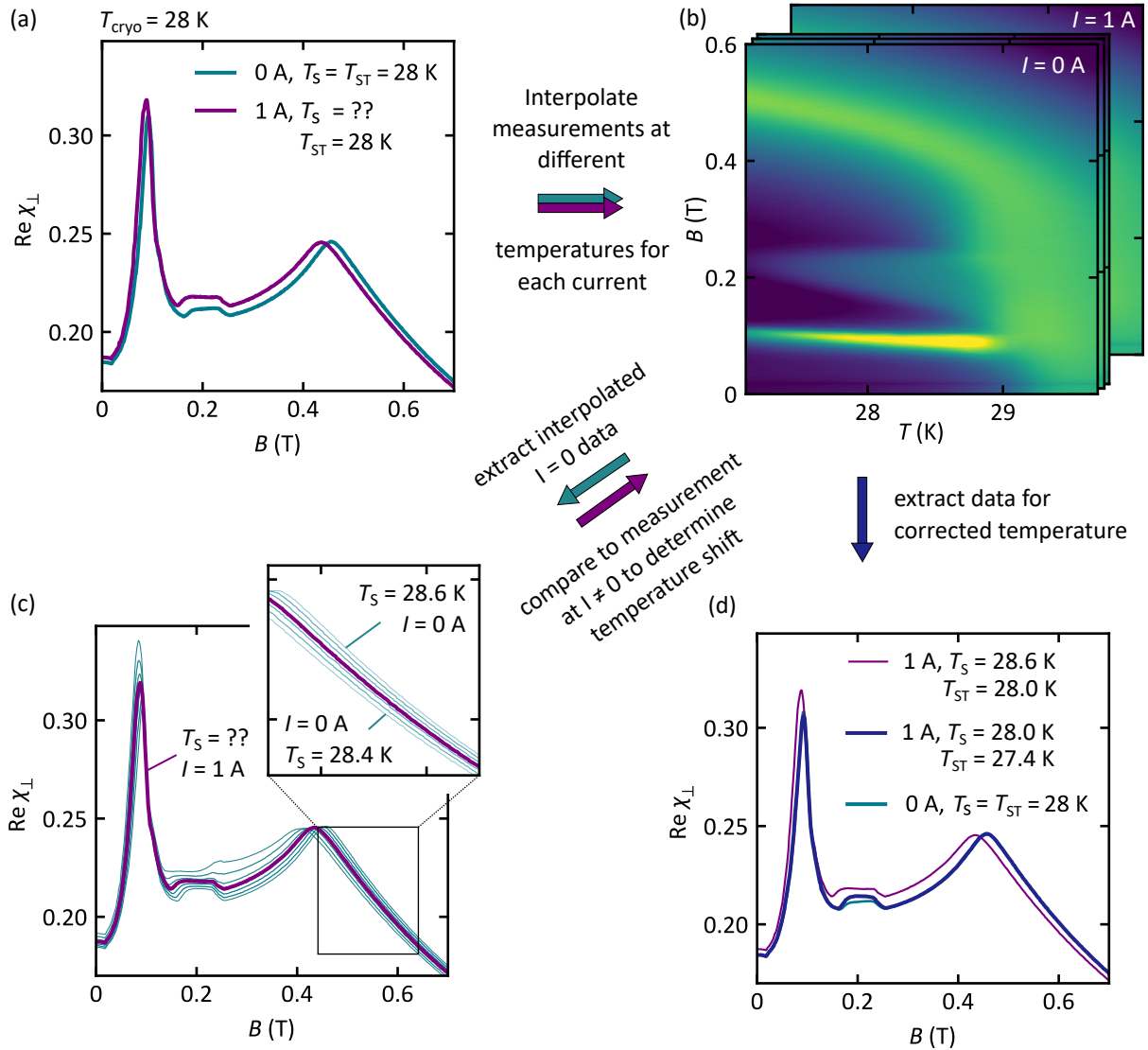
Figure 3.13.: Flow chart of the temperature correction for ohmic heating effects. (a) Measurements taken at $T_{\mathrm{cryo}} = 28\,\mathrm{K}$ and $I = 0$ and $I = 1\,\mathrm{A}$ DC current are shown as generic example. Due to ohmic heating, the temperature of the measurements at non-zero current is unknown. (b) Individual 2D data grids are generated by interpolation of magnetic field sweeps at different temperatures for each DC current. (c) By minimising the difference between the high current measurement (purple curve) and the zero current data grid (light green curves) in the field polarised region between $450\,\mathrm{mT}$ and $650\,\mathrm{mT}$, the effective sample temperature can be determined, assuming a current independent susceptibility in this region. (d) The determined sample temperature is used to extract the high current measurement curve from the corresponding grid which can then be compared to measurements at the same sample temperature, but different DC current (blue and green curve).

magnetic field B and temperature T, as depicted in figure 3.13 (b). This interpolation is repeated for each current investigated in this study. Then, the measurement curve at non-zero current may be compared to the 2D grid of magnetic field sweeps at zero spin torque current. Figure 3.13 (c) shows the curve at non-zero current (purple) and a set of magnetic field sweeps at different temperatures, extracted from the 2D grid for $I = 0$ (light green). Assuming the absence of spin torque effects in the field polarised state of the sample, i.e. above $B \approx 450\,\mathrm{mT}$, we expect the susceptibility of magnetic field sweeps taken at zero current and taken at non-zero current to overlap between $B = 0.45\,\mathrm{T}$ and $B = 0.65\,\mathrm{T}$, if they are recorded at the same sample temperature. Therefore, the zero current measurement with the best overlap with the non-zero current measurement in this regime is identified and we can assume that both curves are taken at the same sample temperature T_s. As T_s is known for the zero current measurement, we can assume that the non-zero current measurement was taken at the same sample temperature and the temperature offset ΔT of this measurement may be determined.
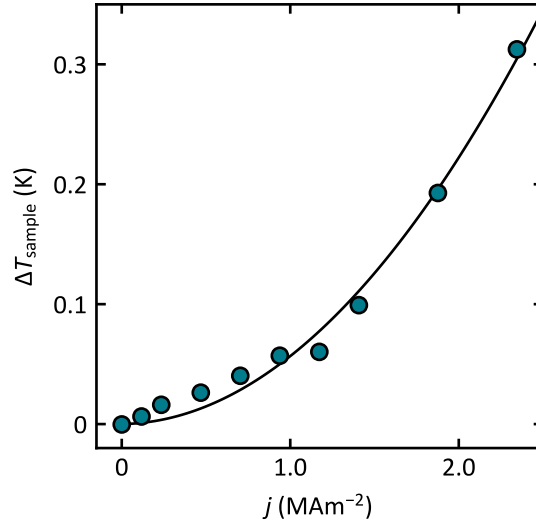

Figure 3.14.: Temperature shift of the sample temperature T_s compared to the temperature, recorded by the sample thermometer, T_ST, as a function of applied DC current j. The dots indicate the temperature shift, determined by the correction procedure shown in figure 3.13. The black line shows a quadratic fit to the temperature shifts confirming the expected quadratic behaviour.

Finally, the temperature axis of the 2D grids of sweeps recorded at non-zero current may be corrected for the previously determined offset. After that, magnetic field sweeps at different spin torque currents may be extracted from the corrected 2D grids at the desired temperature (cf. figure 3.13 (d)). The mean temperature shift resulting from the correction is shown in figure 3.14. As expected, the shifts scale quadratically with the applied current due to ohmic heating suggesting a constant cooling power of the system in the small temperature regime in-

vestigated. The temperature correction has been applied to all non-zero current susceptibility data presented in this thesis.

3.2.5. Correction of Magnetoresistance Effects

The temperature correction presented in the previous section was used to determine a single temperature offset for one magnetic field sweep of the susceptibility. However, even though the cryostat temperature and the temperature detected by the sample thermometer may remain constant during a single magnetic field sweep, the deposited heat in the sample may vary as a function of the applied magnetic field due to the changing magnetoresistance of the sample. This effect is not captured by the previously introduced temperature correction. In the following, a correction for this effect is presented, however, the correction turns out to be negligible, and will not be used for the evaluation of the data, presented in this thesis.
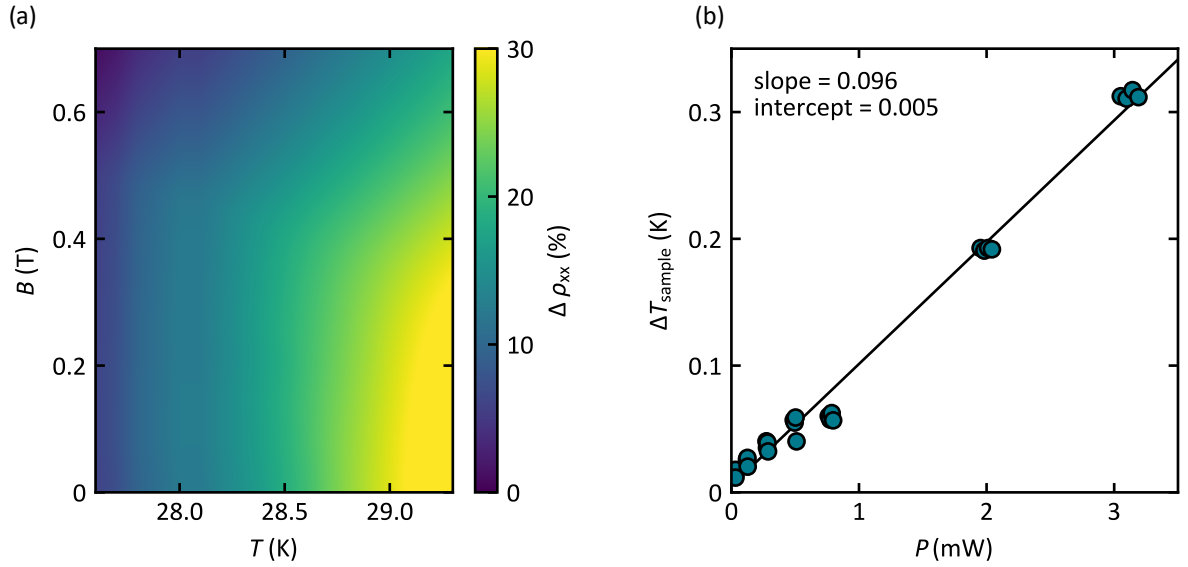
Figure 3.15.: Connection between the shift of the sample temperature T and the deposited heating power P. (a) 2D grid of the change in sample resistivity as a function of applied magnetic field B and sample temperature T. Data taken from reference [155] were used to calculate the grid (b) Sample temperature shift $\Delta T_{\mathrm{sample}}$ as a function of heat, generated by the applied DC current. To calculate the heating power, the sample resistivity was extracted from (a). The parameters of the linear fit may be used to quantify the correction of the change of sample temperature as a result of magnetoresistance effects.

Figures 3.15 and 3.16 summarise the correction for magnetoresistance effects. To estimate the deposited heat, it is necessary to know the resistivity of the sample as a function of temperature and magnetic field. We used data taken from reference [155] to generate a fine 2D grid of the resistivity, shown in figure 3.15 (a). As the major part of the heating effects were corrected in

the previous section, only the change of the sample temperature with respect to a fixed value, at which the temperature correction has already been performed, is determined. To estimate the temperature shift $T_{\mathrm{shift}}(P)$ as a function of ohmic heating power P, generated in the sample, the previously introduced temperature correction is performed for a set of magnetic field sweeps recorded in this thesis. As the sample resistance $\rho_{xx}(T, B)$ as a function of magnetic field and temperature is known, the temperature shift for each curve may be connect to the corresponding deposited heating power. In this way, we obtain a simple linear relation between temperature shift T_{shift} and heating power P. This complicated relation is necessary, as the cooling power of the system, counteracting the ohmic heating, is unknown. The temperature shifts of selected measurements as a function of heating power are shown in figure 3.15 (b). By evaluating all measurement curves the following simple relation is obtained, with specific constants for the cryogenic environment used in this study.

$$T_{\mathrm{shift}}(P) = 0.096 \, \frac{\mathrm{K}}{\mathrm{mW}} \cdot P + 0.005 \, \mathrm{K} \tag{3.12}$$

Here, P is a function of the applied current I and the sample resistivity $\rho_{xx}(B)$:

$$P(I, \rho_{xx}(B)) = I^2 \cdot \rho_{xx}(B). \tag{3.13}$$

Next, we determine a corrected temperature offset $T_{\mathrm{corr}}(B)$ which varies as a function of the magnetic field during a magnetic field sweep. Figure 3.16 (a) shows a colormap of the transverse susceptibility as a function of magnetic field and the additional temperature offset $T_{\mathrm{corr}} - T_0$, where T_0 is the temperature offset, determined by the temperature correction presented in the previous section. The black line indicates the path along which the susceptibility values are extracted from the grid for a magnetic field independent temperature correction. The white dots indicate the alternative path, including the magnetic field dependent offset. We find that the additional temperature correction is of the order of $20 \, \mathrm{mK}$ for the highest measured currents. Figure 3.16 (b) shows both extracted curves, where the turquoise curve only includes the temperature correction independent of the magnetic field, while the purple curve represents the full temperature correction. No significant differences between the two curves are visible in figure 3.16 (b) and hence, figure 3.16 (c) shows the relative deviation of both curves. We find that the maximum difference between both curves for the highest measured currents is in the order of 0.1% to 0.3 %, and therefore negligible for our measurements.

3.2.6. Influence of Oersted Fields

According to Oersted's law, a conductor carrying an electric current generates a magnetic field. Within the conductor, the magnetic field increases linearly as a function of the distance r to the centre of the conductor:
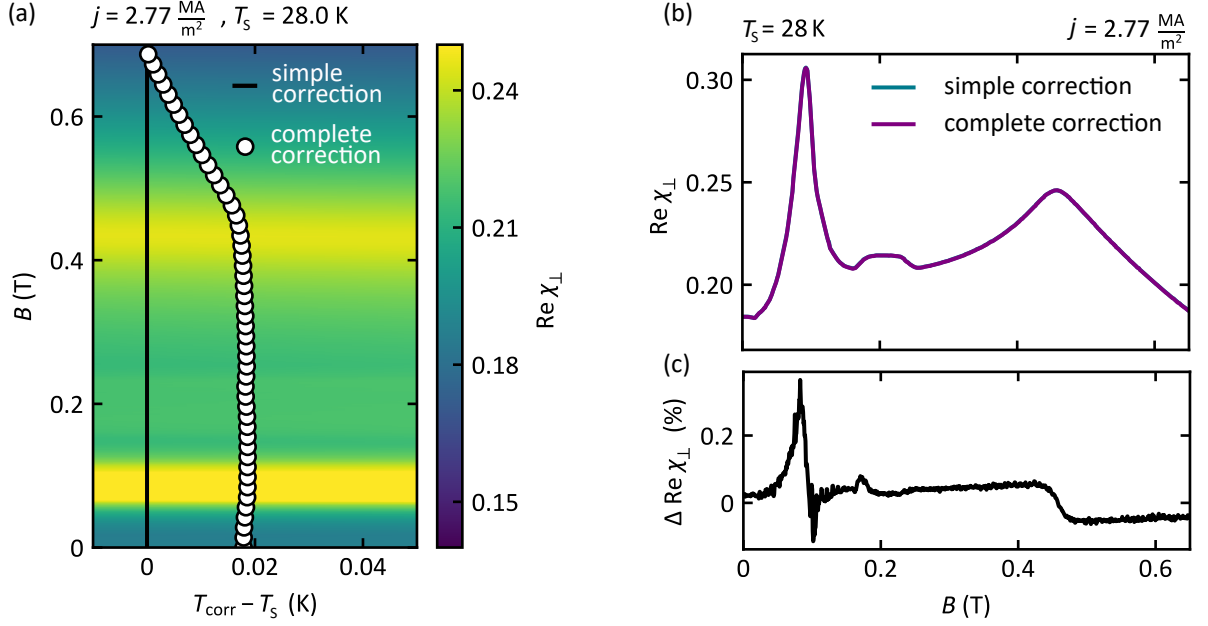
$$B(r) = \mu_0 \cdot j \cdot r. \tag{3.14}$$

Figure 3.16.: Influence of a correction of the sample temperature for magnetoresistive effects on $\chi_\perp$ (a) 2D grid of the real part of the susceptibility, $\mathrm{Re}\,\chi_\perp$ as a function of the magnetic field B. The horizontal axis indicates the difference between the sample temperature determined in this section (complete correction) and the correction described in section 3.2.4 (simple correction). In only the simple correction is applied, the susceptibility $\mathrm{Re}\,\chi_\perp$ is extracted from the grid along the black line. If the complete correction is applied, $\mathrm{Re}\,\chi_\perp$ is extracted along the white dots. (b) Magnetic field sweeps extracted from grid (a) following the black line (simple correction, turquoise curve) and the white dots (final correction, purple line). (c) Difference between the real part of the susceptibility with and without applied magnetoresistance correction. The size of this correction is negligible.

Figure 3.17 (a) shows a schematic drawing of the experimental configuration, indicating the Oersted fields (red circles) in the sample, as well as the current flow direction $\boldsymbol{j}$ and the applied field direction $\boldsymbol{B}$. With the current flowing in y-direction, Oersted fields are generated in the x-z-plane. The absolute value of the Oersted fields, generated in our sample, $|\boldsymbol{B}_{\mathrm{Oe}}|$, is shown over the sample cross section. The strongest Oersted fields at the edges of the sample are $B_{\mathrm{Oe}} < 1.5\,\mathrm{mT}$ for the highest current density of $j = 2.77\,\mathrm{MAm^{-2}}$ applied. This value is very small in comparison to characteristic transition fields in MnSi, which are between $B = 80\,\mathrm{mT}$ and $B = 600\,\mathrm{mT}$. It is important to emphasis that the influence of Oersted fields on the field direction increases, when the applied field is very small. In that case, the Oersted fields cause a strong relative variation of the applied field strength and direction. Figure 3.17 (b) shows the deviation of the effective field $\boldsymbol{B}_{\mathrm{eff}} = \boldsymbol{B} + \boldsymbol{B}_{\mathrm{Oe}}$ from the direction of the applied field $\boldsymbol{B}$, which is points parallel to the vertical z-axis, evaluated for the location in the sample, at which the deviation is largest. This effect is strong in the absence of an applied field, whereas applied fields
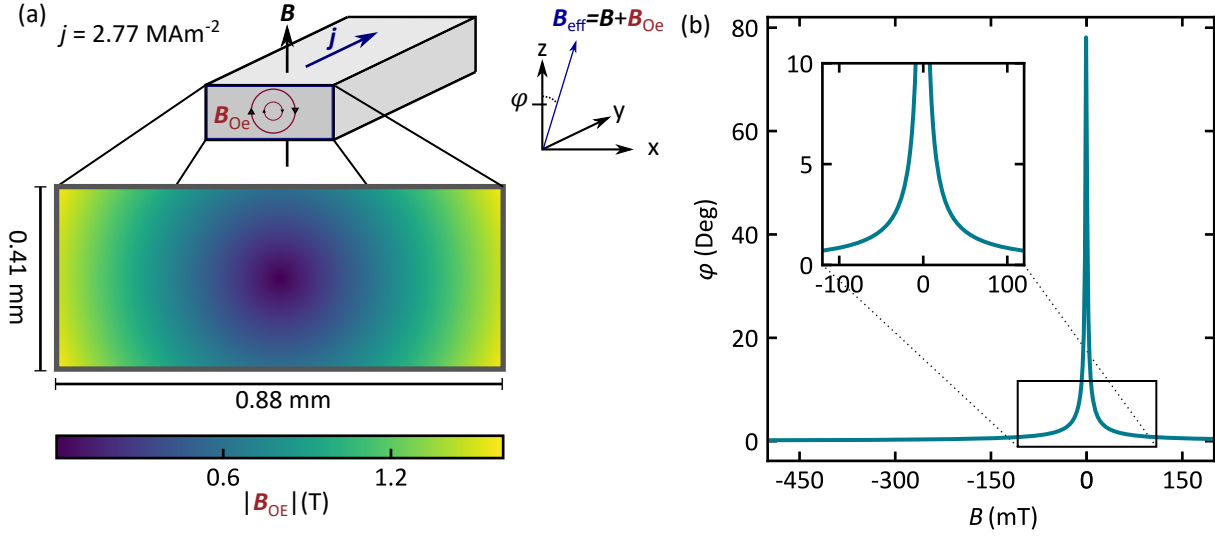
Figure 3.17.: Effects of Oersted fields, B_{Oe}, generated by the DC current flow j in the sample. (a) Cross-sectional depiction of the sample at the maximum current of $j = 2.77 \frac{\mathrm{MA}}{\mathrm{m}^2}$. Oersted fields of up to $B_{\mathrm{Oe}} = 1.6\,\mathrm{mT}$ are generated at the edges of the sample. (b) Resulting effective magnetic field angle φ with respect to the DC field axis as a function of the applied field, B. Inset shows a close up view for small applied fields.

around $50\,\mathrm{mT}$ result in a maximum angle of deviation $\varphi \approx 2°$. This effect may have a significant influence on measurements in zero field. However, the study reported in this thesis focuses on the magnetic properties of the skyrmion lattice, which is stabilised in magnetic fields between $B = 180\,\mathrm{mT}$ and $B = 240\,\mathrm{mT}$. In this regime, the influences of Oersted fields are vanishingly small.

3.3. Experimental Results

In this section, the transverse susceptibility, $\chi_\perp$, of MnSi will be reported as a function of magnetic field and temperature. In the first part, key features of the transverse susceptibility are introduced and compared to the conventional longitudinal susceptibility. This is followed by a discussion of the influence of demagnetisation effects on $\chi_\perp$. Next, the excitation amplitude and frequency dependence of $\chi_\perp$ is reported. A strong influence of both quantities may be observed and two limiting cases are established, which correspond to a collective response of the magnetic structure, and to a response of single spins, respectively. Following that, the interaction of strong spin currents with the skyrmion lattice is investigated. It is shown that the application of a strong DC current results in a translational movement of the skyrmion lattice which can be captured in the transverse susceptibility. This allows to extract the critical current density j_c from the susceptibility measurements. In the last part, the transverse susceptibility is investigated both as a function of the oscillation amplitude, as well as a function of applied DC current. It is shown that an increase of the oscillation amplitude above a threshold amplitude B_{AC}^c results in a reduction of the critical current density j_c by more than one order of magnitude.

3.3.1. Key Features of the Transverse Susceptibility

In order to identify key features of the transverse susceptibility, typical magnetic field sweeps between $B = 0$ and $B = 0.7\,\mathrm{T}$ are recorded and compared to similar sweeps of the well-known longitudinal susceptibility. A comprehensive study of the longitudinal susceptibility is reported in reference [97]. Figures 3.18 (a)-(d) show typical data of the real and imaginary parts of the longitudinal susceptibility of MnSi, $\mathrm{Re}\,\chi_\parallel$ and $\mathrm{Im}\,\chi_\parallel$, at temperatures of $T = 26.5\,\mathrm{K}$ and $T = 28\,\mathrm{K}$. For the measurements of the longitudinal susceptibility, the applied static field $\boldsymbol{B}$ and the oscillating excitation field $\boldsymbol{B}_{AC}$ were aligned along the same axis. A schematic drawing of the field configuration is shown in figure 3.18 (i). The sample was oriented such that both fields pointed parallel to the same crystallographic $\langle 001 \rangle$ axes. All data shown in figures 3.18 were recorded at an excitation field $B_{AC} = 0.6\,\mathrm{mT}$ and an excitation frequency $f_{AC} = 120\,\mathrm{Hz}$. Following initial zero-field cooling, the desired temperature was adjusted, and the magnetic field sweep was performed from $B = 0$ to $B = 0.7\,\mathrm{T}$ at a rate of $20\,\frac{\mathrm{mT}}{\mathrm{s}}$, continuously recording data using a standard lock-in technique (cf. section 1.1.2). Prior to each field sweep, the sample was heated to above the critical temperature to $T \approx 35\,\mathrm{K}$ at zero magnetic field. The data of $\chi_\parallel$ presented in the following are in excellent agreement with the literature (cf. references [81, 97]).

Figure 3.18 (a) depicts $\mathrm{Re}\,\chi_\parallel$ as a function of magnetic field at $T = 26.5\,\mathrm{K}$. $\mathrm{Re}\,\chi_\parallel$ starts at a finite value in zero field and increases monotonically with increasing field, reaching a plateau of constant susceptibility at the helical to conical transition $B_{c1} = 87\,\mathrm{mT}$. This plateau remains relatively constant up to the transition into the field-polarised state at $B_{c2} = 480\,\mathrm{mT}$, where $\mathrm{Re}\,\chi_\parallel$ decreases sharply. The transition field is associated with the point of inflection
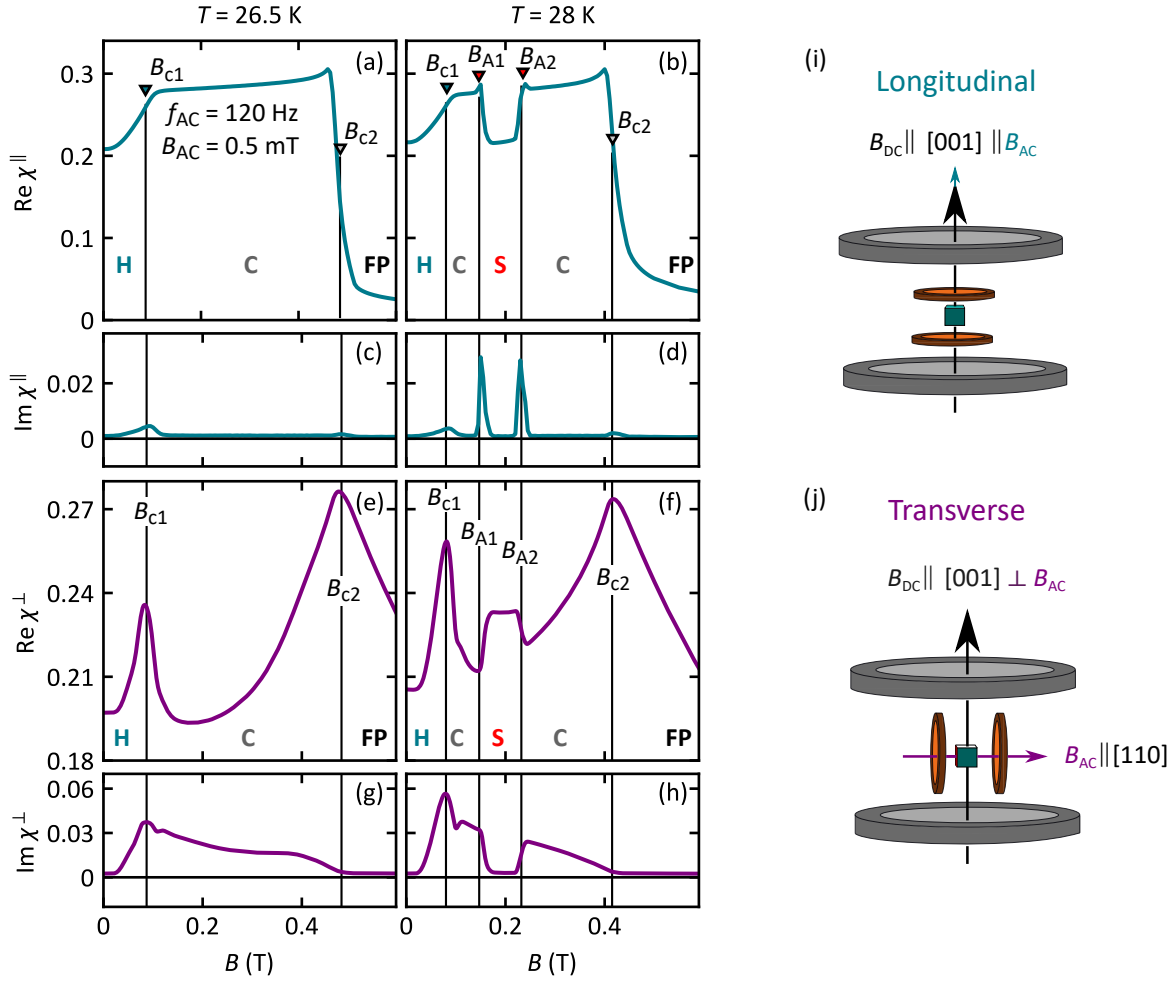
Figure 3.18.: Longitudinal and transverse susceptibilities of MnSi. (a), (b) Real parts of the longitudinal susceptibility $\operatorname{Re}\chi_\parallel$ at $26.5\,\mathrm{K}$ and $28\,\mathrm{K}$ as a function of applied magnetic field B. (c), (d) Imaginary parts $\operatorname{Im}\chi_\parallel$ of the susceptibility as a function of applied magnetic field at $T = 26.5\,\mathrm{K}$ and $T = 28\,\mathrm{K}$. The following transitions are indicated by coloured triangles: helical (H, green) to conical (C, grey) transition at B_{c1}, conical to field polarised (FP, black) transition at B_{c2} and conical to skyrmion lattice phase (S, red) at B_{A1} and at B_{A2}. (e)-(h) Corresponding measurements of the transverse susceptibility $\operatorname{Re}\chi_\perp$ and $\operatorname{Im}\chi_\perp$.(i), (j) Schematic depiction of the field configuration of the longitudinal and the transverse measurement geometries with the crystallographic orientation of the sample.

of $\operatorname{Re}\chi_\parallel$ [97]. At high fields, the susceptibility slowly decreases further. The imaginary part of the susceptibility, $\operatorname{Im}\chi_\parallel$, shown in figure 3.18 (c) is vanishingly small except for the vicinity of the phase transitions at B_{c1} and B_{c2}, where weak maxima are observed. In figure 3.18 (b), the magnetic field dependence of $\operatorname{Re}\chi_\parallel$ is shown at $T = 28\,\mathrm{K}$. Overall, $\operatorname{Re}\chi_\parallel$ displays the same characteristics as data, recorded at $T = 26.5\,\mathrm{K}$. However, the conical plateau displays as additional feature a strongly reduced susceptibility in the field range of the skyrmion lattice phase

between $B_{A1} \approx 147\,\text{mT}$ and $B_{A2} \approx 232\,\text{mT}$. The transitions at B_{A1} and B_{A2} are additionally accompanied by a weak maximum of the susceptibility. The transition field $B_{c2} \approx 415\,\text{mT}$ is shifted to smaller magnetic fields as compared to 26.5 K. Im $\chi_{\parallel}$, shown in figure 3.18 (d), exhibits the same behaviour as for 26.5 K, with additional contributions at B_{A1} and B_{A2}.

In the transverse geometry, the applied static field, $\boldsymbol{B}$, is oriented perpendicular to the excitation field $\boldsymbol{B}_{\text{AC}}$, as depicted in figure 3.18 (j). The sample was mounted such that a crystallographic $\langle 001 \rangle$ axes was parallel to the applied field. The excitation field was oriented along a crystallographic $\langle 110 \rangle$ axes, hence perpendicular to $\boldsymbol{B}$. Note that the applied magnetic field needs be aligned parallel to the same crystallographic direction for both, longitudinal and transverse, susceptibility measurements to reflect the same magnetic state of the sample. As a consequence, in the transverse case the susceptibility is probed along a $\langle 110 \rangle$ direction instead of a $\langle 001 \rangle$ direction. This, however, has no further implications for the results reported in this thesis.

Re $\chi_{\perp}$ and Im $\chi_{\perp}$ are depicted in figures 3.18 (e)-(h). In zero magnetic field Re $\chi_{\parallel}$ and Re $\chi_{\perp}$ are identical. For non-zero magnetic fields, Re $\chi_{\perp}$ shows a quadratic increase up to the critical field B_{c2}, with and additional strong peak at B_{c1}. Above the broad maximum at B_{c2} a linear decrease of the susceptibility towards high magnetic fields is observed. Im $\chi_{\perp}$, depicted in figure 3.18 (g), shows a more complex behaviour as compared to the longitudinal susceptibility. Starting at zero field, Im $\chi_{\perp}$ increases significantly, reaching a maximum value at B_{c1} before decreasing smoothly and reaching zero at the upper critical field B_{c2}. Im $\chi_{\perp}$ remains zero at fields larger than B_{c2}. Figures 3.18 (f) and (h) show the corresponding measurements of Re $\chi_{\perp}$ and Im $\chi_{\perp}$ at $T = 28\,\text{K}$. Again, the shape of the susceptibility curve is equivalent to the data recorded at $T = 26.5\,\text{K}$. However, an additional contribution is observed between B_{A1} and B_{A2} in the regime of the skyrmion lattice phase. Additionally, the peak around B_{c1} increases with increasing temperatures, while the transition field B_{c2} decreases, in agreement with Re $\chi_{\parallel}$. The imaginary part mostly reflects the shape of the data recorded at $T = 26.5\,\text{K}$, with an additional drop to zero between B_{A1} and B_{A2}. Furthermore, the intensity around B_{c1} is increased compared to the 26.5 K measurement.

The comparison between longitudinal and transverse susceptibility measurements shows that both quantities are equally well suited to gain insights into all magnetic phases of MnSi. All phase transitions may be determined easily in the transverse susceptibility and match perfectly well with those inferred from the longitudinal susceptibility. Further, each magnetic phase shows distinct properties in the transverse susceptibility promising complementary information on the magnetic states when combined with the extensively studied longitudinal susceptibility.

In the following, the full magnetic field and temperature dependence of Re $\chi_{\perp}$ and Im $\chi_{\perp}$ over the complete magnetic phase diagram of MnSi is presented. While some important aspects of

the transverse susceptibility have been reported by the author in reference [26], several aspects have not been noticed and will be presented in the following.

Magnetic field sweeps were conducted after zero field cooling, following the procedure described in the previous section, at temperatures between $T = 25\,\mathrm{K}$ and $T = 32\,\mathrm{K}$ in steps of $100\,\mathrm{mK}$. Shown in figures 3.19 (a) and (b) are selected sweeps. All data were combined to generate 2D grids of $\mathrm{Re}\,\chi_\perp$ and $\mathrm{Im}\,\chi_\perp$ as a function of temperature and magnetic field, shown in figures 3.19 (c) and (d).

Following $\mathrm{Re}\,\chi_\perp$ as a function of increasing temperature, shown in figures 3.19 (a) and (c), we find B_{c1} to shift from approximately $90\,\mathrm{mT}$ at the lowest measured temperature to $B_{c1} \approx 60\,\mathrm{mT}$ when approaching the critical temperature $T_c \approx 29\,\mathrm{K}$, in agreement with previous studies. The peak shaped contribution at B_{c1} is associated with the complex reorientation transition from a multi-domain helical state into a single domain conical state reported in reference [105]. It is accompanied by a strong contribution in $\mathrm{Im}\,\chi_\perp$. For magnetic fields $\boldsymbol{H} \parallel \langle 100 \rangle$ this involves two elastic $\mathbb{Z}_2$ Ising transitions. Interestingly, in a similar measurement, presented in reference [26], a more complex behaviour at the helical to conical transition was presented as observed in the measurements reported here. We believe that this discrepancy may be associated with the symmetry breaking, yielding two non-equivalent $\langle 110 \rangle$ directions resulting in different transverse susceptibilities. A more detailed investigation of this transition is beyond the scope of this thesis. Further investigations of the transverse susceptibility, especially investigating two non-equivalent $\langle 110 \rangle$ directions might lead to a more detailed understanding of this transition and consistency with reference [105].

The contribution associated with the skyrmion lattice phase appears at a temperature $T_{A2} = 26.9\,\mathrm{K}$ and is seen up to the critical temperature T_c. While the skyrmion lattice phase ranges from $B_{A1} \approx 117\,\mathrm{mT}$ to $B_{A2} \approx 232\,\mathrm{mT}$ at the highest temperatures, the extent of the signature shrinks with decreasing temperatures down to a minimum, before vanishing completely below T_{A2}. Except for its fringes, the contribution of the skyrmion lattice phase is constant over the whole range of the skyrmion lattice phase both as a function of temperature and field. The lack of contributions to $\mathrm{Im}\,\chi_\perp$, shown in figures 3.19 (b) and (d), as well as to $\mathrm{Im}\,\chi_\parallel$ indicate the absence of dissipative processes in the skyrmion lattice phase caused by the excitation field, regardless of measurement configuration.

For $T > 28.7\,\mathrm{K}$, the magnetic field dependence of the susceptibility changes and exhibits signatures of the helical transition and the skyrmion lattice phase up to temperatures above $T = 29\,\mathrm{K}$. This region is associated with the fluctuation-disordered regime, extensively discussed in reference [103], and persists up to $T = 32\,\mathrm{K}$, above which paramagnetic behaviour is observed. The signatures of the skyrmion lattice phase above T_c support the idea of skyrmion-like, topologi-
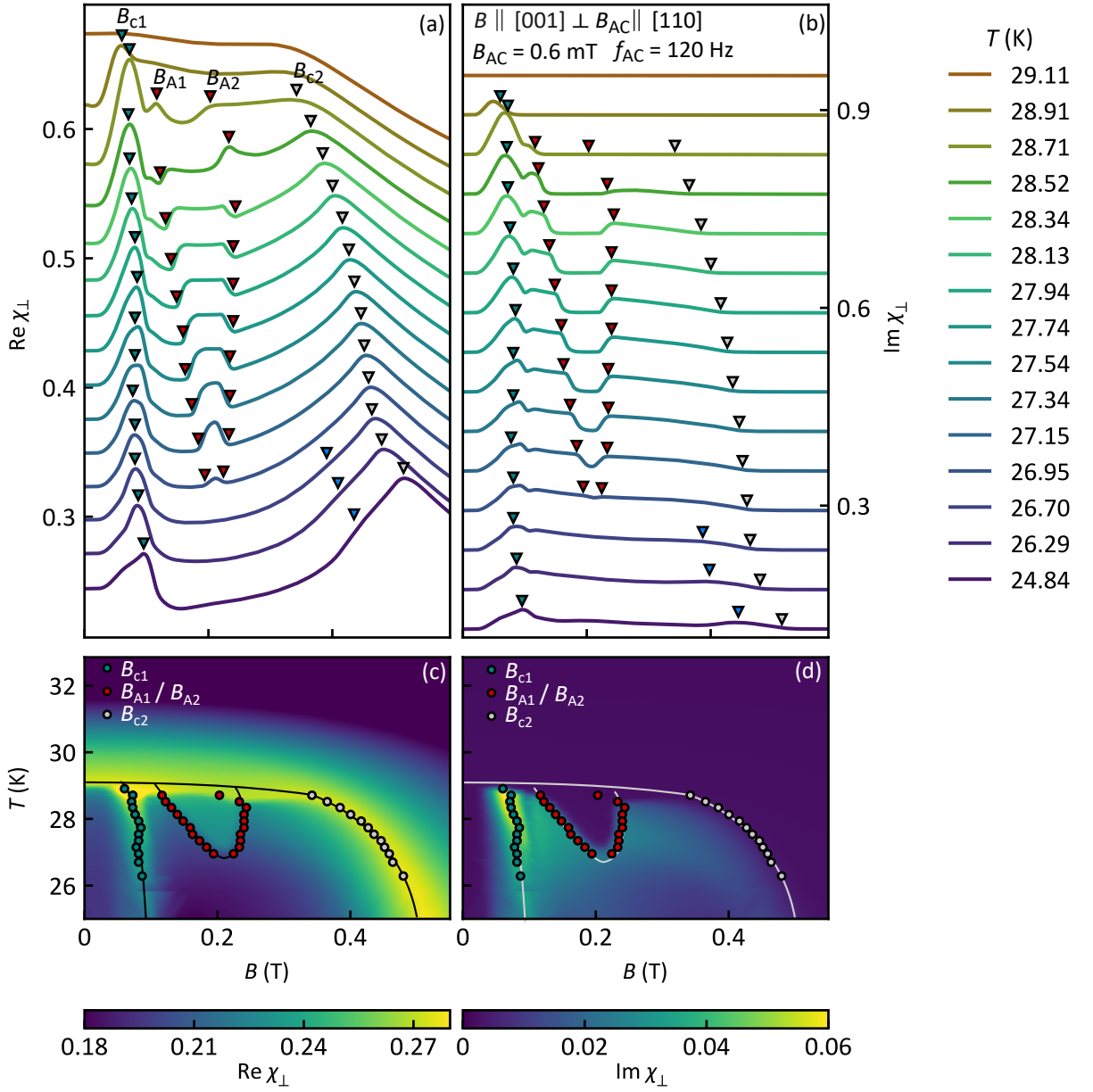
Figure 3.19.: Magnetic field and temperature dependence of the transverse susceptibility of MnSi at a small excitation amplitude and frequency of $B_{AC} = 0.6 \, \text{mT}$ and $f_{AC} = 120 \, \text{Hz}$, respectively. (a), (b) Selected magnetic field sweeps of the real and imaginary parts of the transverse susceptibility at different temperatures. Phase transitions are indicated by coloured triangles (cf. figure 3.18). The curves are shifted by a small offset. (c), (d) 2D representation of $\text{Re} \, \chi_\perp$ and $\text{Im} \, \chi_\perp$ as function of temperature and field generated from the magnetic field sweeps. The phase transition lines are very well visible and additionally indicated by coloured dots, extracted from figures (a) and (b). Curves serve to guide the eye.

cally non-trivial fluctuations, believed to be present in this regime [105]. The intensity of the susceptibility along the B_{c2} transition line remains constant over the entire phase diagram and shifts towards lower field values before vanishing above T_c.

The susceptibility in the conical phase shows a quadratic dependence over the entire temperature and magnetic field region investigated, as discussed above. This shape will be discussed in more detail in the context of frequency and amplitude dependence of the transverse susceptibility in the following section. A weak additional contribution to the parabolic shape of the susceptibility in the conical phase may be observed at temperatures below $T = 26.7\,\mathrm{K}$, indicated by blue triangles in figures 3.19 (a) and (b). The origin of this contribution is presently unclear and requires further studies, planned for the future.

3.3.2. Discussion of Demagnetisation Effects

The data presented above were recorded on a cubic sample (cf. sample B, section 3.2.1) with an edge length of $2\,\mathrm{mm}$. This allows to maximise the filling factor of the susceptometer and thus the signal of the susceptometer. The sample shape and orientation is shown in figure 3.20 (a). As a result of the very high current densities of up to $2.5\,\frac{\mathrm{MA}}{\mathrm{m}^2}$, required to conduct spin torque experiments, it is necessary to adjust the sample shape to minimise the amount of ohmic heating during the experiments. Accordingly, a sample with a reduced cross-section of $0.41\,\mathrm{mm}$ x $0.88\,\mathrm{mm}$ was prepared. In order to keep a reasonably high signal contribution by the sample, the length of the sample was chosen such that it matches the length of the pick-up coil. All sample dimensions and the sample orientation are schematically depicted in figure 3.20 (b), whereas general aspects concerning the sample may be found in section 3.2.1 (cf. sample C). A generic set of data for each sample is shown in figures 3.20 (c) and (d). Even though both measurements have been recorded using identical parameters, the different sample dimensions result in a change of demagnetisation fields. A detailed discussion of the influence of a complete demagnetisation corrections may be found in reference [80]. Here, a short account for the influence of demagnetisation effects is given for the measurement data, presented in this study.

First, overall the susceptibility of sample C is reduced as compared to the cubic sample B, as the excitation field of the susceptometer is subject to a demagnetization correction, which is more pronounced for sample shape C and results in a reduced susceptibility. This effect has been investigated carefully for the longitudinal susceptibility in MnSi. The discussion provided in reference [80] applies also to the transverse susceptibility. The resulting shift of the absolute value of $\chi_\perp$ does not affect the considerations presented in the following. Second, all phase transitions are shifted towards larger magnetic fields. This effect may be corrected by a straight forward demagnetisation correction following reference [80]. Additionally to the shift, the phase boundaries smear out as a result of the inhomogeneous field distribution inside the sample. Fi-
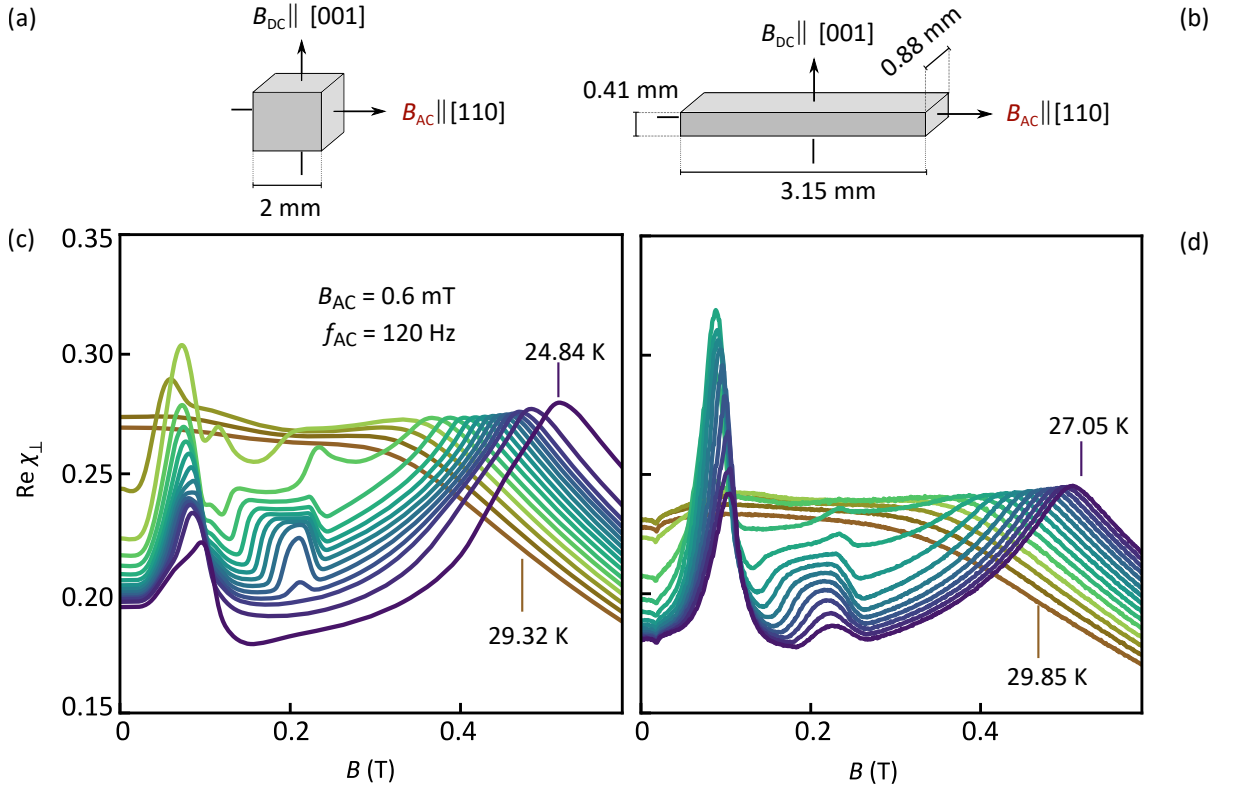
Figure 3.20.: Transverse susceptibility $\mathrm{Re}\,\chi_\perp$ as a function of applied magnetic field B for two different sample shapes. (a), (b) Schematic depiction of the two different samples as well as their orientations and dimensions. (c) Data recorded on a cubic sample of $2\,\mathrm{mm}$ edge length. (d) Data recorded on a flat cuboid, which minimises the ohmic heating during spin torque experiments. The difference of both measurements in (c) and (d) is a result of demagnetisation effects.

nally, the peak around the transition field B_{c1} is enhanced in the flat sample. Following the considerations of reference [105], this may be the result of domain re-population at the transition from a multi-domain helical state to a single-domain conical state.

The influence of all effects mentioned above is mostly restricted to the phase boundaries and is in general well understood. As the aim of the work presented in this thesis is the investigation of spin torque effects in the skyrmion lattice phase, most of these effects will not affect on our conclusions. An exception may be the broadening of the phase boundaries of the skyrmion lattice phase. However, performing the spin torque experiments in the centre of the skyrmion lattice phase, makes a strong influence of the demagnetisation effects unlikely.

3.3.3. Excitation Amplitude and Frequency Dependence of $\chi_\perp$

To investigate the dependence of the critical current j_c on an oscillating magnetic field, a detailed knowledge of the dynamics of the skyrmion lattice, without spin torque currents present, is essential. Therefore, changes of the transverse susceptibility of MnSi under variations of the excitation amplitude B_{AC} and the excitation frequency f_{AC} are reported in the following section.
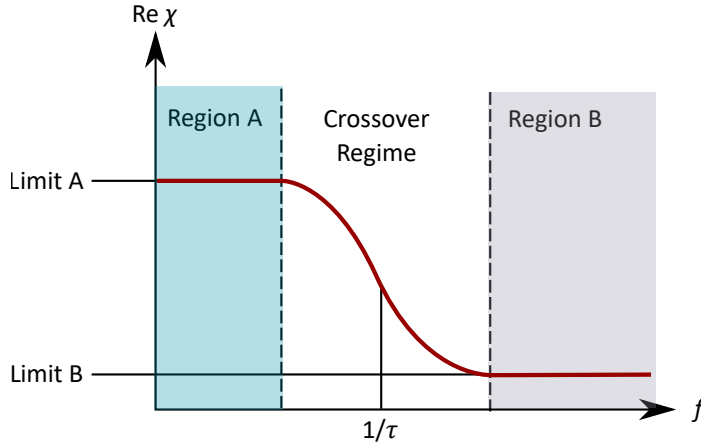

Figure 3.21.: Schematic depiction of $\mathrm{Re}\,\chi_\perp$ as a function of excitation frequency f_{AC} of an applied oscillating field. The susceptibility exhibits two limits. Limit A describes a region, in which the entire magnetic structure can follow the oscillating applied field and limit B a region, in which the response is generated by the excitation of single spins within the magnetic structure. Both regimes are connected by a broad crossover regime, in which a combination of both effects may be observed. The crossover regime is characterised by a typical relaxation time τ.

In the magnetic phases of MnSi, one may expect two limiting cases of the frequency dependence of the susceptibility. First, for small excitation frequencies, a regime in which the entire magnetic structure is able to respond to an external field variation. This is, e.g. the conical pitch direction changes with the oscillating field, while the conical helix itself retains its structure. In general, this region is expected to exhibit a large response in a susceptibility measurement as depicted in figure 3.21. Here, region A denotes the limit of low frequencies, in which the entire magnetic structure is tilted by the applied oscillating field. Region B, in contrast, represents the limit, in which the frequency of the applied field oscillation is too large for the entire magnetic structure to follow, resulting in a response of single spins within the magnetic structure. This leads to a reduced susceptibility as compared to region A. Both regions are connected by a smooth crossover regime which is characterised by the typical relaxation times of the magnetic

structure, τ. In the following, this simple phenomenological picture will be investigated by transverse susceptibility measurements. Additionally, the influence of the excitation amplitude B_{AC} on the transverse susceptibility in both limits will be determined.

In comparison to the data presented above, the magnetic field sweeps in this paragraph were performed using a field-cooled protocol as follows. First, the desired temperature between $T = 27\,\mathrm{K}$ and $T = 28.5\,\mathrm{K}$ was stabilised and the excitation amplitude and frequency were set. Next, data were recorded in a magnetic field sweep from $B = 0$ to $B = 0.7\,\mathrm{T}$. Following this, the field was reduced to zero without heating the sample above its transition temperature and the temperature was changed to the value of the next scan. This way, time consuming zero-field measurements could be avoided speeding the measurements up to allow for the variation of two additional parameters, the excitation amplitude B_{AC} and frequency f_{AC}. Previous studies and several dedicated test measurements did not show any discrepancies between the chosen field-cooled protocol and zero-field cooled measurements in the given configurations.
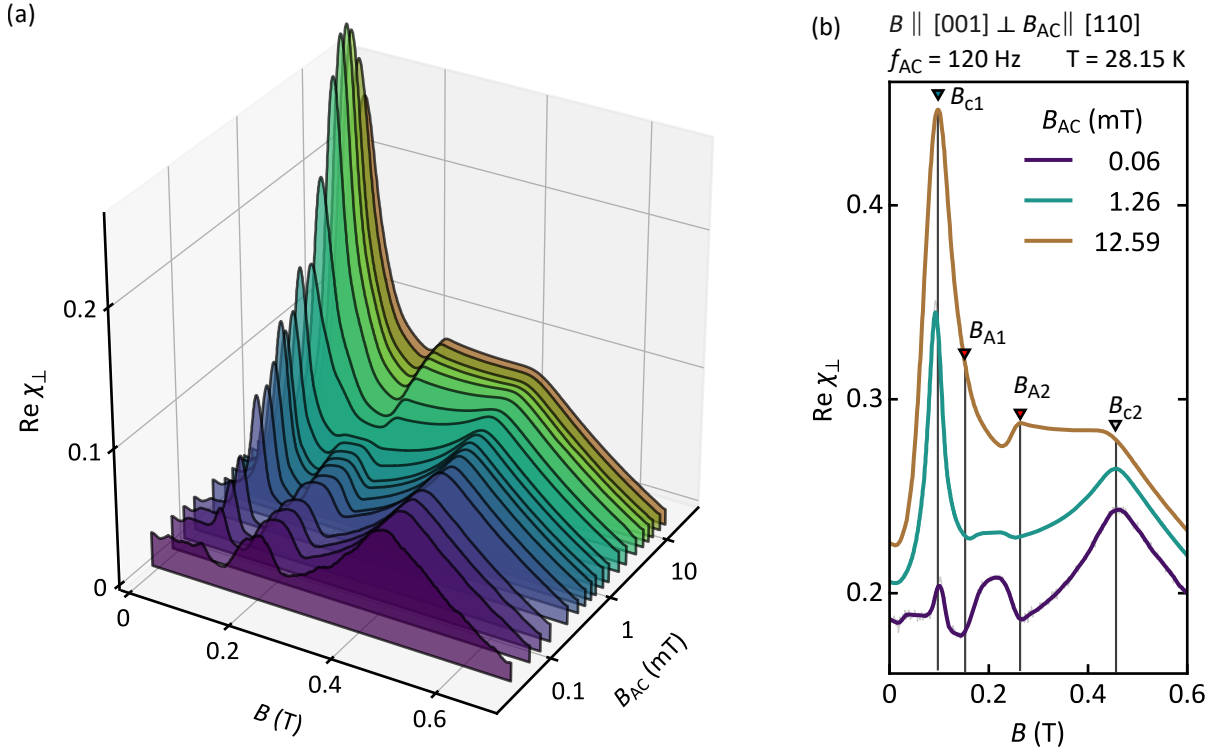
Figure 3.22.: Real part of the transverse susceptibility $\mathrm{Re}\,\chi_\perp$ for selected excitation amplitudes. (a) Magnetic field sweeps taken at a temperature of $T = 28.15\,\mathrm{K}$ for excitation amplitudes between $B_{AC} = 0.06\,\mathrm{mT}$ and $B_{AC} = 12.59\,\mathrm{mT}$ and a fixed frequency of $f_{AC} = 120\,\mathrm{Hz}$. (b) Selected magnetic field sweeps at three selected excitation fields. Phase transitions are indicated by coloured triangles following the description of figure 3.18. Curves have been shifted by a constant value for clarity.
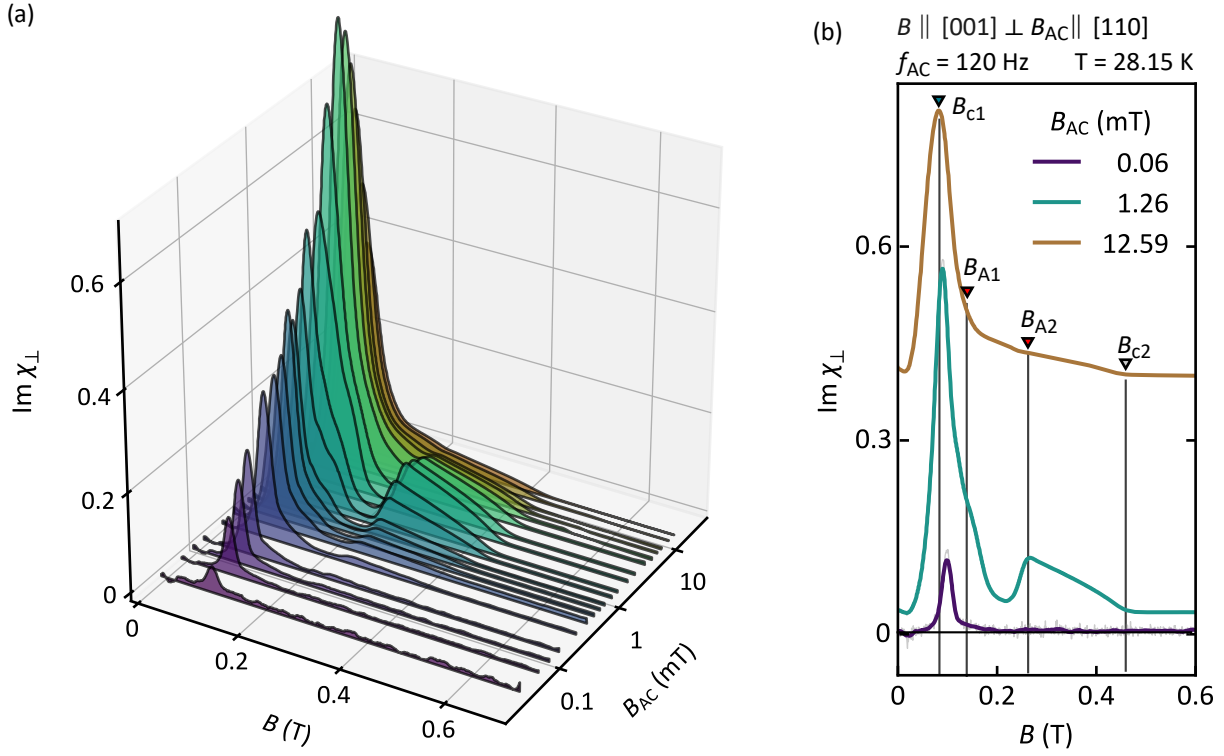
(a)

(b)

$B \parallel [001] \perp B_{AC} \parallel [110]$
$f_{AC} = 120\,\text{Hz}$ $T = 28.15\,\text{K}$

Figure 3.23.: Imaginary part of the transverse susceptibility $\text{Im}\,\chi_\perp$ for selected excitation amplitudes. (a) Magnetic field sweeps taken at a temperature of $T = 28.15\,\text{K}$ for excitation amplitudes between $B_{AC} = 0.06\,\text{mT}$ and $B_{AC} = 12.59\,\text{mT}$ and a fixed frequency of $f_{AC} = 120\,\text{Hz}$. (b) Selected magnetic field sweeps at three selected excitation fields. Phase transitions are indicated by coloured triangles following the description of figure 3.18. Curves have been shifted for a better visualisation.

Figures 3.22 and 3.23 show $\text{Re}\,\chi_\perp$ and $\text{Im}\,\chi_\perp$ as a function of magnetic field B for different excitation amplitudes B_{AC} at $f_{AC} = 120\,\text{Hz}$. Figure 3.22 (a) shows the magnetic field dependence at a temperature $T = 28.15\,\text{K}$ for excitation amplitudes between $B_{AC} = 0.06\,\text{mT}$ and $B_{AC} = 12.9\,\text{mT}$. Three selected curves, taken from figure 3.22 (a), are depicted in figure 3.22 (b). Data are shifted by a small offset for better visibility. At the smallest amplitude, the generic behaviour that has been discussed throughout the previous paragraphs is reproduced. Beginning with the transition peak at B_{c1}, the peak increases strongly as a function of increasing excitation amplitude and reaches a maximum at $B_{AC} \approx 8\,\text{mT}$. This suggests a strong response of the system at the B_{c1} transition. At small magnetic fields and small excitation amplitudes, $\text{Re}\,\chi_\perp$ exhibits some additional structure, which might be connected to the complex transition from the helical to the conical phase. This contribution, however, is only present up to amplitudes of about $B_{AC} = 0.5\,\text{mT}$, above which the contribution at B_{c1} dominates. At the same time, the imaginary part, $\text{Im}\,\chi_\perp$, shown in figures 3.23 (a) and (b), is dominated by the peak around B_{c1}. The size of the peak follows the functional dependence of the real part, with a maximum

at $B_{AC} \approx 8\,\mathrm{mT}$. Note that the maximum value of the peak exceeds the corresponding value of $\mathrm{Re}\,\chi_\perp$ by a factor of two. This indicates strong dissipative behaviour, possibly due to domain re-population or dynamical inelastic properties.

The plateau at intermediate fields, attributed to the skyrmion lattice phase, remains constant for low excitation amplitudes. Above $B_{AC} \approx 1\,\mathrm{mT}$, it increases gently and transforms from a symmetrical contribution between B_{A1} and B_{A2} at low amplitudes (cf. figure 3.22 (b), purple and green curves)), to an asymmetrical shape (cf. figure 3.22 (b), brown curve)), caused by the overlap of the strong B_{c1} peak. Interestingly, the imaginary part, shown in figures 3.23 (a) and (b), does not show any significant contribution in the skyrmion lattice phase.

Even though the susceptibility in the skyrmion lattice phase remains constant, the generic shape of $\mathrm{Re}\,\chi_\perp$ changes significantly as a function of the excitation amplitude. This may be attributed to the contribution of the conical phase, where the observed quadratic dependence on the external field for low excitation amplitudes evolves into a plateau at high excitation amplitudes. Around the transition between both limits, $\mathrm{Im}\,\chi_\perp$ increase to a maximum value for excitations $B_{AC} \approx 3\,\mathrm{mT}$, whereas no contribution is visible for very low excitation amplitudes and only small contributions for very high excitation amplitudes (cf. figure 3.23 (b), green curve).

As expected, the B_{c2} transition as well as the field-polarised region are unaffected by a change of excitation frequency. This was an important assumption of the temperature correction, presented in section 3.2.4. $\mathrm{Im}\,\chi_\perp$ is vanishingly small at all fields except for B_{c1} and the conical phase, which has already been discussed previously.

Figures 3.24 and 3.25 show typical data of $\chi_\perp$ as a function of magnetic field B for different excitation frequencies between $f_{AC} = 20\,\mathrm{Hz}$ and $f_{AC} = 2\,\mathrm{kHz}$. Data were recorded at a temperature $T = 28.15\,\mathrm{K}$ and an excitation amplitude of $B_{AC} = 2.52\,\mathrm{mT}$. The magnetic field dependence, which was discussed in the previous sections, may be found for curves measured at high excitation frequencies above $1\,\mathrm{kHz}$ (cf. 3.24 (b), purple curve). The amplitude of the peak at B_{c1} decreases strongly as a function of frequency and nearly vanishes at the highest measured frequency of $f_{AC} = 2\,\mathrm{kHz}$. Measurements in the intermediate frequency range between $f_{AC} = 80\,\mathrm{Hz}$ and $f_{AC} = 250\,\mathrm{Hz}$, show a second maximum close to the B_{c1} transition which may be present down to lowest frequencies, however hidden in the presence of the main peak at B_{c1}. This maximum is indicated in figure 3.24 (b) as B_{c1}^* at $f_{AC} = 180\,\mathrm{Hz}$ (green curve). The imaginary part, shown in figure 3.25, exhibits a similar behaviour around B_{c1}, including the presence of a second transition at B_{c1}^* over a wide range of frequencies. Again, the magnitude of the peak in the imaginary part exceeds the real part quantitatively by over 200%. The strong increase of the peak at B_{c1} for low frequencies in real and imaginary parts of the transverse susceptibility suggest slow relaxation dynamics at the B_{c1} transition and the observation of the
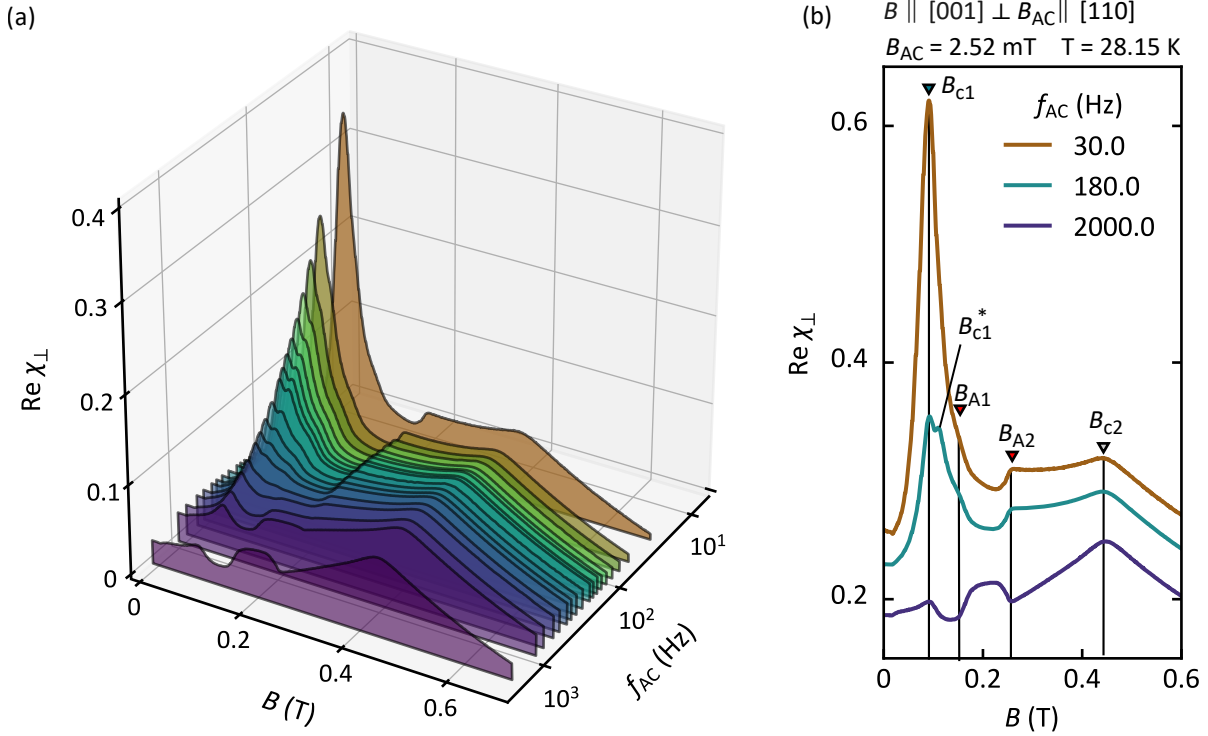
(a)

(b)

Figure 3.24.: Real part of the transverse susceptibility $\text{Re}\,\chi_\perp$ for selected excitation frequencies. (a) Magnetic field sweeps taken at a temperature of $T = 28.15\,\text{K}$ for excitation frequencies between $f_{AC} = 20\,\text{Hz}$ and $f_{AC} = 2000\,\text{Hz}$ and a fixed excitation amplitude of $B_{AC} = 2.52\,\text{mT}$. (b) Selected magnetic field sweeps at three selected excitation frequencies. Phase transitions are indicated by coloured triangles following the description of figure 3.18. Curves have been shifted by a constant value for clarity.

second maximum is related to the two Ising transitions associated with the helix pitch orientation at B_{c1}, as already commented in the previous section and discussed in reference [105].

Similar to the effect of changing the excitation amplitude, the signal strength in the skyrmion lattice phase appears to be essentially constant over the entire range of frequencies, with a finite value of about 0.2 in the real part of $\chi_\perp$ and a vanishing imaginary contribution (cf. figures 3.24 and 3.25). No influence of the excitation frequency on the B_{c2} transition and on the shape of $\text{Re}\,\chi_\perp$ in the field polarised state may be observed. $\text{Im}\,\chi_\perp$, however, shows strong indications for an additional contribution by eddy currents, generated in the sample by the excitation field. As this contribution may clearly be distinguished from the data of interest, a frequency-dependent offset was subtracted in the data set shown here. The uncorrected data may be found in appendix A. In the conical phase, the quadratic field dependence of $\text{Re}\,\chi_\perp$ is reproduced in the high frequency limit consistent with the data shown above. This shape changes gradually to a plateau of constant susceptibility, when the excitation frequency is reduced, similar to $\text{Re}\,\chi_\perp$ at
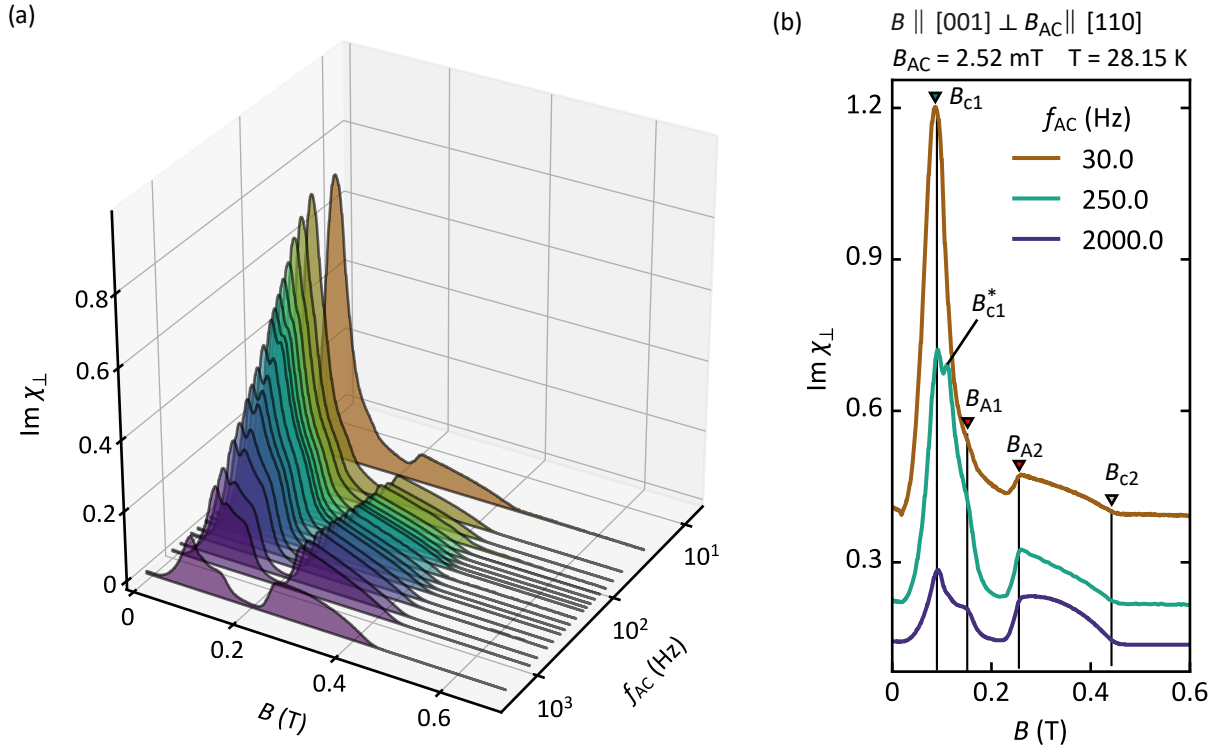
Figure 3.25.: Imaginary part of the transverse susceptibility Im $\chi_\perp$ for different excitation frequencies. (a) Magnetic field sweeps taken at a temperature of $T = 28.15$ K for excitation frequencies between $f_{AC} = 20$ Hz and $f_{AC} = 2000$ Hz and a fixed excitation amplitude of $B_{AC} = 2.52$ mT. (b) Selected magnetic field sweeps at three selected excitation frequencies. Phase transitions are indicated by coloured triangles following the description of figure 3.18. Curves have been shifted for a better visualisation.

high excitation amplitudes.

The data reported above exhibit two distinct limits of the susceptibility as a function of excitation frequency and amplitude. The first limit, region A, may be observed in measurements at low excitation frequencies, as shown in figure 3.24 (b) (brown curve). Here, the conical phase is characterised by a plateau of nearly constant susceptibility and the data exhibit a strong peak at B_{c1}. In the second limit, region B, the susceptibility shows a quadratic field dependence in the conical phase and only a vanishingly small contribution at B_{c1}. In the field polarised region, the susceptibility remains unchanged under a variation of excitation amplitude and frequency. The change of the peak intensity at B_{c1} may be interpreted as a result of slow domain re-population at this transition, and is not discussed further in this study. A detailed discussion may be found in reference [105].

In the conical phase, region A and B may be interpreted, following the considerations at the

beginning of this chapter, as a response of the entire magnetic structure and as the response of single spins to the oscillating field, respectively. In region A, the magnetisation vector $\boldsymbol{M}$ follows the oscillating applied field direction and the transverse susceptibility may be approximated by

$$\mathrm{Re}\,\chi_\perp \approx \frac{M}{H}, \tag{3.15}$$

where M is the magnetisation and H the applied magnetic field. The linear field dependence of the magnetisation in the conical phase then suggests a constant plateau of $\mathrm{Re}\,\chi_\perp$ in region A. This is may be observed in figure 3.26, where a selected field sweep of $\mathrm{Re}\,\chi_\perp$ is shown for $f_\mathrm{AC} = 20\,\mathrm{Hz}$ and $B_\mathrm{AC} = 12.59\,\mathrm{mT}$ together with a measurement of $\frac{M}{H}$, collected in a *Quantum Design* PPMS in reference [97]. Note that the magnetisation data had to be scaled by a factor of 1.13 to fit our data due to different demagnetisation factors of the samples. This shape of the susceptibility, however, vanishes as the excitation frequency is increased. Then, in region B, the conical helix is no longer able to follow the oscillating field direction and we suspect that the susceptibility signal is caused by the response of single spins. As a result, a quadratic dependence of the transverse susceptibility as a function of applied magnetic field is observed in the conical phase, as may be seen in figures 3.22-3.25.
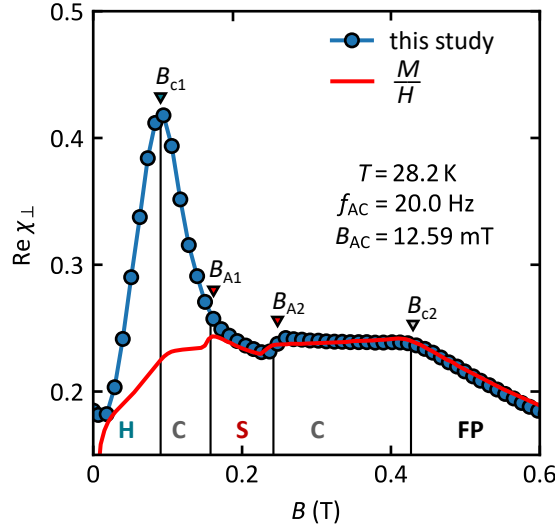
Figure 3.26.: Comparison between real part of the transverse susceptibility, as inferred in this study, and the susceptibility, approximated by $\mathrm{Re}\,\chi_\perp \approx \frac{M}{H}$. In field-polarised state, conical phase and skyrmion lattice phase, both curves overlap remarkably well. At this excitation frequency and amplitude, the entire magnetic structure is able to follow the applied field oscillation, yielding $\mathrm{Re}\,\chi \approx \frac{M}{H}$. The strongly frequency-dependent peak at B_{c1} may not be captured by this approximation.

In the skyrmion lattice phase, similar arguments may be used to describe the frequency dependence of the transverse susceptibility. Here, regions A and B are not clearly distinguishable

by eye in figures 3.22 - 3.25, however, a detailed evaluation shows that the transverse susceptibility in the skyrmion lattice phase decreases slightly as a function of excitation frequency, similar to the behaviour observed in the conical phase. As shown in figure 3.26, the skyrmion lattice phase may be equally approximated by $\mathrm{Re}\,\chi_\perp \approx \frac{M}{H}$, suggesting that the magnetisation direction is able to follow the oscillating magnetic field, similar to the considerations for the conical phase. In region B, the reduced susceptibility in the skyrmion lattice phase at high excitation frequencies, as observed above, suggests a similar behaviour as presented previously for region B of the conical phase. Details of the excitation frequency and amplitude dependence will be discussed further in section 3.3.5 in the context of spin-transfer torques in the skyrmion lattice phase.
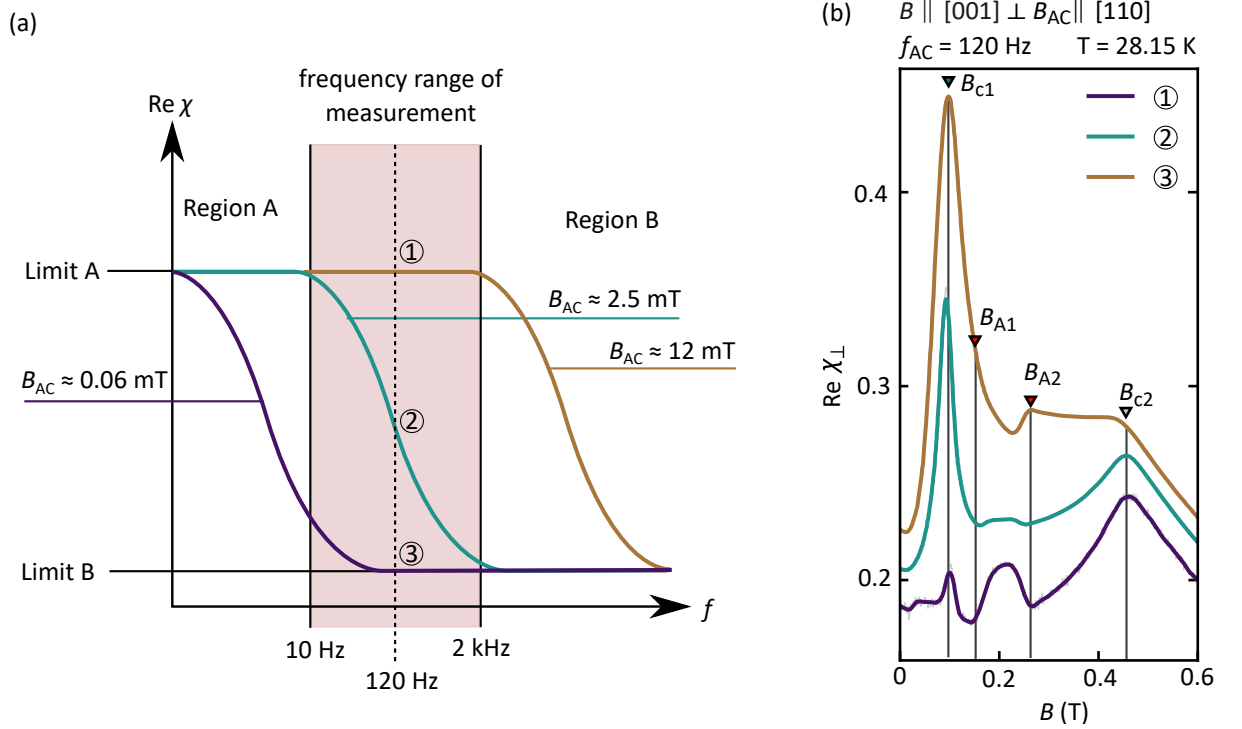
Figure 3.27.: Influence of excitation amplitude B_{AC} and excitation frequency f_{AC} on $\mathrm{Re}\,\chi_\perp$. (a) Schematic depiction of the frequency dependence of $\mathrm{Re}\,\chi_\perp$ for different excitation amplitudes. The curve, described in figure 3.21 is shifted along the horizontal frequency axis for different excitation amplitudes. (b) Measurements of $\mathrm{Re}\,\chi_\perp$ as a function of applied magnetic field for different excitation amplitudes. It may be seen that an increase of the excitation frequency from (1) to (3) results in a change of the generic shape of $\mathrm{Re}\,\chi_\perp$, indicating a transition from limit A to limit B. Curves are shifted by a constant offset for better visibility.

So-far, the considerations were restricted to the influence of the excitation frequency on $\chi_\perp$. The influence of the excitation amplitude on $\chi_\perp$ in the conical phase and the skyrmion lattice phase is summarised schematically in figure 3.27. Here, the green curve has already been in-

troduced at the beginning of this section in figure 3.21. It represents the generic dependence of $\mathrm{Re}\,\chi_\perp$ on the excitation frequency f_{AC}. If the excitation amplitude is increased, this curve is shifted towards higher frequencies (brown curve), while it is shifted towards lower frequencies for small excitation amplitudes (purple curve). This leads to an enhancement of region A for large excitation amplitude and an enhancement of region B for small amplitudes. This behaviour may be clearly observed in figure 3.22. Here, measurements of the susceptibility are presented at an excitation frequency $f_{\mathrm{AC}} = 120\,\mathrm{Hz}$. For better visualisation, figure 3.22 (b) is repeated in figure 3.27 (b). The measurement frequency of this measurement, $f_{\mathrm{AC}} = 120\,\mathrm{Hz}$ is denoted in figure 3.27 by a dashed line. For large excitation amplitudes, (1), the system remains in state A even at a frequency of $120\,\mathrm{Hz}$. When the amplitude is reduced, the response of the system gradually changes from region A to region B, (2). For the smallest excitation amplitudes, (3), the system has already changed to region B at $f_{\mathrm{AC}} = 120\,\mathrm{Hz}$ and limit B is observed.

3.3.4. Spin-Transfer Torques in the Skyrmion Lattice Phase of MnSi

The skyrmion lattice phase of MnSi is known to exhibit spin torque effects above a critical current density of $j_c \approx 0.7\,\mathrm{MAm^{-2}}$ [16]. In the following, evidence for j_c in the transverse susceptibility is reported. Therefore, measurements of the transverse susceptibility were conducted at various current densities between $j = 0$ and $j = 2.5\,\mathrm{MAm^{-2}}$. To take into account the effects of ohmic heating, a complex temperature correction was performed for all spin torque measurements as presented in section 3.2.4. The corrected results are shown in figures 3.28 (a) and (b) with a detailed investigation of the skyrmion lattice phase in figures 3.28 (c) and (d).

Figures 3.28 (a) and (b) show the real and the imaginary parts of the transverse susceptibility, $\mathrm{Re}\,\chi_\perp$ and $\mathrm{Im}\,\chi_\perp$, as a function of the applied magnetic field B at $T = 28.1\,\mathrm{K}$, an excitation frequency $f_{\mathrm{AC}} = 120\,\mathrm{Hz}$, and an excitation amplitude $B_{\mathrm{AC}} = 1.26\,\mathrm{mT}$. The magnetic field dependence was determined between $B = 0$ and $B = 0.7\,\mathrm{T}$ as described in section 3.3.3. The transition fields are denoted by triangles where the green triangle marks the transition from the helical to the conical phase at B_{c1}, the red triangles mark the transition fields B_{A1} and B_{A2} of the skyrmion lattice phase, and the grey triangle indicates the onset of the field-polarised state at B_{c2}. In agreement with the discussion presented above, a plateau-like contribution to $\mathrm{Re}\,\chi_\perp$ my be observed in the data, associated with the skyrmion lattice phase (S), between B_{A1} and B_{A2} for zero applied current (purple curve).

Next, magnetic field sweeps were performed at a set of different current densities, applied along a crystallographic $\langle 110 \rangle$ direction. With the applied magnetic field B oriented along $\langle 001 \rangle$, the current density was applied perpendicular to the applied field direction and parallel to the oscillating probing field B_{AC}. This measurement configuration has already been discussed in section 1.2.5 and in figures 3.10 (b) and (c) and is depicted schematically in figure 3.28 (a).
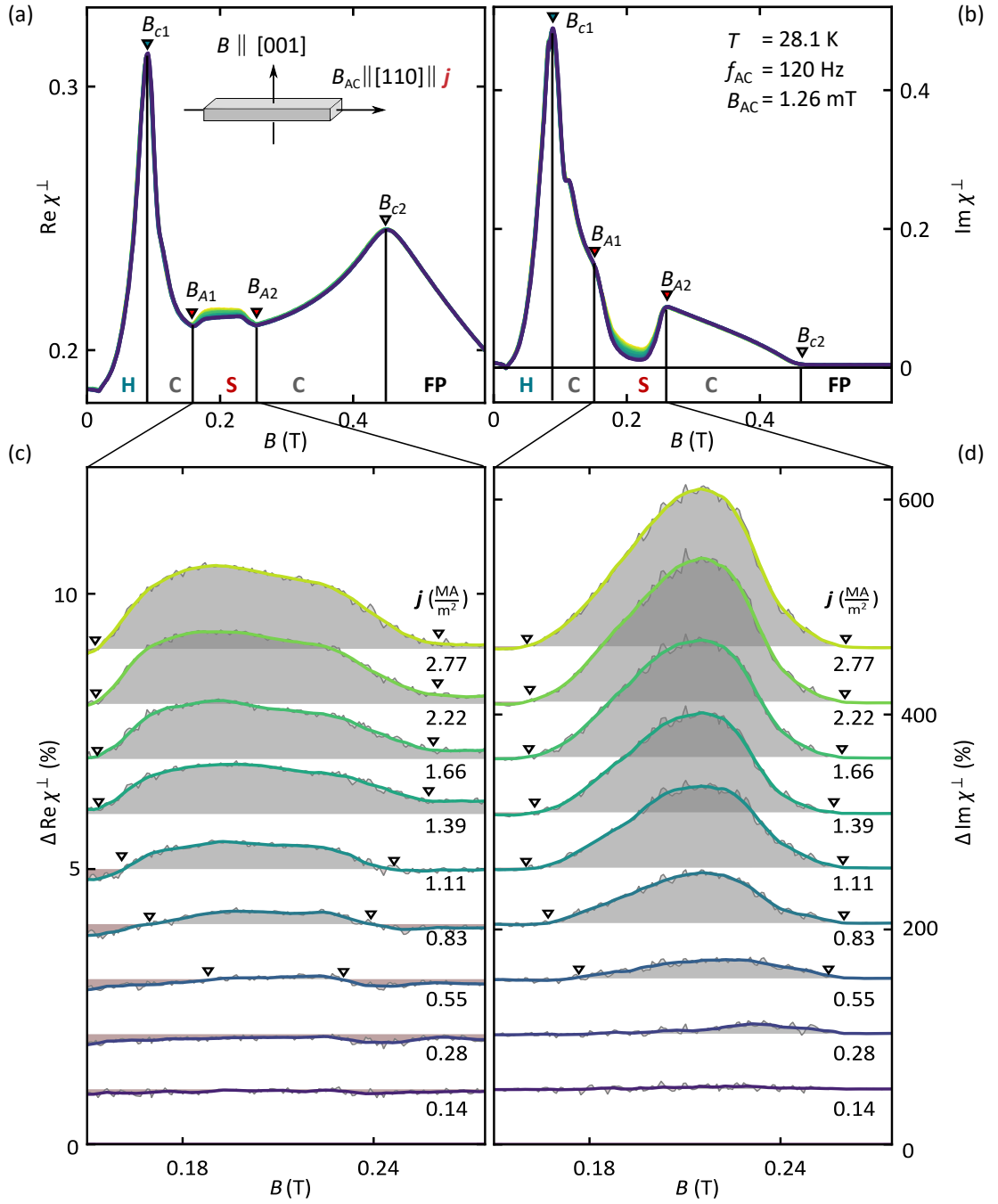
92

Figure 3.28.: Influence of an applied current on the transverse susceptibility $\chi_\perp$. (a) Magnetic field dependence of the real part of the susceptibility $\mathrm{Re}\,\chi_\perp$ at different current densities between $j = 0$ and $j = 2.77\,\mathrm{MAm}^{-2}$. Phase transitions are marked by coloured triangles. (b) Imaginary part $\mathrm{Im}\,\chi_\perp$ of the transverse susceptibility and schematic depiction of the sample orientation during the spin torque measurement. (c), (d) Close-up view of the change of the susceptibility $\Delta\chi_\perp$ in the skyrmion lattice phase for different current densities. An additional contribution to $\chi_\perp$ is visible above a critical current density of $j_c = 0.83\,\mathrm{MAm}^{-2}$ in both $\mathrm{Re}\,\chi_\perp$ and $\mathrm{Im}\,\chi_\perp$.

No influence of the applied current on the transverse susceptibility may be observed in helical phase, conical phase, and in the field-polarised state. However, in the skyrmion lattice phase, real and imaginary parts of the susceptibility increase as a function of applied current density j.

A detailed evaluation of this increase is shown in figures 3.28 (c) and (d). Here, the relative deviation of $\chi_\perp$ from its value at zero current,

$$\Delta\chi_\perp \, (\%) = \left| \frac{\chi_\perp(j \neq 0) - \chi_\perp(j = 0)}{\chi_\perp(j = 0)} \right|, \tag{3.16}$$

is depicted as a function of the applied field for the skyrmion lattice. $\mathrm{Re}\,\chi_\perp$ exhibits no change below a threshold current of $j_c \approx 0.83\,\mathrm{MAm}^{-2}$ and increases gradually as a function of applied current density. At the highest current density investigated, $j \approx 2.77\,\mathrm{MAm}^{-2}$, $\mathrm{Re}\,\chi_\perp$ increases by $\approx 1\,\%$ as compared to the zero current value, uniformly over the entire field range of the skyrmion lattice phase. Figures 3.28 (b) and (d) present the corresponding imaginary part, $\mathrm{Im}\,\chi_\perp$, which exhibits a similar additional contribution, exceeding $100\,\%$ at the highest current densities. However, $\mathrm{Im}\,\chi_\perp$ displays a broad, peak-like structure with a maximum located in the centre of the skyrmion lattice phase. Additionally, small contributions to $\mathrm{Im}\,\chi_\perp$ may already be observed at current densities above $j \gtrsim 0.55\,\mathrm{MAm}^{-2}$.

An evaluation of the transverse susceptibility is presented for the different magnetic phases of MnSi in figure 3.29. Here, the relative increase of the transverse susceptibility $\Delta\,\chi_\perp$, is shown as a function of the applied current density j. The susceptibility has been evaluated in the helical phase (H) for $B = 10\,\mathrm{mT}$, the skyrmion lattice phase (S) for $B = 200\,\mathrm{mT}$, the conical phase (C) for $B = 300\,\mathrm{mT}$ and the field polarised state (FP) for $B = 500\,\mathrm{mT}$. In the skyrmion lattice phase (red dots), an additional contribution to $\mathrm{Re}\,\chi_\perp$ may be observed above the critical current density j_c. This contribution saturates above current densities of $j > 2.5\,\mathrm{MAm}^{-2}$ exceeding an increase of $1\,\%$. The imaginary part exhibits a qualitatively similar behaviour, with a significantly higher relative contribution exceeding $100\,\%$ at high current densities. The large values observed in the imaginary part, however, are attributed to the vanishingly small intensity of $\mathrm{Im}\,\chi_\perp$ in the skyrmion lattice phase, without applied current. No significant changes of $\chi_\perp$ as a function of applied current may be observed in the other magnetic phases, except for the B_{c1} transition, where $\chi_\perp$ exhibits a small additional contribution. This might be related to topologically non-trivial defects at this transition. A detailed discussion of this effect exceeds the scope of this thesis and further information may be found in reference [105]. The discussion presented in the following focuses on spin torque effects in the skyrmion lattice phase only.

Figure 3.28 shows that $\mathrm{Re}\,\chi_\perp$ remains unchanged for current densities below $j_c = 0.83\,\mathrm{MAm}^{-2}$. In this regime, the pinning forces F_{Pin}, generated by defects and surface effects, exceed the drag forces F_{Drag}, generated by the spin current, and prevent a movement of the skyrmion lattice
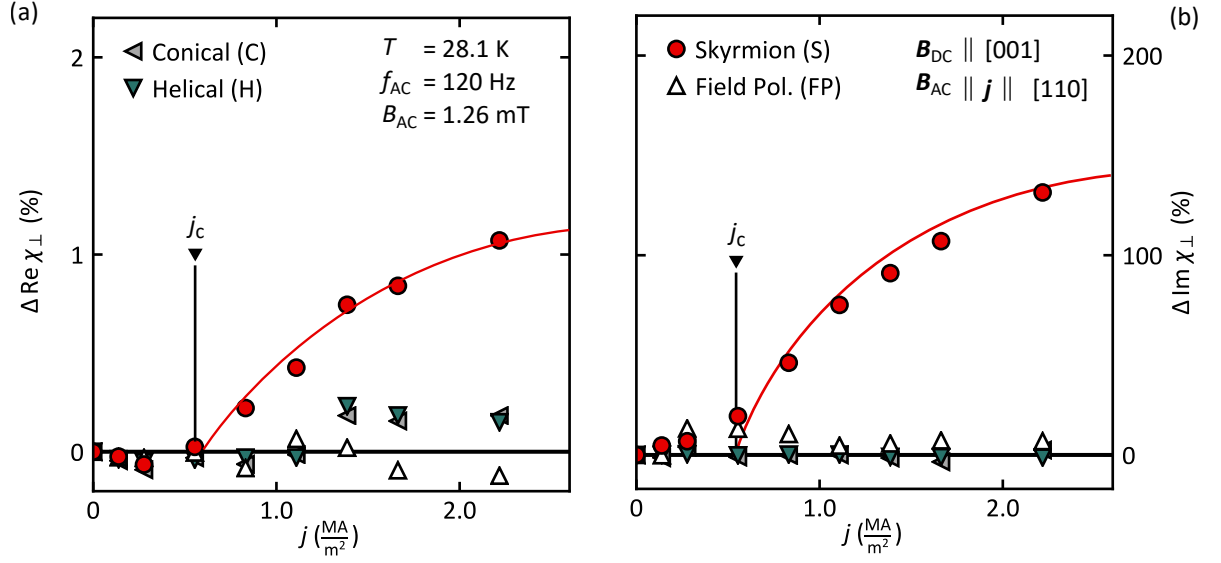
Figure 3.29.: Relative change of the real part of the transverse susceptibility $\Delta\chi_\perp$ as a function of applied DC current density j in different magnetic states of MnSi. Measurements have been evaluated at $B = 10\,\text{mT}$ for the helical phase (H), at $B = 200\,\text{mT}$ for the skyrmion lattice phase (S), at $B = 300\,\text{mT}$ for the conical phase (C) and at $B = 500\,\text{mT}$ for the field polarised state (FP). (a) Relative change of the real part of the susceptibility $\Delta\text{Re}\,\chi_\perp$. An increase is observed at the critical current density $j_c \approx 0.83\,\text{MAm}^{-2}$ in the skyrmion lattice phase. All other phases remain unaffected. (b) Relative change of the imaginary part of the susceptibility $\Delta\text{Im}\,\chi_\perp$. Similar to $\Delta\text{Re}\,\chi_\perp$, a strong increase is observed at j_c in the skyrmion lattice phase.

resulting in a constant $\chi_\perp$. As discussed in section 3.3.3, the susceptibility signal for the given excitation frequency $f_\text{AC} = 120\,\text{Hz}$ and excitation amplitude $B_\text{AC} = 1.26\,\text{mT}$ at zero applied current is generated by the response of single spins within the skyrmion lattice. In this regime (region B) the skyrmion lattice is not able to follow the applied field oscillation. However, with an applied current $j > j_c$, the skyrmion lattice is unpinned from defects. Then, we suspect that the entire skyrmion lattice may follow the applied field oscillation, resulting in an enhanced contribution to $\text{Re}\,\chi_\perp$. This suspicion will be supported further in our discussion in section 3.3.5, where we include the excitation amplitude as an additional parameter to our measurements.

Tracking the onset of the additional contribution, the critical current density j_c may be extracted from the transverse susceptibility as shown in figure 3.29. It is important to appreciate that this contribution can only be detected in the present geometry, where the susceptibility is probed in the plane of the skyrmion lattice and parallel to the applied current, in contrast to conventional, longitudinal configurations, where the susceptibility is probed perpendicular to the skyrmion flow direction as described in section 3.3.4 and in reference [15].

3.3.5. Suppression of the Critical Current by an Oscillating Magnetic Field

In the following, the response of j_c to variations of the applied oscillating field B_{AC} are reported. Therefore, the measurements presented previously were repeated using different excitation amplitudes between $B_{AC} = 1.26\,\text{mT}$ and $B_{AC} = 12.59\,\text{mT}$. Following the same procedure as in section 3.3.4, the relative increase of the susceptibility $\Delta\chi_\perp$ as defined in equation 3.16 may be determined as a function of the applied current density j in the skyrmion lattice phase.

Shown in figure 3.30 (a) is the relative increase of the real part of the susceptibility, $\Delta\text{Re}\,\chi_\perp$, for different excitation amplitudes evaluated in the skyrmion lattice phase at $B = 200\,\text{mT}$. Data were recorded at $T = 28.1\,\text{K}$ and an excitation frequency $f_{AC} = 120\,\text{Hz}$ and are shifted for better visualisation. The purple curve, depicting the lowest excitation amplitude in figure 3.30 (a), has already been discussed in the previous section in detail (cf. figure 3.29 (a)). In the following, the influence of an increasing excitation amplitude B_{AC} on the shape of this curve is investigated, focussing especially on the critical current j_c, denoted by red triangles. With increasing excitation amplitude, onset and curve shape remain essentially unchanged up to excitation amplitudes $B_{AC} \gtrsim 3.15\,\text{mT}$. Further increasing B_{AC} results in a shift of j_c towards very low current densities. For amplitudes exceeding $B_{AC} = 3.78\,\text{mT}$, the resolution is not sufficient to establish a finite value of j_c, with an upper limit $j_c < 0.14\,\text{MAm}^{-2}$. Increasing B_{AC} even further causes a decrease of the additional contribution, $\Delta\text{Re}\,\chi_\perp$, which nearly vanishes at $B_{AC} = 12.59\,\text{mT}$, the highest amplitude studied. Shown in figure 3.30 (b) is the critical current density j_c as a function of excitation amplitude B_{AC}. The decrease of j_c may be observed above a critical excitation amplitude $B_{AC}^c \approx 3.5\,\text{mT}$.

For our discussion, it is instructive to consider first the relative change of the transverse susceptibility $\Delta\text{Re}\,\chi_\perp$ with respect to its value at $B_{AC} = 0.16\,\text{mT}$, the lowest excitation amplitude measured, as a function of B_{AC} at zero current, as depicted in figure 3.30 (c). It was argued in section 3.3.3, that the susceptibility in the skyrmion lattice phase increases as a function of B_{AC}, as the system changes from a single spin response in region B, to a response of the entire magnetic structure in region A. This increase may be observed in figure 3.30 (c) where both limits are clearly visible and indicated by black lines. As discussed in the previous section for the measurement at $B_{AC} = 1.25\,\text{mT}$, we suspect that the susceptibility increases as a result of the unpinning of the skyrmion lattice at j_c as a function of applied current density. With increasing excitation amplitude, this situation remains unchanged up to amplitudes exceeding $B_{AC} \approx 3.15\,\text{mT}$. In this regime, the system remains in state B at zero current and the influence of the applied current may only be observed above j_c.

However, exceeding the critical amplitude $B_{AC}^c \approx 3.5\,\text{mT}$, the onset indicating j_c is shifted towards smaller currents. As depicted in figures 3.30 (b) and (c), this coincides with the transi-
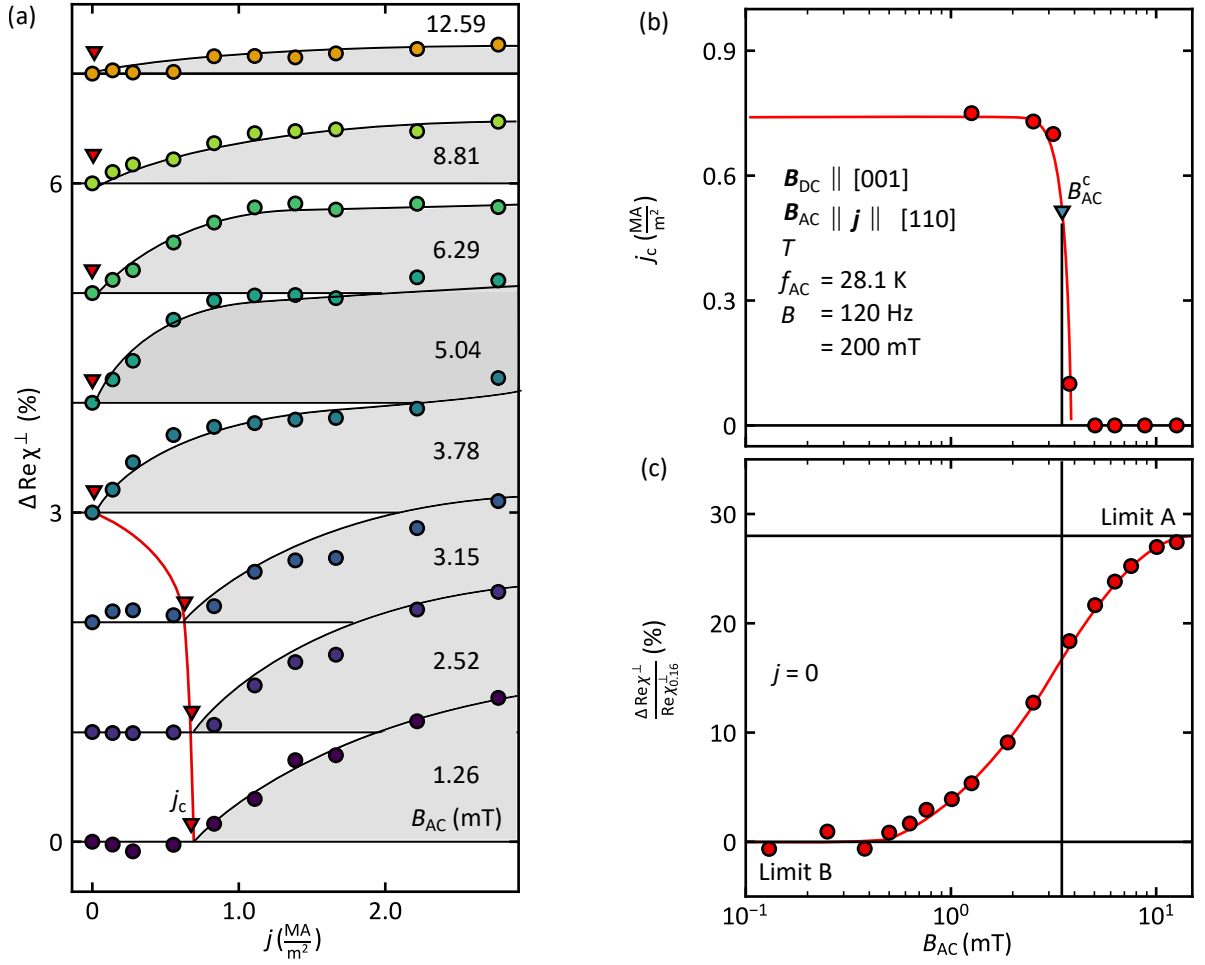
Figure 3.30.: Variation of the critical current density j_c as a function of the excitation ampli-
tude B_{AC}. (a) Relative increase of the real part of the susceptibility $\Delta \operatorname{Re} \chi_\perp$ as
a function of the applied current density j. Red triangles indicate j_c, defined at
the onset of the increase of $\operatorname{Re} \chi_\perp$. This onset is shifted towards lower currents
for increasing excitation amplitudes (red line). (b) Critical current densities j_c
extracted from (a) as a function of excitation amplitude B_{AC}. Green trian-
gle marks the critical field B_{AC}^c, above which j_c falls below $j_c \leq 0.14 \, \mathrm{MAm}^{-2}$.
(c) Relative increase of $\operatorname{Re} \chi_\perp$ compared to its value at the lowest excitation
amplitude of $B_{AC} = 0.16 \, \mathrm{mT}$ as a function of the excitation amplitude B_{AC} at
zero current. The system transits from limit B at small excitation amplitudes,
to limit A for large amplitudes exceeding $B_{AC} \gtrsim 12 \, \mathrm{mT}$, in agreement with the
schematic depiction presented in figure 3.27.

tion of the system at zero current from state B to state A. Hence, above excitation amplitudes
of B_{AC}^c, the skyrmion lattice is already able to follow partially the oscillation of the applied
field, even at zero current. We suspect that, in this regime, the skyrmion lattice is unpinned
from defects by the oscillation of the applied magnetic field and spin torque effects may already

be observed at the smallest current densities, investigated in this study. The fact that the susceptibility value still increases as a function of applied current density, even at large excitation amplitudes, as observed in figure 3.30 (a), suggests that the lattice is not yet completely free to follow the applied field oscillation and the unpinning of the skyrmion lattice by the applied current still affects the response of the skyrmion lattice.

This situation changes when approaching large excitation amplitudes $B_{AC} \gtrapprox 12 \, \text{mT}$. Here, the influence of the applied current density is reduced as compared to data, collected at smaller amplitudes. In this regime, the skyrmion lattice may be unpinned completely by the applied magnetic field and can follow any change of the field direction at excitation frequencies smaller than $f_{AC} \approx 120 \, \text{Hz}$. It may be seen in figure 3.30 (c) that the curve has not yet saturated completely in limit A at the highest amplitude $B_{AC} = 12.59 \, \text{mT}$. We suspect that no further influence of the applied current may be observed as soon as this limit is reached. Then, the skyrmion lattice is already unpinned completely by the oscillating magnetic field and the additional spin current does not influence the susceptibility measurement. This may be interpreted as an extremely reduced critical current density, as compared to measurements without applied oscillating field. This interpretation agrees qualitatively and quantitatively with the neutron scattering data, presented in section 3.3.4 and reference [192]. In their study, Mühlbauer *et al.* report a critical amplitude for the free oscillation of the skyrmion lattice of $B_{AC}^c \approx 4 \, \text{mT}$ at a frequency of $f_{AC} = 325 \, \text{Hz}$ which agrees with the values, reported in this study.

3.4. Summary & Outlook

In this chapter, the influence of an oscillating magnetic field on the critical current j_c for the skyrmion movement in MnSi was investigated by means of transverse susceptibility measurements. First, generic properties of the transverse susceptibility were presented and compared to the well know longitudinal susceptibility, establishing the transverse susceptibility as a complementary probe to conventional susceptibility measurements. A detailed investigation of the full magnetic field and temperature dependence of the transverse susceptibility of MnSi was conducted for the first time, revealing an additional contribution to the susceptibility just below B_{c2}, that has remained unnoticed in previous studies. Subsequently, the dependence of the transverse susceptibility on excitation amplitude and frequency was determined in detail. Two limits of the susceptibility in conical and skyrmion lattice phase were established, which correspond to a collective response of the magnetic structure and a response of individual spins, respectively. Additionally, a strong variation of the transverse susceptibility at the helical to conical transition could be observed as a function of excitation frequency and amplitude. This may be connected to complex domain reorientations and the breaking of the $\mathbb{Z}_2$ symmetry at this transition. In helical as well as field-polarised state, no influence on $\chi_\perp$ stemming from changes of excitation amplitude or frequency could be observed.

In the second part, the response of the transverse susceptibility to an applied DC current was investigated. First, measurements as a function of applied current were conducted at fixed excitation amplitudes and frequencies, establishing a way to capture spin torque effects in the skyrmion lattice phase using transverse susceptibility measurements. Subsequently, the critical current j_c for the skyrmion movement could be extracted from our measurements. Additionally, small spin torque effects could be observed at the helical to conical transition at B_{c1}, possibly attributed to topological defects at this transition. No spin torque effects could be observed in all other phases for the current densities investigated. In a second step, similar measurements were performed under variation of the excitation amplitude B_{AC}. It could be shown that j_c may be reduced below a threshold value of $j_c \lesssim 0.15 \, \mathrm{MAm}^{-2}$ by the application of a transverse oscillating magnetic field larger than $B_{AC}^c \gtrsim 3.5 \, \mathrm{mT}$. Based on our findings in the first part of this chapter, we interpret this effect as a combination of the unpinning of the skyrmion lattice mediated by the oscillating field and the applied current density.

Besides the results discussed in this study, the comprehensive investigation of the transverse susceptibility revealed a couple of new phenomena, which have not been discussed in detail. Notably, we suggest a further investigation of the so-far unrecognised feature, identified in the conical phase, a further investigation of the helical to conical transition by means of transverse susceptibility measurements as well as the confirmation of our results on the critical current by complementary methods.

Conclusions

The focus of this thesis was the investigation of the dynamic properties of complex magnetic structures and quantum phase transitions as probed by transverse susceptibility measurements. After a short overview of technical developments in the first chapter, the second chapter focused on the investigation of the low-temperature properties of the dipolar-coupled Ising ferromagnet $LiHoF_4$, representing a generic example of a transverse field-tuned quantum phase transition. In the third chapter, the interaction of spin currents with a topologically non-trivial spin structure, the skyrmion lattice, in the cubic helimagnet MnSi was investigated.

In the initial technical part of this work, we presented the development of three bespoke low-temperature AC susceptometers, which were an indispensable prerequisite for a successful investigation of the transverse susceptibility. The susceptometers have been successfully tested and calibrated to provide reliable measurement results. Additionally, the existing measurement automation software was further developed and restructured to facilitate the integration of new measurement equipment, provide accurate measurement timing, and to optimize on-the-fly data evaluation.

In the second chapter, the investigation of the low temperature properties of the Ising ferromagnet $LiHoF_4$ was divided into two parts. First, the phase boundaries of the ferromagnetic state, including the quantum phase transition at high transverse magnetic fields, were examined. Therefore, the influence of small misalignments between the applied magnetic field and the sample orientation were investigated and it was shown that a second order quantum phase transition is restricted to angular deviations from the perpendicular orientation below $\varphi = 0.25°$. Larger deviations lead to signatures, typically associated with first-order transitions, obscuring the underlying quantum critical point. Then, the critical exponents were investigated at the thermal and the quantum phase transition, yielding a value of $\gamma \approx 1$. This indicates a mean-field transition in both the thermal and in the quantum limit in agreement with the established theoretical picture and previous studies. Additionally, a mismatch between current theoretical predictions and experimental observations concerning the phase boundary at small magnetic field was ad-

dressed and we propose a refinement of the theoretical description based on our observations. In the second part, three distinct regimes in the ferromagnetic ground state of the system could be identified. In the first regime, the AC susceptibility saturates on a demagnetisation plateau, indicating completely free domain wall movement in the ferromagnetic phase just below T_c. In the second regime, a steep decrease of the susceptibility at low temperatures and magnetic fields with a distinct frequency dependence suggests a freezing of the domain-walls due to a lack of thermal energy. This was analogously observed in the doped compound $LiY_{1-x}Ho_xF_4$ [78], with $x = 0.55$, and questions the assumption of Bitko [75], who suggested a quantum glass state at low temperatures in the pure compound. In the third regime, the free domain-wall movement can be restored by the application of a transverse magnetic field, even at lowest temperatures, indicating a purely quantum nature of the phenomenon. In analogy to reference [78], we suspect that the increased domain-wall mobility is caused by quantum-tunnelling effects of the domain walls generated by the transverse magnetic field. Finally, we have observed an additional contribution to the transverse susceptibility around the quantum critical point associated with a strong hyperfine coupling, which is believed to stabilise the magnetic order and to conceal the quantum critical point.

The third chapter, concerned with the investigation of the interplay of spin currents with the skyrmion lattice in MnSi comprises four parts. First, the transverse susceptibility was established as a suitable tool for the investigation of specific properties in systems with complex magnetic order, complementing the conventionally investigated longitudinal susceptibility. Thereby an additional contribution to the susceptibility could be identified near the ferromagnetic transition at high magnetic fields and low temperatures, which remained unnoticed in literature so-far. In a second step, a variation of excitation frequency and amplitude revealed two distinct limits of $\mathrm{Re}\,\chi_\perp$ in conical and skyrmion lattice phase, representing collective and isolated spin responses, respectively. Next, signatures of the skyrmion lattice movement in MnSi were identified in the transverse susceptibility, providing the possibility to extract the critical current density j_c from our measurements. Besides, a small contribution of the applied current at B_{c1} was observed, which we attributed to a coupling of the spin current to topologically non-trivial defects, which are believed to exist at this transition [105]. Finally, we showed that the critical current density in the skyrmion lattice of MnSi can be reduced by more than one order of magnitude by the application of an oscillating magnetic field. Based on our previous considerations we proposed that this reduction is a result of the unpinning of the skyrmion lattice from defects as a result of the applied oscillating field above a critical amplitude $B_{\mathrm{AC}}^c = 3.5\,\mathrm{mT}$.

Publications

1. **Room-temperature helimagnetism in FeGe thin films**
   S. L. Zhang, I. Stasinopoulos, T. Lancaster, F. Xiao, A. Bauer, <u>F. Rucker</u>, A. A. Baker, A. I. Figueroa, Z. Salman, F. L. Pratt, S. J. Blundell, T. Rokscha, A. Suter, J. Waizner, M. Garst, D. Grundler, G. van der Laan, C. Pfleiderer and T. Hesjedal
   Scientific Reports **7**, 123 (2017)

2. **Uniaxial Pressure Dependence of Magnetic Order in MnSi**
   A. Chacón, A. Bauer, T. Adams, <u>F. Rucker</u>, G. Brandl, R. Georgii, M. Garst and C. Pfleiderer
   Physical Review Letters **115**, 267202 (2015)

3. **High performance, large cross-section S-bender for neutron polarization**
   Th. Krist, <u>F. Rucker</u>, G. Brandl and R. Georgii
   Nuclear Instruments and Methods in Physics Research Section A **698**, 94 (2013)

Acknowledgments

Während der letzten Jahre haben mich viele Menschen sowohl fachlich als auch persönlich begleitet, unterstützt und motiviert und damit maßgeblich zum erfolgreichen Abschluss dieser Arbeit beigetragen. Besonderer Dank gilt

- Christian Pfleiderer, für die freundschaftliche Atmosphäre, die vertrauensvolle Zusammenarbeit und die hervorragenden Arbeitsbedingungen am Lehrstuhl. Vielen Dank, dass du mir schon seit Beginn meines Studiums stets mit Rat und Tat zur Seite stehst und mir die Promotion an deinem Lehrstuhl ermöglicht hast.

- Peter Böni, für die angenehme Zusammenarbeit und für viele interessante Gespräche, auch über die Physik hinaus, bei diversen Kaffeerunden und Skiausflug-Busfahrten.

- meinen langjährigen Bürokollegen Christoph Schnarr, Jonas Kindervater, Georg Benka, Stefan Giemsa und Steffen Säubert für unzählige Stunden an ernsthaften Diskussionen und unsinnigem Geschwätz, die einen Arbeitstag oft wie im Flug vergehen ließen.

- meinen Labor-Kollegen Christopher Duvinage, Christoph Schnarr, Alexander Regnat, Jan Spallek und neuerdings auch Markus Kleinhans. Vielen Dank für die tatkräftige Unterstützung über die letzten Jahre, auch zu den unmöglichsten Uhrzeiten. Insbesondere Danke an Christoph & Christopher für die vielen gemeinsamen Lösungen jeglicher Labor-Probleme und für die hilfreichen Kommentare zu dieser Arbeit.

- Andreas Bauer, unserem Post-Doc-Techniker-Sektretär, für seine Unterstützung bei Vorträgen, Postern, Papern und eigentlich Allem, speziell natürlich bei dieser Arbeit, und für die gute Zusammenarbeit bei allen Klempner-, Elektriker-, Mechaniker- und was-sonst-noch-so-anfällt-Arbeiten ("Bauer-Rucker GmbH, alles außer Tiernahrung").

- allen Kollegen am E51: Den Doktoranden-Opas und -Omas Christian Franz, Christopher Duvinage, Christoph Schnarr, Alexander Regnat, Jonas Kindervater, Tim Adams, Michael Wagner, Robert Ritz, Birgit Wiedemann, Alfonso Chachon, Marco Halder, Philipp Schmakat, Tomek Schulz und meinem Mentor Marc Janoschek von denen ich, vom sauberen

107

APPENDIX A

Uncorrected Frequency Dependence

Raw data of the imaginary part of the transverse susceptibility, $\mathrm{Im}\,\chi_\perp$, is shown as a function of magnetic field at different frequencies in figure A.1 (a). The data is subject to a frequency-dependent offset, generated by eddy currents. The offset was determined by assuming no influence of the excitation frequency on the susceptibility value in the field polarised state above B_{c2} and is shown in figure A.1 (b). For the discussion in this thesis, this offset was subtracted.
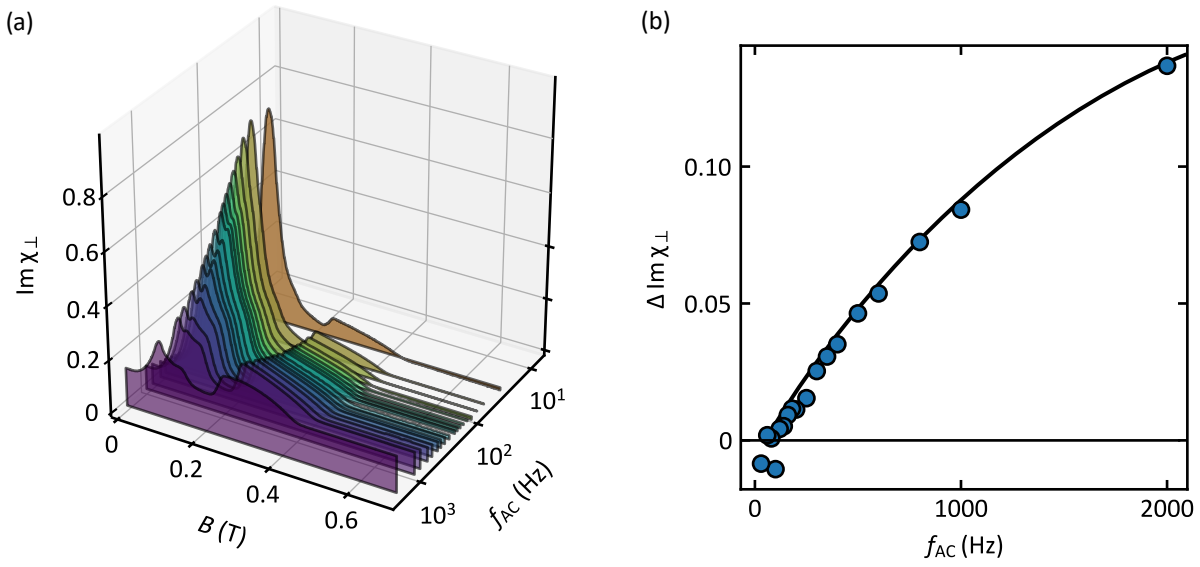
(a)

(b)

Figure A.1.: Raw data of $\mathrm{Im}\,\chi_\perp$ and corresponding offset due to the generation of eddy currents by the oscillating field. (a) Uncorrected data of the imaginary part of the transverse susceptibility $\mathrm{Im}\,\chi_\perp$ as a function of excitation frequency taken at $T = 28.15\,\mathrm{K}$ and at excitation frequencies between $20\,\mathrm{Hz}$ and $2000\,\mathrm{Hz}$ and a fixed excitation amplitude of $B_{\mathrm{AC}} = 2.52\,\mathrm{mT}$. (b) Offset resulting from the generation of eddy currents. The offset has been estimated by assuming no influence of the excitation frequency in the field polarised regime above B_{c2}. Line serves as guide to the eye.

Bibliography

[1] M. R. Norman, The challenge of unconventional superconductivity, Science **332**, 196 (2011).

[2] G. R. Stewart, Unconventional superconductivity, Adv. Phys. **66**, 75 (2017).

[3] J. E. Moore, The birth of topological insulators, Nature **464**, 194 (2010).

[4] X.-L. Qi and S.-C. Zhang, Topological insulators and superconductors, Rev. Mod. Phys. **83**, 1057 (2011).

[5] A. P. Ramirez, Strongly geometrically frustrated magnets, Annu. Rev. Mater. Sci. **24**, 453 (1994).

[6] W. Eerenstein, N. D. Mathur, and J. F. Scott, Multiferroic and magnetoelectric materials, Nature **442**, 759 (2006).

[7] S. Mühlbauer, B. Binz, F. Jonietz, C. Pfleiderer, A. Rosch, A. Neubauer, R. Georgii, and P. Böni, Skyrmion lattice in a chiral magnet, Science **323**, 915 (2009).

[8] S. Sachdev and B. Keimer, Quantum criticality, Phys. Today **64**, 29 (2011).

[9] D. Bitko, T. F. Rosenbaum, and G. Aeppli, Quantum critical behavior for a model magnet, Phys. Rev. Lett. **77**, 940 (1996).

[10] S. Sachdev, *Quantum Phase Transitions*, 2nd ed. (Cambridge University Press, 2011).

[11] C. Pfleiderer, S. R. Julian, and G. G. Lonzarich, Non-Fermi-liquid nature of the normal state of itinerant-electron ferromagnets, Nature **414**, 427 (2001).

[12] C. Pfleiderer, P. Böni, T. Keller, U. K. Rößler, and A. Rosch, Non-Fermi liquid metal without quantum criticality, Science **316**, 1871 (2007).

Bibliography

[13] R. Ritz, M. Halder, M. Wagner, C. Franz, A. Bauer, and C. Pfleiderer, Formation of a topological non-Fermi liquid in MnSi, Nature **497**, 231 (2013).

[14] A. Neubauer, C. Pfleiderer, B. Binz, A. Rosch, R. Ritz, P. G. Niklowitz, and P. Böni, Topological Hall effect in the A phase of MnSi, Phys. Rev. Lett. **102**, 186602 (2009).

[15] F. Jonietz, S. Mühlbauer, C. Pfleiderer, A. Neubauer, W. Münzer, A. Bauer, T. Adams, R. Georgii, P. Böni, R. A. Duine, K. Everschor, M. Garst, and A. Rosch, Spin transfer torques in MnSi at ultralow current densities, Science **330**, 1648 (2010).

[16] T. Schulz, R. Ritz, A. Bauer, M. Halder, M. Wagner, C. Franz, C. Pfleiderer, K. Everschor, M. Garst, and A. Rosch, Emergent electrodynamics of skyrmions in a chiral magnet, Nat. Phys. **8**, 301 (2012).

[17] Z. Diao, Z. Li, S. Wang, Y. Ding, A. Panchula, E. Chen, L.-C. Wang, and Yiming Huai, Spin-transfer torque switching in magnetic tunnel junctions and spin-transfer torque random access memory, J. Phys.: Condens. Matter **19**, 165209 (2007).

[18] S. S. P. Parkin, M. Hayashi, and L. Thomas, Magnetic domain-wall racetrack memory, Science **320**, 190 (2008).

[19] A. Fert, V. Cros, and J. Sampaio, Skyrmions on the track, Nat. Nanotechnol. **8**, 152 (2013).

[20] R. Tomasello, E. Martinez, R. Zivieri, L. Torres, M. Carpentieri, and G. Finocchio, A strategy for the design of skyrmion racetrack memories, Sci. Rep. **4**, 06784 (2014).

[21] W. Koshibae and N. Nagaosa, Creation of skyrmions and antiskyrmions by local heating, Nat. Commun. **5**, 5148 (2014).

[22] W. Koshibae, Y. Kaneko, J. Iwasaki, M. Kawasaki, Y. Tokura, and N. Nagaosa, Memory functions of magnetic skyrmions, Jpn. J. Appl. Phys. **54**, 053001 (2015).

[23] S. Blundell, *Magnetism in Condesed Matter* (Oxford University Press Inc., New York, 2001).

[24] N. W. Ashcroft and N. D. Mermin, *Festkörperphysik* (De Gruyter, 2001).

[25] C. Pfleiderer, Miniature AC susceptometers for use inside clamp type pressure cells, Rev. Sci. Instr. **68**, 1532 (1997).

[26] F. Rucker, *High Precision Susceptometer for Angle-Resolved Studies of Quantum Phase Transitions*, Diploma Thesis, TU München (2013).

[27] C. Krey, *Spulen-Vibrationsmagnetometrie an Frustrierten Magneten Bei mK–Temperaturen*, Diploma Thesis, TU München (2013).

[28] H. London, G. R. Clarke, and E. Mendoza, Osmotic pressure of ^{3}He in liquid ^{4}He, with proposals for a refrigerator to work below 1K, Phys. Rev. **128**, 1992 (1962).

[29] D. S. Betts, *Refrigeration and Thermometry below One Kelvin* (Sussex University Press, 1976).

[30] R. Ritz, *Phasenübergänge Schwach-Magnetischer Metalle Unter Extremen Bedingungen*, Diploma Thesis, TU München (2007).

[31] M. Brando, D. Belitz, F. M. Grosche, and T. R. Kirkpatrick, Metallic quantum ferromagnets, Rev. Mod. Phys. **88**, 025006 (2016).

[32] M. Vojta, Quantum phase transitions, Rep. Prog. Phys. **66**, 2069 (2003).

[33] N. Mott, On metal-insulator transitions, J. Solid State Chem. **88**, 5 (1990).

[34] P. Sémon and A.-M. S. Tremblay, Importance of subleading corrections for the Mott critical point, Phys. Rev. B **85**, 201101 (2012).

[35] S. Onoda and N. Nagaosa, Mott transition vs multicritical phenomenon of superconductivity and antiferromagnetism — application to κ-(BEDT-TTF)$_2X$—, J. Phys. Soc. Jpn. **72**, 2445 (2003).

[36] L. D. Landau and E. M. Lifshitz, *Course of Theoretical Physics*, Vol. 8 (Pergamon Press, 1980).

[37] K. G. Wilson, The renormalization group and critical phenomena, Rev. Mod. Phys. **55**, 583 (1983).

[38] M. E. Fisher, The theory of equilibrium critical phenomena, Rep. Prog. Phys. **30**, 615 (1967).

[39] A. Kopp and S. Chakravarty, Criticality in correlated quantum matter, Nat. Phys. **1**, 53 (2005).

[40] C. L. Seaman, M. B. Maple, B. W. Lee, S. Ghamaty, M. S. Torikachvili, J.-S. Kang, L. Z. Liu, J. W. Allen, and D. L. Cox, Evidence for non-Fermi liquid behavior in the Kondo alloy $y_{1-x}u_x$pd$_3$, Phys. Rev. Lett. **67**, 2882 (1991).

[41] H. v. Löhneysen, T. Pietrus, G. Portisch, H. G. Schlager, A. Schröder, M. Sieck, and T. Trappmann, Non-Fermi-liquid behavior in a heavy-fermion alloy at a magnetic instability, Phys. Rev. Lett. **72**, 3262 (1994).

[42] F. M. Grosche, C. Pfleiderer, G. J. McMullan, G. G. Lonzarich, and N. R. Bernhoeft, Critical behaviour of ZrZn2, Physica B **206-207**, 20 (1995).

Bibliography

[43] C. Pfleiderer, G. J. MeMullan, and G. G. Lonzarich, Critical behaviour at the transition from a magnetic to a nonmagnetic metallic state in MnSi as a function of hydrostatic pressure, Physica B **199-200**, 634 (1994).

[44] C. Pfleiderer, G. J. McMullan, S. R. Julian, and G. G. Lonzarich, Magnetic quantum phase transition in MnSi under hydrostatic pressure, Phys. Rev. B **55**, 8330 (1997).

[45] C. Pfleiderer, C. Thessieu, A. N. Stepanov, G. Lapertot, M. Couach, and J. Flouquet, Field dependence of the magnetic quantum phase transition in MnSi, Phys. B **230-232**, 576 (1997).

[46] C. Thessieu, C. Pfleiderer, A. N. Stepanov, and J. Flouquet, Field dependence of the magnetic quantum phase transition in MnSi, J. Phys.: Condens. Matter **9**, 6677 (1997).

[47] C. Pfleiderer, Experimental studies of weakly magnetic transition metal compounds, J. Magn. Magn. Mater. **226-230**, 23 (2001).

[48] D. Belitz, T. R. Kirkpatrick, and J. Rollbühler, Tricritical behavior in itinerant quantum ferromagnets, Phys. Rev. Lett. **94**, 247205 (2005).

[49] P. Gegenwart, Q. Si, and F. Steglich, Quantum criticality in heavy-fermion metals, Nat. Phys. **4**, 186 (2008).

[50] N. D. Mathur, F. M. Grosche, S. R. Julian, I. R. Walker, D. M. Freye, R. K. W. Haselwimmer, and G. G. Lonzarich, Magnetically mediated superconductivity in heavy fermion compounds, Nature **394**, 39 (1998).

[51] F. M. Grosche, I. R. Walker, S. R. Julian, N. D. Mathur, D. M. Freye, M. J. Steiner, and G. G. Lonzarich, Superconductivity on the threshold of magnetism in CePd 2 Si 2 and CeIn 3, J. Phys.: Condens. Matter **13**, 2845 (2001).

[52] G. R. Stewart, Non-Fermi-liquid behavior in d- and f-electron metals, Rev. Mod. Phys. **73**, 797 (2001).

[53] H. v. Löhneysen, A. Rosch, M. Vojta, and P. Wölfle, Fermi-liquid instabilities at magnetic quantum phase transitions, Rev. Mod. Phys. **79**, 1015 (2007).

[54] P. Coleman and A. J. Schofield, Quantum criticality, Nature **433**, 226 (2005).

[55] G. G. Lonzarich, Quantum criticality: Magnetic quantum liquid enigma, Nat. Phys. **1**, 11 (2005).

[56] C. Pfleiderer, Superconducting phases of f-electron compounds, Rev. Mod. Phys. **81**, 1551 (2009).

[57] T. Park, F. Ronning, H. Q. Yuan, M. B. Salamon, R. Movshovich, J. L. Sarrao, and J. D. Thompson, Hidden magnetism and quantum criticality in the heavy fermion superconductor CeRhIn$_5$, Nature **440**, 65 (2006).

[58] R. Coldea, D. A. Tennant, E. M. Wheeler, E. Wawrzynska, D. Prabhakaran, M. Telling, K. Habicht, P. Smeibidl, and K. Kiefer, Quantum criticality in an ising chain: Experimental evidence for emergent E$_8$ symmetry, Science **327**, 177 (2010).

[59] T. Nikuni, M. Oshikawa, A. Oosawa, and H. Tanaka, Bose-Einstein condensation of dilute magnons in TlCuCl$_3$, Phys. Rev. Lett. **84**, 5868 (2000).

[60] M. Matsumoto, B. Normand, T. M. Rice, and M. Sigrist, Field- and pressure-induced magnetic quantum phase transitions in TlCuCl$_3$, Phys. Rev. B **69**, 054423 (2004).

[61] R. E. Thoma, G. D. Brunton, R. A. Penneman, and T. K. Keenan, Equilibrium relations and crystal structure of lithium fluorolanthanate phases, Inorg. Chem. **9**, 1096 (1970).

[62] A. H. Cooke, D. A. Jones, J. F. A. Silva, and M. R. Wells, Ferromagnetism in lithium holmium fluoride-LiHoF$_4$. I. Magnetic measurements, J. Phys. C **8**, 4083 (1975).

[63] P. B. Chakraborty, P. Henelius, H. Kjønsberg, A. W. Sandvik, and S. M. Girvin, Theory of the magnetic phase diagram of LiHoF$_4$, Phys. Rev. B **70**, 144411 (2004).

[64] P. G. de Gennes, Collective motions of hydrogen bonds, Solid State Commun. **1**, 132 (1963).

[65] R. J. Elliott, P. Pfeuty, and C. Wood, Ising model with a transverse field, Phys. Rev. Lett. **25**, 443 (1970).

[66] J. A. Hertz, Quantum critical phenomena, Phys. Rev. B **14**, 1165 (1976).

[67] M. Suzuki, Relationship between d-dimensional quantal spin systems and (d+1)-dimensional Ising systems: Equivalence, critical exponents and systematic approximants of the partition function and spin correlations, Prog. Theor. Phys. **56**, 1454 (1976).

[68] A. P. Young, Quantum effects in the renormalization group approach to phase transitions, J. Phys. C: Solid State Phys. **8**, L309 (1975).

[69] S. Suzuki, J.-i. Inoue, and B. K. Chakrabarti, *Quantum Ising Phases and Transitions in Transverse Ising Models*, 2nd ed. (Springer-Verlag, 2013).

[70] G. Mennenga, L. J. de Jongh, and W. J. Huiskamp, Field dependent specific heat study of the dipolar Ising ferromagnet LiHoF$_4$, J. Magn. Mang. Mater **44**, 59 (1984).

[71] H. M. Rønnow, R. Parthasarathy, J. Jensen, G. Aeppli, T. F. Rosenbaum, and D. F. McMorrow, Quantum phase transition of a magnet in a spin bath, Science **308**, 389 (2005).

Bibliography

[72] H. M. Rønnow, J. Jensen, R. Parthasarathy, G. Aeppli, T. F. Rosenbaum, D. F. McMorrow, and C. Kraemer, Magnetic excitations near the quantum phase transition in the Ising ferromagnet LiHoF$_4$, Phys. Rev. B **75**, 054426 (2007).

[73] S. M. A. Tabei, M. J. P. Gingras, Y.-J. Kao, and T. Yavors'kii, Perturbative quantum Monte Carlo study of LiHoF$_4$ in a transverse magnetic field, Phys. Rev. B **78**, 184408 (2008).

[74] S. Legl, *Entwicklung Eines Spulen-Vibrationsmagnetometers Zur Untersuchung Korrelierter Elektronensysteme Bei Ultratiefen Temperaturen*, PhD thesis, TU München (2010).

[75] Bitko, *Order and Disorder in a Model Quantum Magnet*, PhD thesis, University of Chicago (1997).

[76] P. Beauvillain, J. P. Renard, I. Laursen, and P. J. Walker, Critical behavior of the magnetic susceptibility of the uniaxial ferromagnet LiHoF$_4$, Phys. Rev. B **18**, 3360 (1978).

[77] J. A. Griffin, M. Huster, and R. J. Folweiler, Critical behavior of the spontaneous magnetization at marginal dimensionality in LiHoF$_4$, Phys. Rev. B **22**, 4370 (1980).

[78] J. Brooke, T. F. Rosenbaum, and G. Aeppli, Tunable quantum tunnelling of magnetic domain walls, Nature **413**, 610 (2001).

[79] A. Bauer, *Investigation of Itinerant Antiferromagnets and Cubic Chiral Helimagnets*, PhD thesis, TU München (2014).

[80] A. Bauer and C. Pfleiderer, Chapter 1: Generic aspects of skyrmion lattices in chiral magnets, in *Topological Structures in Ferroic Materials*, edited by J. Seidel (Springer, 2016) 1st ed.

[81] A. Bauer, A. Neubauer, C. Franz, W. Münzer, M. Garst, and C. Pfleiderer, Quantum phase transitions in single-crystal Mn$_{1-x}$Fe$_x$Si and Mn$_{1-x}$Co$_x$Si: Crystal growth, magnetization, AC susceptibility, and specific heat, Phys. Rev. B **82**, 064404 (2010).

[82] N. Nagaosa and Y. Tokura, Topological properties and dynamics of magnetic skyrmions, Nat. Nano. **8**, 899 (2013).

[83] A. Fert, N. Reyren, and V. Cros, Magnetic skyrmions: Advances in physics and potential applications, Nat. Rev Mater. **2**, 17031 (2017).

[84] M. Garst, Chapter 2: Topological Skyrmion dynamics in chiral magnets, in *Topological Structures in Ferroic Materials*, edited by J. Seidel (Springer, 2016) 1st ed.

[85] H. J. Williams, J. H. Wernick, R. C. Sherwood, and G. K. Wertheim, Magnetic properties of the monosilicides of some 3d transition elements, J. Appl. Phys. **37**, 1256 (1966).

[86] D. Shinoda and S. Asanabe, Magnetic properties of silicides of iron group transition elements, J. Phys. Soc. Jpn. **21**, 555 (1966).

[87] E. Fawcett, J. P. Maita, and J. H. Wernick, Magnetoelastic and thermal properties of MnSi, Int. J. Magn. **1**, 29 (1970).

[88] Y. Ishikawa, K. Tajima, D. Bloch, and M. Roth, Helical spin structure in manganese silicide MnSi, Solid State Commun. **19**, 525 (1976).

[89] S. Kusaka, K. Yamamoto, T. Komatsubara, and Y. Ishikawa, Ultrasonic study of magnetic phase diagram of MnSi, Solid State Commun. **20**, 925 (1976).

[90] K. Motoya, H. Yasuoka, Y. Nakamura, and J. H. Wernick, Helical spin structure in MnSi-NMR studies, Solid State Commun. **19**, 529 (1976).

[91] I. E. Dzialoshinskii, Thermodynamic theory of weak ferromagnetism in antiferromagentic substances, Sov. Phys. JETP **5**, 1259 (1957).

[92] T. Moriya, Anisotropic superexchange interaction and weak ferromagnetism, Phys. Rev. **120**, 91 (1960).

[93] I. E. Dzyaloshinskii, Theory of helicoidal structures in antiferromagnets. I. Nonmetals, Sov. Phys. JETP **19**, 960 (1964).

[94] P. Bak and M. H. Jensen, Theory of helical magnetic structures and phase transitions in MnSi and FeGe, J. Phys. C **13**, L881 (1980).

[95] A. E. Petrova, V. Krasnorussky, J. Sarrao, and S. M. Stishov, Tricritical behavior in MnSi at nearly hydrostatic pressure, Phys. Rev. B **73**, 052409 (2006).

[96] A. E. Petrova and S. M. Stishov, Ultrasonic studies of the magnetic phase transition in MnSi, J. Phys.: Condens. Matter **21**, 196001 (2009).

[97] A. Bauer and C. Pfleiderer, Magnetic phase diagram of MnSi inferred from magnetization and AC susceptibility, Phys. Rev. B **85**, 214418 (2012).

[98] T. Sakakibara, H. Mollymoto, and M. Date, Magnetization and magnetoresistance of MnSi. II, J. Phys. Soc. Jpn. **51**, 2439 (1982).

[99] C. Pappas, E. Lelièvre-Berna, P. Bentley, P. Falus, P. Fouquet, and B. Farago, Magnetic fluctuations and correlations in MnSi: Evidence for a chiral skyrmion spin liquid phase, Phys. Rev. B **83**, 224405 (2011).

[100] C. Pappas, E. Lelièvre-Berna, P. Falus, P. M. Bentley, E. Moskvin, S. Grigoriev, P. Fouquet, and B. Farago, Chiral paramagnetic skyrmion-like phase in MnSi, Phys. Rev. Lett. **102**, 197202 (2009).

Bibliography

[101] U. K. Rößler, A. N. Bogdanov, and C. Pfleiderer, Spontaneous skyrmion ground states in magnetic metals, Nature **442**, 797 (2006).

[102] A. Hamann, D. Lamago, T. Wolf, H. v. Löhneysen, and D. Reznik, Magnetic blue phase in the chiral itinerant magnet MnSi, Phys. Rev. Lett. **107**, 037207 (2011).

[103] M. Janoschek, M. Garst, A. Bauer, P. Krautscheid, R. Georgii, P. Böni, and C. Pfleiderer, Fluctuation-induced first-order phase transition in Dzyaloshinskii-Moriya helimagnets, Phys. Rev. B **87**, 134407 (2013).

[104] S. A. Brazovskii, Phase transition of an isotropic system to a nonuniform state, Sov. Phys. JETP **41**, 85 (1975).

[105] A. Bauer, A. Chacon, M. Wagner, M. Halder, R. Georgii, A. Rosch, C. Pfleiderer, and M. Garst, Symmetry breaking, slow relaxation dynamics, and topological defects at the field-induced helix reorientation in MnSi, Phys. Rev. B **95**, 024429 (2017).

[106] N. Doiron-Leyraud, I. R. Walker, L. Taillefer, M. J. Steiner, S. R. Julian, and G. G. Lonzarich, Fermi-liquid breakdown in the paramagnetic phase of a pure metal, Nature **425**, 595 (2003).

[107] P. Pedrazzini, D. Jaccard, G. Lapertot, J. Flouquet, Y. Inada, H. Kohara, and Y. Onuki, Probing the extended non-Fermi liquid regimes of MnSi and Fe, Phys. B **378-380**, 165 (2006).

[108] T. R. Kirkpatrick and D. Belitz, Columnar fluctuations as a source of non-Fermi-liquid behavior in weak metallic magnets, Phys. Rev. Lett. **104**, 256404 (2010).

[109] C. Thessieu, J. Flouquet, G. Lapertot, A. N. Stepanov, and D. Jaccard, Magnetism and spin fluctuations in a weak itinerant ferromagnet: MnSi, Solid State Commun. **95**, 707 (1995).

[110] K. Koyama, T. Goto, T. Kanomata, and R. Note, Observation of an itinerant metamagnetic transition in MnSi under high pressure, Phys. Rev. B **62**, 986 (2000).

[111] C. Pfleiderer, D. Reznik, L. Pintschovius, and J. Haug, Magnetic field and pressure dependence of small angle neutron scattering in MnSi, Phys. Rev. Lett. **99**, 156406 (2007).

[112] C. Pfleiderer, D. Reznik, L. Pintschovius, H. Löhneysen, M. Garst, and A. Rosch, Partial order in the non-fermi-liquid phase of MnSi, Nature **427**, 227 (2004).

[113] Y. J. Uemura, T. Goko, I. M. Gat-Malureanu, J. P. Carlo, P. L. Russo, A. T. Savici, A. Aczel, G. J. MacDougall, J. A. Rodriguez, G. M. Luke, S. R. Dunsiger, A. McCollam, J. Arai, C. Pfleiderer, P. Böni, K. Yoshimura, E. Baggio-Saitovitch, M. B. Fontes, J. Larrea,

Y. V. Sushko, and J. Sereni, Phase separation and suppression of critical dynamics at quantum phase transitions of MnSi and $Sr_{1-x}Ca_xRuO_3$, Nat. Phys. **3**, 29 (2007).

[114] S. S. Saxena, P. Agarwal, K. Ahilan, F. M. Grosche, R. K. W. Haselwimmer, M. J. Steiner, E. Pugh, I. R. Walker, S. R. Julian, P. Monthoux, G. G. Lonzarich, A. Huxley, I. Sheikin, D. Braithweite, and J. Flouquet, Superconductivity on the border of itinerant electron ferromagnetism in UGe_2, J. Magn. Magn. Mater. **226-230**, 45 (2001).

[115] S. Friedemann, W. J. Duncan, M. Hirschberger, T. W. Bauer, R. Küchler, A. Neubauer, M. Brando, C. Pfleiderer, and F. M. Grosche, Quantum tricritical points in $NbFe_2$, Nat. Phys. **14**, 62 (2017).

[116] R. Ritz, M. Halder, C. Franz, A. Bauer, M. Wagner, R. Bamler, A. Rosch, and C. Pfleiderer, Giant generic topological Hall resistivity of MnSi under pressure, Phys. Rev. B **87**, 134424 (2013).

[117] T. Skyrme and T. Skyrme, A non-linear field theory, Proc. R. Soc. Lond. A **260**, 127 (1961).

[118] T. H. R. Skyrme, A unified field theory of mesons and baryons, Nucl. Phys. **31**, 556 (1962).

[119] S. L. Sondhi, A. Karlhede, S. A. Kivelson, and E. H. Rezayi, Skyrmions and the crossover from the integer to fractional quantum Hall effect at small Zeeman energies, Phys. Rev. B **47**, 16419 (1993).

[120] L. Brey, H. A. Fertig, R. Côté, and A. H. MacDonald, Skyrme crystal in a two-dimensional electron gas, Phys. Rev. Lett. **75**, 2562 (1995).

[121] A. Schmeller, J. P. Eisenstein, L. N. Pfeiffer, and K. W. West, Evidence for skyrmions and single spin flips in the integer quantized Hall effect, Phys. Rev. Lett. **75**, 4290 (1995).

[122] E. H. Aifer, B. B. Goldberg, and D. A. Broido, Evidence of skyrmion excitations about $\nu = 1$ in n-modulation-doped single quantum wells by interband optical transmission, Phys. Rev. Lett. **76**, 680 (1996).

[123] J. Alicea and M. P. A. Fisher, Graphene integer quantum Hall effect in the ferromagnetic and paramagnetic regimes, Phys. Rev. B **74**, 075422 (2006).

[124] Y. Lian, A. Rosch, and M. O. Goerbig, Su(4) skyrmions in the $\nu = \pm 1$ quantum Hall state of graphene, Phys. Rev. Lett. **117**, 056806 (2016).

[125] U. A. Khawaja and H. Stoof, Skyrmions in a ferromagnetic Bose–Einstein condensate, Nature **411**, 918 (2001).

Bibliography

[126] L. S. Leslie, A. Hansen, K. C. Wright, B. M. Deutsch, and N. P. Bigelow, Creation and detection of skyrmions in a Bose–Einstein condensate, Phys. Rev. Lett. **103**, 250401 (2009).

[127] J.-y. Choi, W. J. Kwon, and Y.-i. Shin, Observation of Topologically Stable 2D Skyrmions in an Antiferromagnetic Spinor Bose-Einstein Condensate, Phys. Rev. Lett. **108**, 035301 (2012).

[128] J.-i. Fukuda and S. Žumer, Quasi-two-dimensional Skyrmion lattices in a chiral nematic liquid crystal, Nat. Commun. **2**, 246 (2011).

[129] A. Nych, J.-i. Fukuda, U. Ognysta, S. Žumer, and I. Muševič, Spontaneous formation and dynamics of half-skyrmions in a chiral liquid-crystal film, Nat. Phys. **13**, 1215 (2017).

[130] S. Mühlbauer, C. Pfleiderer, P. Böni, M. Laver, E. M. Forgan, D. Fort, U. Keiderling, and G. Behr, Morphology of the superconducting vortex lattice in ultrapure niobium, Phys. Rev. Lett. **102**, 136408 (2009).

[131] P. Milde, D. Köhler, J. Seidel, L. M. Eng, A. Bauer, A. Chacon, J. Kindervater, S. Mühlbauer, C. Pfleiderer, S. Buhrandt, C. Schütte, and A. Rosch, Unwinding of a skyrmion lattice by magnetic monopoles, Science **340**, 1076 (2013).

[132] Y. Ishikawa and M. Arai, Magnetic phase diagram of MnSi near critical temperature studied by neutron small angle scattering, J. Phys. Soc. Jpn. **53**, 2726 (1984).

[133] B. Lebech, Magnetic ordering in nearly ferromagnetic antiferromagnetic helices, in *Recent Advances in Magnetism of Transition Metal Compounds*, edited by A. Kotani and N. Suzuki (World Scientific, 1993) p. 167.

[134] S. V. Grigoriev, S. V. Maleyev, A. I. Okorokov, Y. O. Chetverikov, P. Böni, R. Georgii, D. Lamago, H. Eckerlebe, and K. Pranzas, Magnetic structure of MnSi under an applied field probed by polarized small-angle neutron scattering, Phys. Rev. B **74**, 214414 (2006).

[135] S. V. Grigoriev, S. V. Maleyev, A. I. Okorokov, Y. O. Chetverikov, and H. Eckerlebe, Field-induced reorientation of the spin helix in MnSi near T_c, Phys. Rev. B **73**, 224440 (2006).

[136] T. Adams, A. Chacon, M. Wagner, A. Bauer, G. Brandl, B. Pedersen, H. Berger, P. Lemmens, and C. Pfleiderer, Long-wavelength helimagnetic order and skyrmion lattice phase in Cu_2OSeO_3, Phys. Rev. Lett. **108**, 237204 (2012).

[137] C. Pfleiderer, T. Adams, A. Bauer, W. Biberacher, B. Binz, F. Birkelbach, P. Böni, C. Franz, R. Georgii, M. Janoschek, F Jonietz, T. Keller, R. Ritz, S. Mühlbauer, W. Münzer, A. Neubauer, B. Pedersen, and A. Rosch, Skyrmion lattices in metallic and semiconducting B20 transition metal compounds, J. Phys.: Condens. Matter **22**, 164207 (2010).

[138] W. Münzer, A. Neubauer, T. Adams, S. Mühlbauer, C. Franz, F. Jonietz, R. Georgii, P. Böni, B. Pedersen, M. Schmidt, A. Rosch, and C. Pfleiderer, Skyrmion lattice in the doped semiconductor $Fe_{1-x}Co_xSi$, Phys. Rev. B **81**, 041203 (2010).

[139] S. Seki, J.-H. Kim, D. S. Inosov, R. Georgii, B. Keimer, S. Ishiwata, and Y. Tokura, Formation and rotation of skyrmion crystal in the chiral-lattice insulator Cu_2OSeO_3, Phys. Rev. B **85**, 220406 (2012).

[140] E. Moskvin, S. Grigoriev, V. Dyadkin, H. Eckerlebe, M. Baenitz, M. Schmidt, and H. Wilhelm, Complex Chiral Modulations in FeGe Close to Magnetic Ordering, Phys. Rev. Lett. **110**, 077207 (2013).

[141] X. Z. Yu, Y. Onose, N. Kanazawa, J. H. Park, J. H. Han, Y. Matsui, N. Nagaosa, and Y. Tokura, Real-space observation of a two-dimensional skyrmion crystal, Nature **465**, 901 (2010).

[142] S. Seki, X. Z. Yu, S. Ishiwata, and Y. Tokura, Observation of skyrmions in a multiferroic material, Science **336**, 198 (2012).

[143] H. S. Park, X. Yu, S. Aizawa, T. Tanigaki, T. Akashi, Y. Takahashi, T. Matsuda, N. Kanazawa, Y. Onose, D. Shindo, A. Tonomura, and Y. Tokura, Observation of the magnetic flux and three-dimensional structure of skyrmion lattices by electron holography, Nat. Nanotechnol. **9**, 337 (2014).

[144] A. Bogdanov and D. Yablonskii, Thermodynamically stable "vortices" in magnetically ordered crystals. The mixed state of magnets, Sov. Phys. JETP **68**, 101 (1989).

[145] A. Bogdanov and A. Hubert, Thermodynamically stable magnetic vortex states in magnetic crystals, J. Magn. Magn. Mater. **138**, 255 (1994).

[146] S. Heinze, K. von Bergmann, M. Menzel, J. Brede, A. Kubetzka, R. Wiesendanger, G. Bihlmayer, and S. Blügel, Spontaneous atomic-scale magnetic skyrmion lattice in two dimensions, Nat. Phys. **7**, 713 (2011).

[147] O. Boulle, J. Vogel, H. Yang, S. Pizzini, D. de Souza Chaves, A. Locatelli, T. O. Menteş, A. Sala, L. D. Buda-Prejbeanu, O. Klein, M. Belmeguenai, Y. Roussigné, A. Stashkevich, S. M. Chérif, L. Aballe, M. Foerster, M. Chshiev, S. Auffret, I. M. Miron, and G. Gaudin, Room-temperature chiral magnetic skyrmions in ultrathin magnetic nanostructures, Nat. Nano. **11**, 449 (2016).

[148] N. Romming, C. Hanneken, M. Menzel, J. E. Bickel, B. Wolter, K. Bergmann, A. Kubetzka, and R. Wiesendanger, Writing and deleting single magnetic skyrmions, Science **341**, 636 (2013).

[149] S. L. Zhang, I. Stasinopoulos, T. Lancaster, F. Xiao, A. Bauer, F. Rucker, A. A. Baker, A. I. Figueroa, Z. Salman, F. L. Pratt, S. J. Blundell, T. Prokscha, A. Suter, J. Waizner, M. Garst, D. Grundler, G. van der Laan, C. Pfleiderer, and T. Hesjedal, Room-temperature helimagnetism in FeGe thin films, Sci. Rep. **7**, 123 (2017).

[150] C. Moreau-Luchaire, C. Moutafis, N. Reyren, J. Sampaio, C. a. F. Vaz, N. Van Horne, K. Bouzehouane, K. Garcia, C. Deranlot, P. Warnicke, P. Wohlhüter, J.-M. George, M. Weigand, J. Raabe, V. Cros, and A. Fert, Additive interfacial chiral interaction in multilayers for stabilization of small individual skyrmions at room temperature, Nat. Nanotechnol. **11**, 444 (2016).

[151] T. Adams, S. Mühlbauer, C. Pfleiderer, F. Jonietz, A. Bauer, A. Neubauer, R. Georgii, P. Böni, U. Keiderling, K. Everschor, M. Garst, and A. Rosch, Long-range crystalline nature of the skyrmion lattice in MnSi, Phys. Rev. Lett. **107**, 217206 (2011).

[152] S. Seki and M. Mochizuki, *Skyrmions in Magnetic Materials*, 1st ed. (Springer, 2015).

[153] S. X. Huang and C. L. Chien, Extended skyrmion phase in epitaxial FeGe(111) thin films, Phys. Rev. Lett. **108**, 267201 (2012).

[154] C. Franz, *Experimentelle Untersuchung von Ferromagnetischen Quantenphasenübergängen*, Diploma Thesis, TU München (2008).

[155] C. Franz, F. Freimuth, A. Bauer, R. Ritz, C. Schnarr, C. Duvinage, T. Adams, S. Blügel, A. Rosch, Y. Mokrousov, and C. Pfleiderer, Real-space and reciprocal-space Berry phases in the Hall effect of $Mn_{1-x}Fe_xSi$, Phys. Rev. Lett. **112**, 186601 (2014).

[156] N. Kanazawa, Y. Onose, T. Arima, D. Okuyama, K. Ohoyama, S. Wakimoto, K. Kakurai, S. Ishiwata, and Y. Tokura, Large topological hall effect in a short-period helimagnet MnGe, Phys. Rev. Lett. **106**, 156603 (2011).

[157] H. Yanagihara and M. B. Salamon, Skyrmion strings and the anomalous Hall-effect in CrO_2, Phys. Rev. Lett. **89**, 187201 (2002).

[158] Y. Taguchi, Y. Oohara, H. Yoshizawa, N. Nagaosa, and Y. Tokura, Spin chirality, Berry phase, and anomalous Hall effect in a frustrated ferromagnet, Science **291**, 2573 (2001).

[159] Y. Machida, S. Nakatsuji, Y. Maeno, T. Tayama, T. Sakakibara, and S. Onoda, Unconventional anomalous Hall effect enhanced by a noncoplanar spin texture in the frustrated kondo lattice $Pr_2Ir_2O_7$, Phys. Rev. Lett. **98**, 057203 (2007).

[160] S. Yoshii, S. Iikubo, T. Kageyama, K. Oda, Y. Kondo, K. Murata, and M. Sato, Anomalous hall effect of pyrochlore molybdate $Nd_2Mo_2O_7$, J. Phys. Soc. Jpn. **69**, 3777 (2000).

[161] S. Nakatsuji, N. Kiyohara, and T. Higo, Large anomalous Hall effect in a non-collinear antiferromagnet at room temperature, Nature **527**, nature15723 (2015).

[162] Z. H. Liu, Y. J. Zhang, G. D. Liu, B. Ding, E. K. Liu, H. M. Jafri, Z. P. Hou, W. H. Wang, X. Q. Ma, and G. H. Wu, Transition from anomalous Hall effect to topological Hall effect in hexagonal non-collinear magnet Mn_3Ga, Sci. Rep. **7**, 515 (2017).

[163] C. Sürgers, T. Wolf, P. Adelmann, W. Kittler, G. Fischer, and H. v Löhneysen, Switching of a large anomalous Hall effect between metamagnetic phases of a non-collinear antiferromagnet, Sci. Rep. **7**, 42982 (2017).

[164] L. Berger, Prediction of a domain-drag effect in uniaxial, non-compensated, ferromagnetic metals, J. Phys. Chem. Solids **35**, 947 (1974).

[165] L. Berger, Low-field magnetoresistance and domain drag in ferromagnets, J. Appl. Phys. **49**, 2156 (1978).

[166] L. Berger, Motion of a magnetic domain wall traversed by fast-rising current pulses, J. Appl. Phys. **71**, 2721 (1992).

[167] J. C. Slonczewski, Current-driven excitation of magnetic multilayers, J. Magn. Mang. Mat. **159**, L1 (1996).

[168] S. Parkin and S.-H. Yang, Memory on the racetrack, Nat. Nanotechnol. **10**, 195 (2015).

[169] L. Thomas, S.-H. Yang, K.-S. Ryu, B. Hughes, C. Rettner, D.-S. Wang, C.-H. Tsai, K.-H. Shen, and S. S. P. Parkin, Racetrack Memory: A high-performance, low-cost, non-volatile memory based on magnetic domain walls, in *2011 International Electron Devices Meeting* (2011) p. 24.2.1.

[170] K. Everschor, M. Garst, R. A. Duine, and A. Rosch, Current-induced rotational torques in the skyrmion lattice phase of chiral magnets, Phys. Rev. B **84**, 064401 (2011).

[171] M. Mochizuki, Chapter 3: Current-Driven dynamics of Skyrmions, in *Topological Structures in Ferroic Materials*, edited by J. Seidel (Springer, 2016) 1st ed.

[172] L. Berger, Emission of spin waves by a magnetic multilayer traversed by a current, Phys. Rev. B **54**, 9353 (1996).

[173] S. Zhang and Z. Li, Roles of nonequilibrium conduction electrons on the magnetization dynamics of ferromagnets, Phys. Rev. Lett. **93**, 127204 (2004).

[174] A. A. Thiele, Steady-state motion of magnetic domains, Phys. Rev. Lett. **30**, 230 (1973).

Bibliography

[175] K. Everschor, M. Garst, B. Binz, F. Jonietz, S. Mühlbauer, C. Pfleiderer, and A. Rosch, Rotating skyrmion lattices by spin torques and field or temperature gradients, Phys Rev B **86**, 054432 (2012).

[176] K. Everschor, *Current-Induced Dynamics of Chiral Magnetic Structures: Skyrmions, Emergent Electrodynamics and Spin-Transfer Torques*, PhD thesis, Institute for Theoretical Physics, University of Cologne (2012).

[177] G. Blatter, M. V. Feigel'man, V. B. Geshkenbein, A. I. Larkin, and V. M. Vinokur, Vortices in high-temperature superconductors, Rev. Mod. Phys. **66**, 1125 (1994).

[178] N. B. Kopnin, Vortex dynamics and mutual friction in superconductors and Fermi superfluids, Rep. Prog. Phys. **65**, 1633 (2002).

[179] A. Schmid and W. Hauger, On the theory of vortex motion in an inhomogeneous superconducting film, J. Low Temp. Phys. **11**, 667 (1973).

[180] C. Schnarr, *Spin-Transfer-Torque-Effekte in $Mn_{1-x}Fe_x$ Si-Volumenkristallen Und Epitaktischen MnSi-Schichten*, PhD thesis, TU München (2017).

[181] S. L. Zhang, W. W. Wang, D. M. Burn, H. Peng, H. Berger, A. Bauer, C. Pfleiderer, G. van der Laan, and T. Hesjedal, Manipulation of skyrmion motion by magnetic field gradients, Nat. Commun. **9**, 2115 (2018).

[182] S. Pöllath, J. Wild, L. Heinen, T. N. G. Meier, M. Kronseder, L. Tutsch, A. Bauer, H. Berger, C. Pfleiderer, J. Zweck, A. Rosch, and C. H. Back, Dynamical defects in rotating magnetic skyrmion lattices, Phys. Rev. Lett. **118**, 207205 (2017).

[183] M. Mochizuki, X. Z. Yu, S. Seki, N. Kanazawa, W. Koshibae, J. Zang, M. Mostovoy, Y. Tokura, and N. Nagaosa, Thermally driven ratchet motion of a skyrmion microcrystal and topological magnon Hall effect, Nat. Mater. **13**, 241 (2014).

[184] J. Sampaio, V. Cros, S. Rohart, A. Thiaville, and A. Fert, Nucleation, stability and current-induced motion of isolated magnetic skyrmions in nanostructures, Nat. Nano. **8**, 839 (2013).

[185] X. Zhang, M. Ezawa, and Y. Zhou, Magnetic skyrmion logic gates: Conversion, duplication and merging of skyrmions, Sci. Rep. **5**, 9400 (2015).

[186] S. Zhang, A. A. Baker, S. Komineas, and T. Hesjedal, Topological computation based on direct magnetic logic communication, Sci. Rep. **5**, 15773 (2015).

[187] H. Y. Yuan and X. R. Wang, Skyrmion creation and manipulation by nano-second current pulses, Sci. Rep. **6**, 22638 (2016).

[188] W. Jiang, P. Upadhyaya, W. Zhang, G. Yu, M. B. Jungfleisch, F. Y. Fradin, J. E. Pearson, Y. Tserkovnyak, K. L. Wang, O. Heinonen, S. G. E. te Velthuis, and A. Hoffmann, Blowing magnetic skyrmion bubbles, Science **349**, 283 (2015).

[189] J. Iwasaki, M. Mochizuki, and N. Nagaosa, Universal current-velocity relation of skyrmion motion in chiral magnets, Nat. Commun. **4**, 1463 (2013).

[190] J. Iwasaki, M. Mochizuki, and N. Nagaosa, Current-induced skyrmion dynamics in constricted geometries, Nat. Nanotech **8**, 742 (2013).

[191] C. Schnarr, A. Bauer, and C. Pfleiderer, Doping dependence of the threshold current for skyrmion drift in $Mn_{1-x}Fe_xSi$, in prep. (2018).

[192] S. Mühlbauer, J. Kindervater, T. Adams, A. Bauer, U. Keiderling, and C. Pfleiderer, Kinetic small angle neutron scattering of the skyrmion lattice in MnSi, New J. Phys. **18**, 075017 (2016).